Modeling the Energetics of the Upper Atmosphere

Karthik Venkataramani

Dissertation submitted to the Faculty of the
Virginia Polytechnic Institute and State University
in partial fulfillment of the requirements for the degree of

Doctor of Philosophy
in
Electrical Engineering

Scott M. Bailey, Chair
Joseph B. Baker
Gregory D. Earle
Bhuvana Srinivasan
Yizheng Zhu

May 14, 2018
Blacksburg, Virginia

Keywords: Thermosphere, 5.3 microns, Infrared Emissions, Nitric Oxide, Numerical Modeling

Modeling the Energetics of the Upper Atmosphere

Karthik Venkataramani

(ABSTRACT)

Nitric oxide (NO) is a minor species in the Earth's atmosphere whose densities have been measured to closely reflect solar energy deposition above 100 km. It is an efficient emitter in the infrared where the thermosphere is optically thin, and serves as an important source of radiative cooling between 100 - 200 km. The primary mechanism of this cooling involves the conversion of kinetic energy from the background atmosphere into vibrational energy in NO, followed by the radiative de-excitation of the NO molecule. This results in the production of a 5.3 µm photon which escapes the thermosphere and results in a net cooling of the region. While this process causes the excitation of ground state NO to its first vibrational level, nascent vibrational excitation to the (v$\geq$ 1) levels may also occur from the reactions that produce NO in the thermosphere. The NO(v$\geq$ 1) molecules produced from this secondary process can undergo a radiative cascade and emit multiple photons, thus forming a significant fraction of the 5.3 µm emission from NO in the thermosphere.

Existing thermospheric models consider the collisional excitation of NO to be the only source of the 5.3 µm emission and assume the contribution from nascent excitation to be negligible. These models also tend to use a rate coefficient for the collisional excitation that is significantly larger than the values suggested in literature in order to obtain a temperature profile that is in agreement with empirical data. We address these discrepancies by presenting an updated calculation of the chemically produced emission by accounting for the $v \leq 10$ level populations. By incorporating this process into a three dimensional global upper atmospheric model, it is shown that the additional emission contributes between $5 - 40\%$ of the daytime emission from nitric oxide under quiet solar conditions, and is a significant source of energy loss during periods of enhanced solar energy deposition. Accounting for this process however does not resolve the model-data discrepancy seen with regards to the recovery times of thermospheric densities following geomagnetic storms, suggesting that an improved treatment of nitric oxide chemistry is required to resolve this issue.

In order to improve our understanding of the thermospheric energy budget, we also develop the Atmospheric Chemistry and Energetics (ACE) 1D model using up-to-date aeronomic results. The model self-consistently solves the 1D momentum and energy equations to produce a global average profile of the coupled thermosphere and ionosphere system in terms of its constituent densities and temperatures. The model calculations of neutral densities and exospheric temperatures are found to be in good agreement with empirical data for a wide range of solar activity.

It is concluded from the present work that while the magnitude of the chemically produced emission from nitric oxide has previously been underestimated, its effect on the thermospheric energy budget is relatively small. Including the secondary emission in thermospheric models results in an average reduction of 3% in the exospheric temperatures, which does not

completely offset the change introduced by using a smaller rate coefficient for the collisional excitation of NO. However, thermospheric temperatures can still be accurately modeled by including these changes as part of broader improvements to calculations of the thermospheric energy budget.

Modeling the Energetics of the Upper Atmosphere

Karthik Venkataramani

(GENERAL AUDIENCE ABSTRACT)

Nitric oxide (NO) is a molecule that is produced in the Earth's thermosphere (the region of the atmosphere above 100 kilometers) as a consequence of solar energy deposition. As an important source of radiative cooling, its presence significantly influences the temperature structure of the region. An accurate understanding of the associated energetics is thus vital towards the development of numerical models used to describe the thermosphere.

Energy loss from the thermosphere due to nitric oxide begins with the vibrational excitation of the molecule either due to collisions or chemical processes, followed by the emission of one or more infrared photons which returns the molecule to the ground state. The photons produced escape the thermosphere resulting in a net energy loss from this region of the atmosphere.

Existing thermospheric models generally account for the vibrational excitation of nitric oxide only via collisions, and have assumed chemical processes to be a negligible source of thermospheric energy loss. These models also assume a rate of collisional excitation that is significantly larger than the values suggested in literature in order to obtain a temperature profile that is in agreement with empirical data. The present work demonstrates that the chemical excitation in fact contributes to between $5 - 40\%$ of the total energy loss due to nitric oxide under quiet solar conditions on the dayside of the Earth, and is also an important energy loss mechanism during periods of enhanced solar activity. However, including this mechanism into existing models does not resolve outstanding model-data discrepancies regarding the rate at which the thermosphere returns to equilibrium following sudden enhancements in solar energy deposition. This suggests the need for an improved treatment of the nitric oxide chemistry in current thermospheric models.

This work also presents the Atmospheric Chemistry and Energetics (ACE) 1D model, a new one dimensional upper atmospheric model developed in order to obtain a better understanding of the thermospheric energy budget. The model includes the effects of the chemically produced emissions from nitric oxide, and also uses a collisional cooling rate that is in line with the value suggested in literature. The model calculations of thermospheric densities and temperatures are shown to be in good agreement with empirical data over a wide range of solar activity.

Acknowledgements

My career as a graduate student and this dissertation would not have been possible if it were not for the unwavering support of my advisor and friend, Dr. Scott Bailey. You've shown me how to teach and learn, how to make mistakes but not let them weigh me down, how to laugh and live well. All of this has come to pass simply because you wouldn't have me leave your office as the disillusioned graduate student that walked in. I am proud to be your student and hope to carry your lessons forward.

I am thankful to my parents Ramaswami and Sundari Venkataramani, for their love, patience, and trust in me. I hold you in my heart and always hope to make you proud.

My life is infinitely better off for all the people, places, and music that have helped me get through my time as a graduate student. This journey wouldn't have been half as much fun without them, and I'm grateful to have them in my life.

For my parents

Contents

List of Figures

List of Tables

Chapter 1

Introduction

1.1 The Thermosphere

The thermosphere is the region of the Earth's atmosphere above 100 kilometers. In this region, turbulent mixing processes which serve to keep the composition of the lower atmosphere uniform decrease in importance, as diffusive processes begin to govern the constituent densities. As a result, the composition of the thermosphere varies with height and the densities of the constituent major species exhibit individual gradients that are proportional to their atomic or molecular masses. This is illustrated in Figure 1.1(a), where the global average[1] densities of the major species have been plotted as a function of altitude for equinox conditions and moderate levels of solar activity. The densities show the transition of the thermosphere from being composed primarily of molecular nitrogen and oxygen below 200 km to predominantly atomic oxygen at higher altitudes.

The energy content of the thermosphere can be characterized by the temperature of the neutral gas, which is plotted in Figure 1.1(b) as a function of altitude for different levels of solar activity. A steep gradient exists in the temperatures between 100 - 250 km, above which the thermosphere becomes isothermal. The magnitude of the gradient is seen to increase with solar activity, and is primarily driven by the absorption of solar soft x-rays (XUV) and extreme ultraviolet (EUV) radiation in the thermosphere below 200 km. This is shown in Figure 1.1(c), which plots the average solar energy deposition rate as a function of altitude and wavelength. As the energy deposition rate is dependent on the absorption cross sections and column densities of the major species, it is seen to peak in the lower thermosphere for wavelengths between $0.05 - 105$ nm.

Another significant consequence of solar energy deposition in the thermosphere is the pro-

[1]The density and temperature profiles shown in Figure 1.1 are obtained by averaging data from the MSIS empirical model over the entire globe. While the profiles do not correspond to values at a particular physical location or local time, they are representative of the behaviour of these quantities in the thermosphere.

Table 1.1: Ionization Potentials of Thermospheric species

Species	Ionization Potential (eV [nm])
N_2	15.61 [79.6]
N	14.58 [85.2]
O	13.64 [91.04]
O_2	12.08 [102.78]
CO_2	13.82 [89.9]
NO	9.27 [134.0]
He	24.58 [50.43]
H	13.64 [91.1]

duction of neutral and charged minor species, produced as a result of the dissociation and ionization of the major species. Figure 1.1(d) shows densities of these minor species produced for moderate levels of solar activity from the background atmosphere shown in Figure 1.1(a) and (b). Although the densities of these minor species are several orders of magnitude smaller than that of the background atmosphere, they are coupled to the background atmosphere via chemical and energetic processes, and their presence has a significant effect on the composition and temperature structure of the thermosphere.

1.2 Nitric oxide in the Thermosphere

One such minor species that has a significant role in the upper atmosphere is nitric oxide (NO). Nitric oxide was originally hypothesized as a minor constituent of the upper atmosphere in order to explain the presence of the D-region of the ionosphere, as well as the diurnal variations seen in the extent of ionization of the region (Nicolet, 1955; Nicolet and Aikin, 1960). Knowledge of the solar spectrum at wavelengths below 200 nm (Figure 1.2) and the ionization potentials of various atmospheric constituents (Table 1.1) led to the theory that the strong Lyman-alpha emission from the Sun at 121.57 nm could potentially ionize nitric oxide present in the upper atmosphere, contributing to the formation of the dayside ionosphere. Further, its absence at night would allow for ion recombination and hence electron density depletion to occur.

Confirmation of the presence of a nitric oxide layer in the upper atmosphere came in the form of sounding rocket measurements (Barth, 1964, 1966), which then paved the way for satellite missions that have provided a view of the global distribution of nitric oxide in the thermosphere (Barth et al., 1973; Barth, 1992; Barth et al., 2003). These measurements have

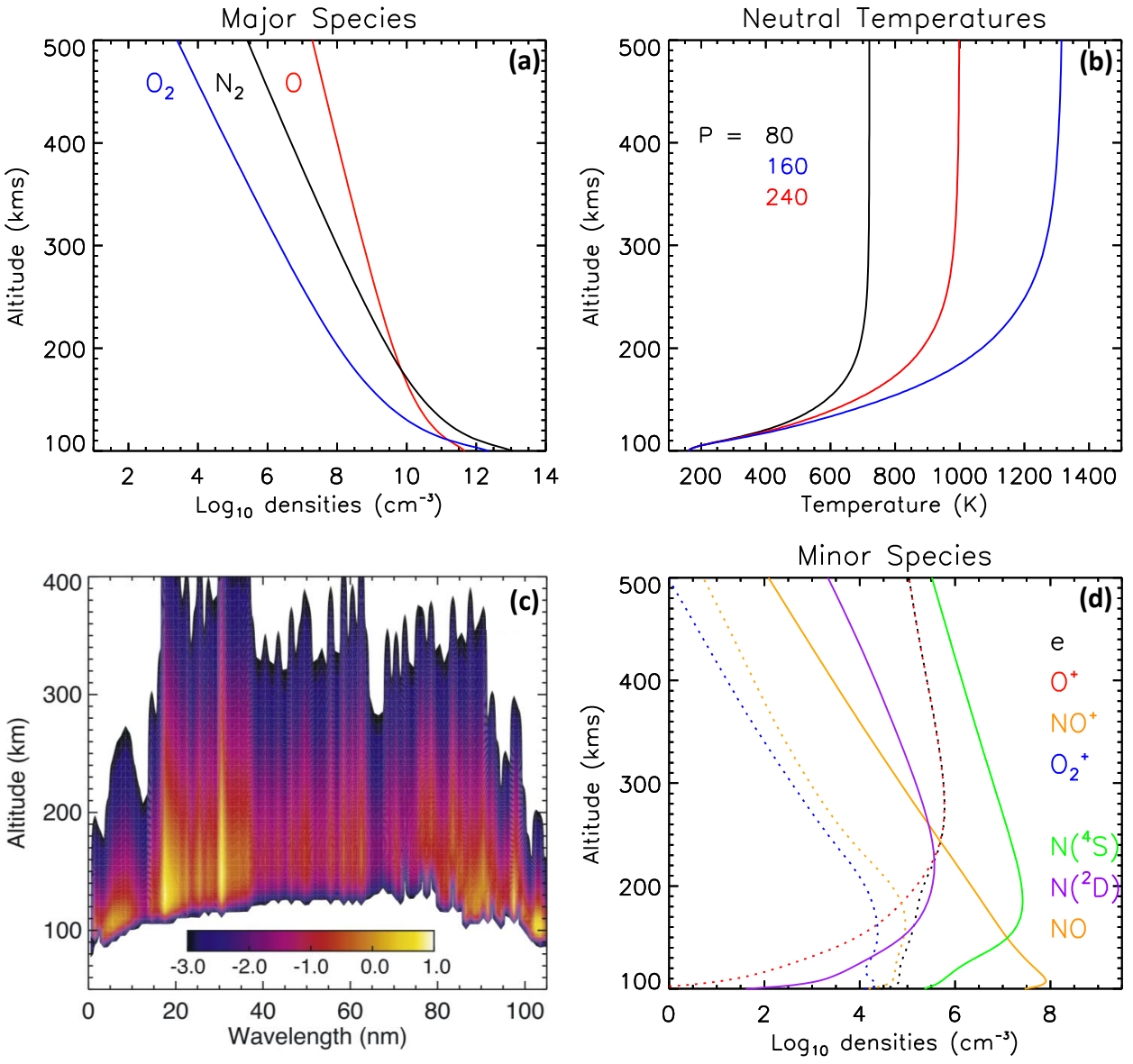

Figure 1.1: Overview of the thermosphere. (a) Global average densities of the major neutral species N_2 (black), O_2 (blue) and O (red). (b) Global average neutral temperatures in the thermosphere for three different levels of solar activity denoted by the proxy P. The values of 80, 160, and 240 indicate low, moderate and high levels of solar activity respectively. (c) Solar EUV energy deposition in units of log(W m^{-3} nm^{-1}) at low solar activity, adopted from Solomon and Qian (2005). (d) Global average densities of neutral (solid lines) and charged (dotted lines) minor species formed in the thermosphere as a result of XUV/EUV absorption by the major species.

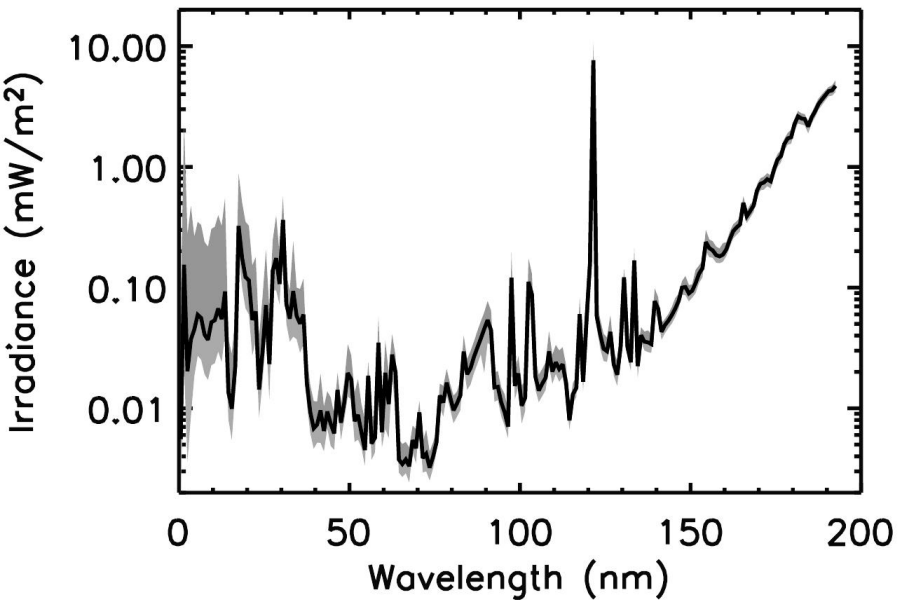

Figure 1.2: Solar spectra measured by the Solar EUV Experiment (SEE) between 2002 and 2004. The black curve shows the average value of the measurement, and the gray overlay indicates the measured solar variability. Reproduced from Woods et al. (2005).

subsequently served to inform models (Barth, 1992; Swaminathan et al., 1998; Bailey et al., 2002; Yonker, 2013) that have been used to explain the processes that govern the production and loss of nitric oxide in the thermosphere.

Figure 1.3 shows measured nitric oxide densities as a function of altitude and latitude on day 80 of 1999 (spring equinox), as observed by the Student Nitric Oxide Explorer (SNOE) satellite Barth et al. (2003). The measurements were made by observing the fluorescent scattering of sunlight by nitric oxide at 215 and 237 nm, and correspond to an average local time of 1030 hours. The density distributions show a characteristic peak between $106-110$ km at all latitudes, produced as a result of energy deposition by soft x-rays. At auroral latitudes, precipitating electrons also contribute to energy deposition in the thermosphere, resulting in larger peak densities. Although Figure 1.3 shows an asymmetry in the density profiles between the two hemispheres for a particular day of observations, long term averages for periods near equinox show density distributions in the two hemisphere to be approximately equal (Barth et al., 2003).

Measurements of the densities at 106 km are shown as a function of day of year and latitude in Figure 1.4. The densities show prominent variations that are driven by changes in the local NO production rate, and underlying changes in the O_2 density and neutral temperatures caused by seasonal effects and the 27 day solar rotation period. These figures indicate that nitric oxide densities in the thermosphere are dependent on the local energy deposition rate,

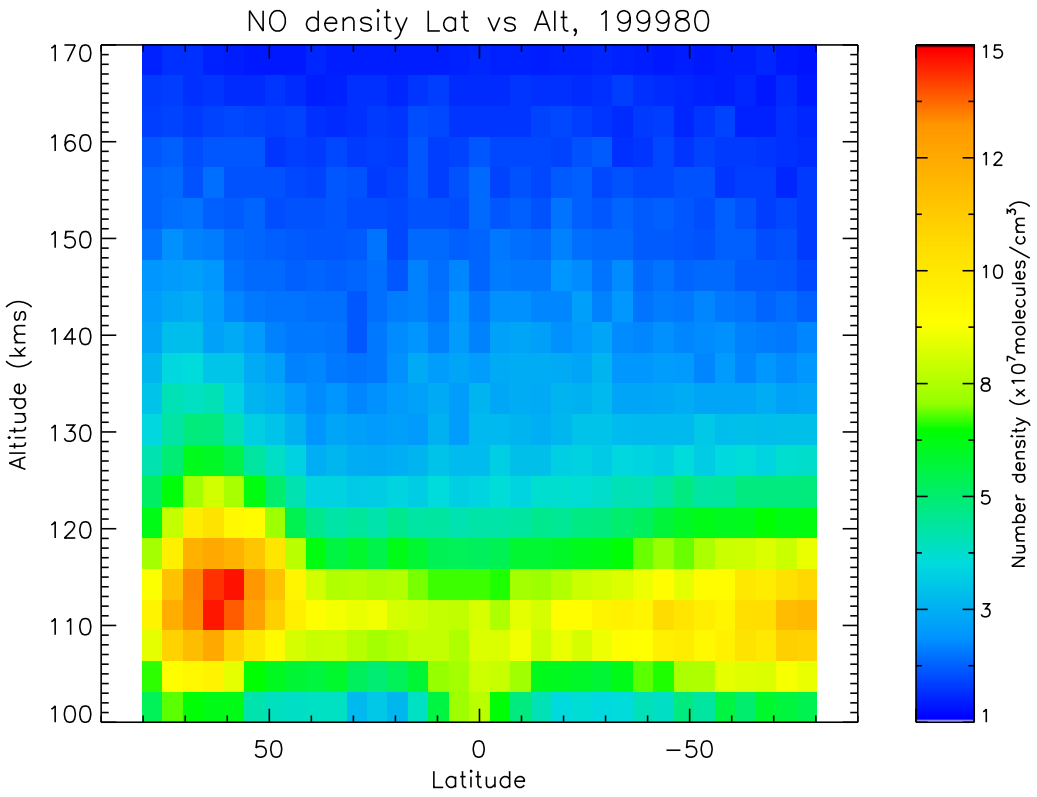

Figure 1.3: Distribution of NO densities in the thermosphere as a function of latitude and altitude, as measured by the Student Nitric Oxide Explorer (SNOE) satellite. Densities are shown for day 80 (March 21st) of 1999 at a local time of 1030 hours.

and are tied to a portion of the solar spectrum that is highly variable in nature.

Nitric oxide is also capable of efficiently radiating in the infrared at 5.3 µm. This emission from the thermosphere is known to be an important source of radiative cooling and has been the subject of several observational (Ballard et al., 1993; Russell et al., 1999; Fischer et al., 2008) and modeling (Sharma et al., 1998; Funke and López-Puertas, 2000; Venkataramani et al., 2016) studies. The effect of this emission is demonstrated in Figure 1.5, which shows calculations of thermospheric temperatures for moderate levels of solar activity. The inclusion of nitric oxide cooling is seen to reduce the calculated exospheric temperatures by 300 K.

The Sounding of the Atmosphere using Broadband Emission Radiometry (SABER) experiment (Russell et al., 1999) aboard the Thermosphere Ionosphere Mesosphere Energetics and Dynamics (TIMED) satellite is significant source of data regarding this emission, with observations being made since 2002. Figure 1.6 shows a typical measurement from this experiment for March 20-22 (days 79-81) of 2003. The plots shows measurements from 15 orbits on the

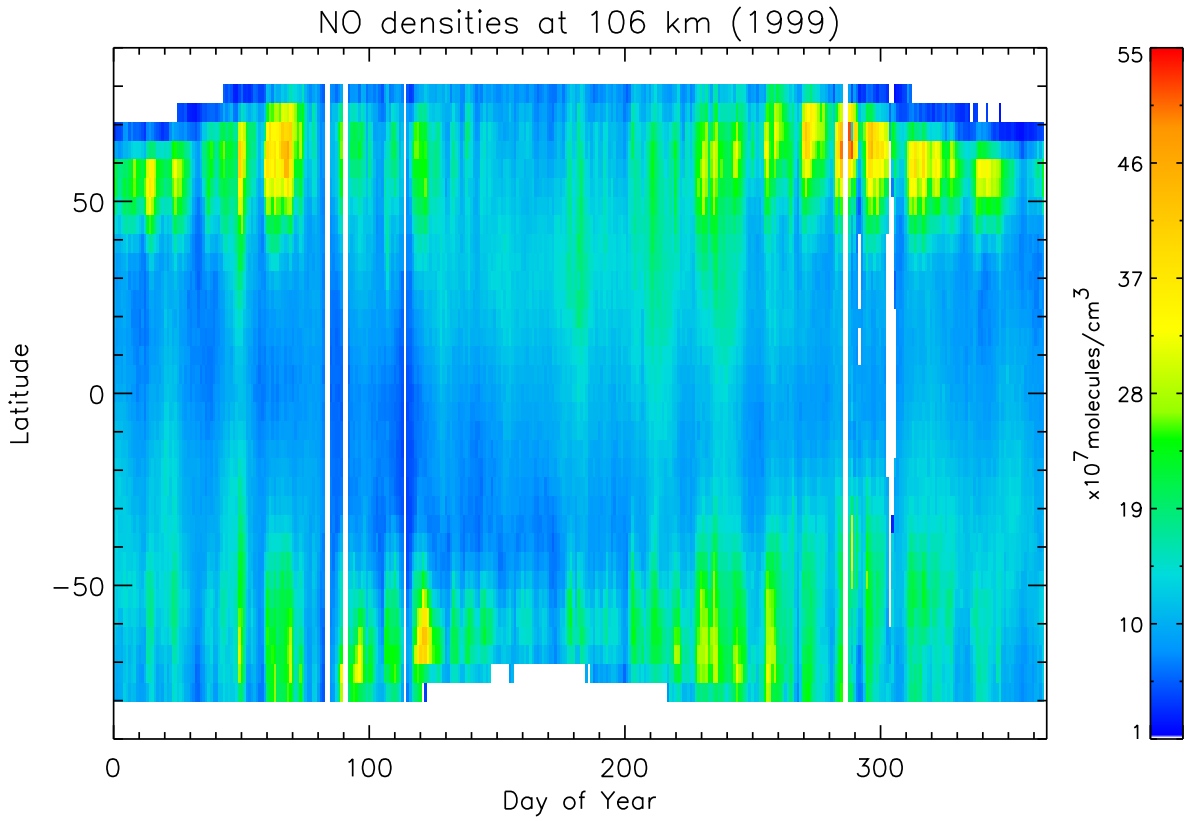

Figure 1.4: Distribution of NO densities in the thermosphere at 106 km as function of latitude and day of year, as measured by the SNOE satellite. Densities are shown for the year 1999.

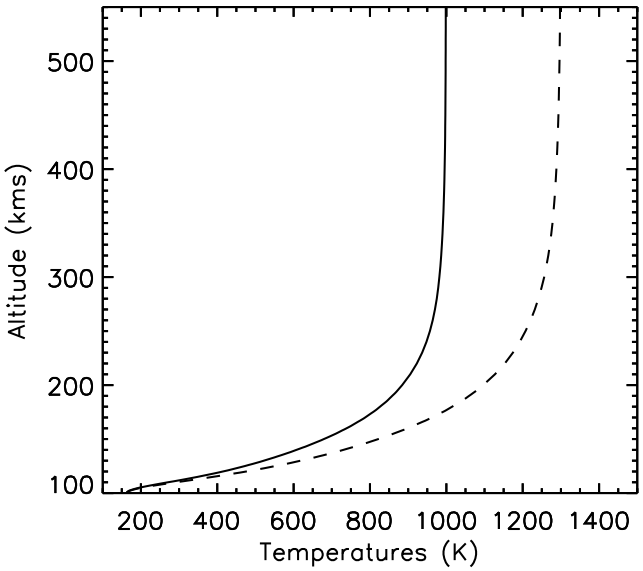

Figure 1.5: Modeled thermospheric temperatures for equinox conditions at moderate levels of solar activity ($P = 160$). The dashed line shows the effect of excluding thermospheric cooling by nitric oxide from calculations.

dayside and nightside for each day, with observations limited to between 55°N and 85°S due to the pointing mode of the instrument. The column emission rates are seen to be similar to the NO density distributions (Figure 1.4), with greater column emission rates observed at auroral latitudes. The apparent diurnal variation seen in the figures is caused by changes in the geomagnetic latitude of measurement between orbits.

Figure 1.7 shows the zonally averaged emission over the same period as a function of altitude and latitude. Once again, the volume emission rates are seen to be greater at higher latitudes, similar to Figure 1.3. However, as the emission depends on both nitric oxide densities and the rate of energy exchange with the background atmosphere, it does not peak near 106 km, and is instead largest near 130 km.

For the period corresponding to the above measurements by SABER, Figure 1.8 shows measurements of the B_z component of the solar wind magnetic field from the Advanced Composition Explorer (ACE) satellite. B_z was observed to be southward ($B_z < 0$) on March 20th (day 79), resulting in increased coupling of the solar wind with the Earth's magnetic field, and a corresponding enhancement in solar wind energy deposition at auroral latitudes (Dungey, 1961). This causes an increase in the thermospheric neutral temperature and nitric oxide density, and is consequently reflected in the 5.3 µm emission on March 20th and 21st. The response of nitric oxide cooling is seen to be nearly concurrent with the energy deposition on the nightside on March 20th, while transport processes result in increased NO

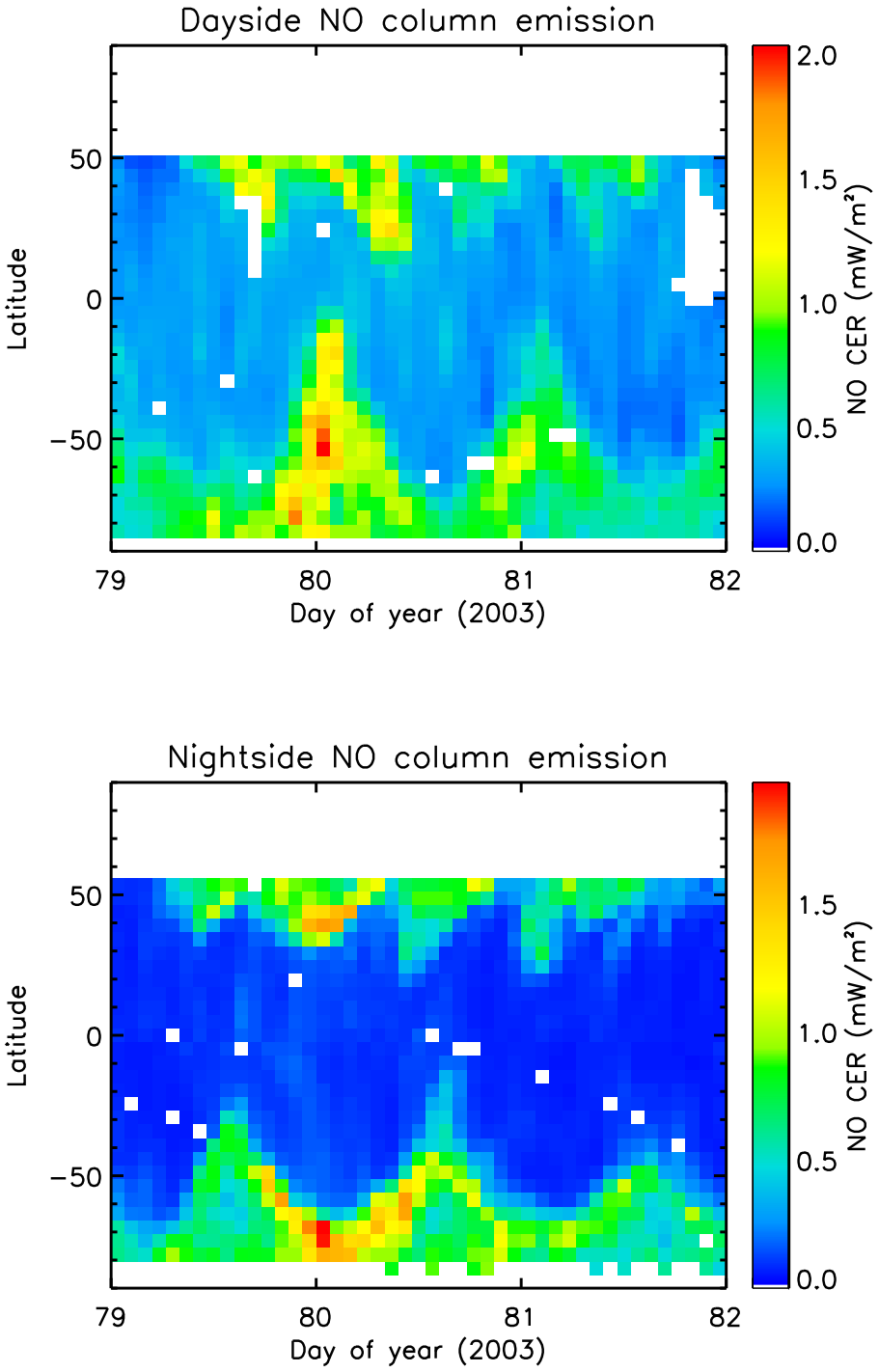

Figure 1.6: Column Emission Rates (CER) obtained by integrating volume emission rates of the 5.3 µm emission between 100-200 km in the thermosphere for day 79-81 of 2003, measured by the SABER instrument. The average local time of measurement on the dayside and nightside are 1100 hours and 0100 hours respectively. The instrument was in its "southward" pointing mode, resulting in no measurements above 55°N.

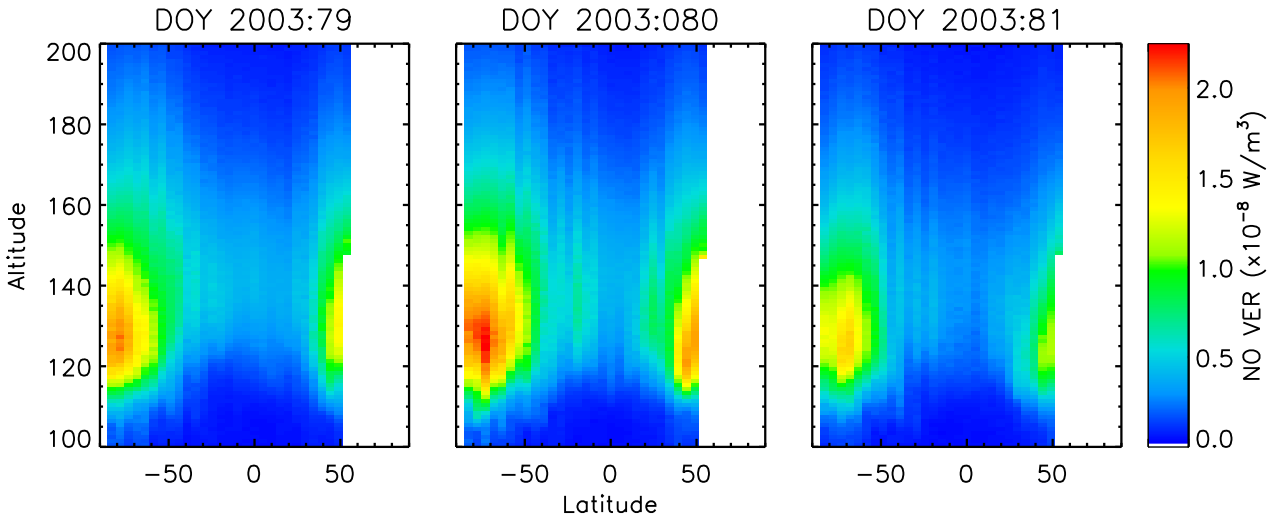

Figure 1.7: Volume emission rates (VER) of the zonally averaged 5.3 µm emission in the thermosphere by the SABER experiment for day 79-81 of 2003.

production and emissions that extend to low latitudes on March 21st (Barth et al., 2009).

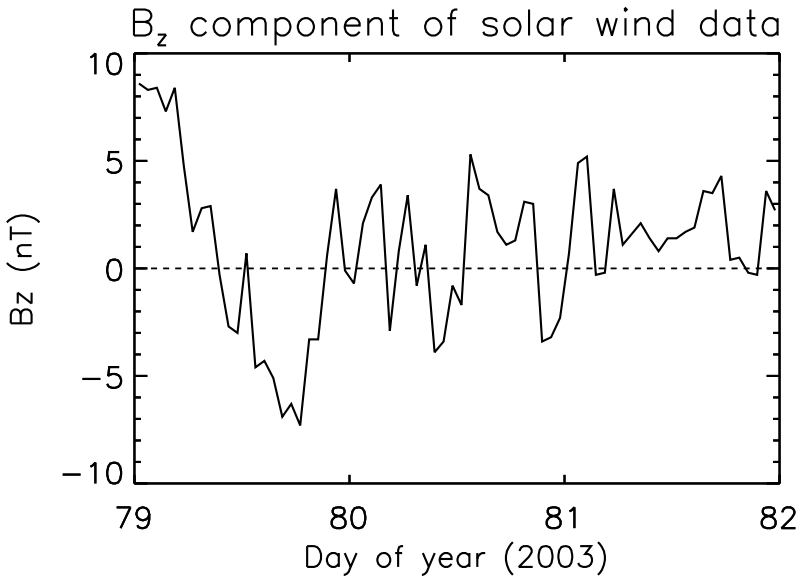

Figure 1.8: B_z component of the solar wind magnetic field / interplanetary magnetic field from the Advanced Composition Explorer (ACE) satellite. Coupling with the Earth's magnetic field occurs when $B_z < 0$, which causes energy deposition in the upper atmosphere.

As B_z returns to values greater than zero on March 22nd (day 81), the energy input from the solar wind reduces and the emission is seen to return to quiescent levels. This indicates that emissions from nitric oxide serve to act as a 'natural thermostat' of the upper atmosphere (Mlynczak et al., 2003), counteracting sudden increases in the thermospheric energy input by radiating away the excess energy.

1.3 Production of Infrared Emissions from Nitric Oxide

To understand the production of infrared emissions from nitric oxide, we first consider the potential energy diagram of a hypothetical diatomic molecule, modeled as an ideal (harmonic) oscillator and non-ideal (anharmonic) oscillator as shown in Figure 1.9. The molecule has one mode of vibration (a symmetric stretch), and specific energy levels associated with this motion denoted by the vibrational quantum number v. It is seen that for the case of an idealized oscillator there are an infinite number of equally spaced vibrational levels; however, in reality the molecule dissociates beyond a certain internuclear distance, and the separation between vibrational levels decreases with increasing v.

In the case of nitric oxide, the bond dissociation energy is approximately 6.5 eV (Minschwaner and Siskind, 1993), and the level separations have been shown to reduce from 0.23 eV for $v = (0 - 1)$ to 0.19 eV for $v = (13 - 14)$ (Rawlins et al., 1992; Billingsley, 1975). As it is heteromolecular in nature (composed of two different atoms) nitric oxide has a permanent dipole moment which can interact with the oscillating electric field of an electromagnetic wave, allowing the molecule to transition between adjacent vibrational levels ($\Delta v = \pm 1$) by the emission or absorption of a photon near 5.3 µm. In the thermosphere, nitric oxide is generally excited to the $v = 1$ vibrational level due to thermal collisions with atomic oxygen, and it subsequently returns to the ground state by the emission of a 5.3 µm photon. This conversion of thermal kinetic energy into infrared radiation by nitric oxide was originally hypothesized as a thermospheric energy loss mechanism by Bates (1951). Kockarts (1980) subsequently provided a theoretical calculation of the energy loss rate due to the emission, and demonstrated it to have a significant effect on the modeled thermospheric temperature.

In addition to the collisional excitation of nitric oxide to the $v = 1$ level, the exothermic reactions that produce nitric oxide in the thermosphere are known to cause nascent excitation of the molecule to the $v \geq 1$ levels (Kennealy et al., 1978; Winkler et al., 1986). In contrast to collisional excitation which results in the production of a single 5.3 µm photon, excitation to the $v > 1$ levels can result in the emission of multiple photons as the molecule radiatively decays to the ground state. For instance, an NO molecule excited to the $v = 3$ level may return to the ground state by undergoing the radiative transitions corresponding to $v = 3 - 2$, $2 - 1$ and $1 - 0$, resulting in the emission of three photons near 5.3 µm of increasing wavelengths. Excitation to these higher ($v > 1$) vibrational levels can also result in radiative

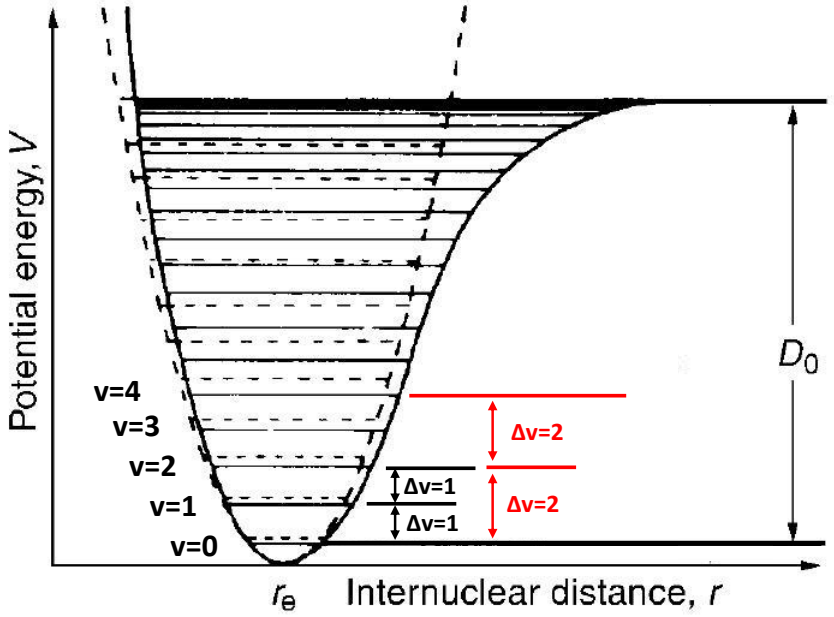

Figure 1.9: Potential energy as a function of internuclear distance for a hyothetical diatomic molecule, modeled as an anharmonic oscillator (solid line) and harmonic oscillator (dashed line). D_0 is the measured dissociation energy of the molecule. Adopted from Hollas (2004).

de-excitation via a $\Delta v = 2$ transition (eg., $v = 3-1$), producing an 'overtone' emission at 2.7 µm. Though the energy loss rate due to this excitation mechanism has been suggested to be relatively small (Sharma et al., 1998; Funke and López-Puertas, 2000), models have generally accounted only for the emission from the $v \leq 2$ levels, and have assumed the contribution of higher levels to be negligible.

1.4 Problem Statement

Current thermospheric models generally assume thermal collisions with the background atmosphere to be the only source of vibrational excitation of nitric oxide, and hence the 5.3 µm emission. While the rate coefficient for the vibrational excitation used in these models Hwang et al. (2003) is significantly larger than the values suggested in literature (Duff and Sharma, 1997; Dodd et al., 1999; Caridade et al., 2008), the higher value is adopted in order to obtain temperature profiles that are in agreement with empirical data. However, recent studies have noted the inability of models to accurately reproduce the observed recovery of thermospheric densities following geomagnetic storms (Lei et al., 2011; Lu et al., 2014; Sheng et al., 2017), suggesting the need to re-examine the current methodology of modeling nitric oxide densities and emissions.

This dissertation explores the role of chemically produced emissions from nitric oxide in order to explain the above discrepancy regarding thermospheric cooling rates. Updated calculations and measurements have shown that the fraction of NO molecules excited to the $v \geq 2$ levels from chemical processes is significantly larger than previously assumed (Winkler et al., 1986; Braunstein and Duff, 2000; Miquel et al., 2003; Sultanov and Balakrishnan, 2006), indicating that the contribution of the chemiluminescent emission may have been previously underestimated. As this emission results in thermospheric energy loss that is concurrent with nitric oxide production, it is shown to be particularly significant during periods of enhanced solar energy deposition.

Further, we hypothesize that existing models are tuned to reproduce observed temperature and neutral mass density profiles at the expense of accurate nitric oxide density calculations. By updating the chemistry scheme employed in models to reflect our current knowledge (Yonker, 2013), we believe the calculations of nitric oxide densities will improve in a manner that allows us to assume a thermal cooling rate coefficient that is consistent with the estimates from lab measurements and theory.

The work presented in this dissertation has two goals - 1) quantify the importance of chemical processes in producing vibrationally excited nitric oxide and hence infrared emissions from the thermosphere, and 2) ascertain if including this additional emission in thermospheric models allows for the use of a nitric oxide cooling rate coefficient that is consistent with the value prevalent in literature.

The remainder of the dissertation is organized as follows - Chapter 2 presents a model of the secondary source of the 5.3 µm emission, obtained by modeling the chemically produced level populations for NO($v \leq 10$). Its contribution to energy loss from the thermosphere is evaluated by incorporating the process into a three dimensional global thermospheric model, which is run for the case of quiet and active solar conditions. We also present a computationally inexpensive parameterization scheme that reproduces results of the full calculation to within 5% under quiet solar conditions.

To obtain a better understanding of the contribution of this additional emission to the thermospheric energy budget, we develop a new, self-consistent one dimensional model of the upper atmosphere that incorporates up-to-date aeronomic results. Chapter 3 presents a detailed description of this new 1D model, while Chapter 4 presents model results obtained for various levels of solar activity. The energetics that govern the neutral temperatures are examined in Chapter 5, along with model sensitivities to changes in the heating and cooling processes. Chapter 6 summarizes the findings of the dissertation.

Chapter 2

Chemiluminescent emissions from Nitric Oxide in the Thermosphere

2.1 Infrared emissions from Nitric Oxide

Infrared emissions from nitric oxide is a significant source of energy loss from the thermosphere, and occurs via a two step process. First, kinetic energy from the major species is converted into vibrational energy in nitric oxide via collisional excitation. The nitric oxide molecule then de-excites either by collisional quenching (where the energy is returned to the background atmosphere), or by radiative de-excitation with the emission of a 5.3 µm photon. The infrared photon produced escapes the thermosphere and results in a net cooling of the atmosphere. The primary reactions involved in the production of this emission can be written as:

$$NO + M \rightarrow NO(v = 1) + M \qquad (k_{01}) \tag{2.1}$$

$$NO(v = 1) + M \rightarrow NO(v = 0) + M^* \qquad (k_{10}) \tag{2.2}$$

$$NO(v = 1) \rightarrow NO(v = 0) + h\nu \qquad (A_{10}) \tag{2.3}$$

where v refers to the vibrational state of the molecule, k_{01} and k_{10} refer to the rate coefficient for collisional excitation and de-excitation respectively, and A_{10} refers to the Einstein coefficient for radiative de-excitation. In Equation 2.3, $h\nu$ denotes the energy of the photon emitted where h is Planck's constant and ν is the frequency of the photon. Laboratory measurements (Murphy et al., 1975) have shown that the rate coefficients for Eq. 2.1 and 2.2 involving N_2 and O_2 are a few orders of magnitude smaller than that involving O. As

a result, atomic oxygen is the dominant source of vibrational excitation (and quenching) of NO in the thermosphere.

The rate coefficients k_{01} and k_{10} are related by the expression:

$$k_{01} = k_{10}\ e^{-h\nu/kT} \tag{2.4}$$

where k is Boltmann's constant and T is the neutral temperature. Assuming photochemical equilibrium, the population of the $v = 1$ level can be given as the ratio of the associated net production rate and loss frequency:

$$[NO(v=1)] = \frac{k_{01}[NO(v=0)][O]}{k_{10}[O] + A_{10}} \tag{2.5}$$

where the square brackets denote number densities. Using Eq. 2.4 the above equation can be re-written as:

$$[NO(v=1)] = \frac{[NO(v=0)][O]k_{10}\ e^{-h\nu/kT}}{k_{10}[O] + A_{10}} \tag{2.6}$$

The energy loss rate from an optically thin atmosphere due to the infrared emissions from NO can then be written as the product of the energy of a 5.3 µm photon, the transition probability of the $v = 1$ level resulting in the emission of a photon, and the level population:

$$L_{NO} = h\nu\ A_{10}\ [NO_{v=0}]\ \omega\ e^{-h\nu/kT} \tag{2.7}$$

where

$$\omega = \frac{k_{10}\ [O]}{k_{10}\ [O] + A_{10}} \tag{2.8}$$

Here ω is a 'dilution' factor, denoting the departure of the NO($v = 1$) population from local thermodynamic equilibrium (LTE). When the collisional loss frequency is much larger than the radiative loss frequency ($k_{10}[O] \gg A_{10}$), ω is approximately equal to 1 and the level population is in thermodynamic equilibrium, described by a Boltzmann distribution. However as shown in Figure 2.1 and 2.2, this condition does not hold true in the thermosphere where radiative lifetimes (on the order of a tenth of a second or less) are much smaller than the collisional lifetimes, which increase as a result of decreasing atomic oxygen densities above 100 km. Thus vibrationally excited NO molecules predominantly return to the ground state by means of radiative de-excitation, and Eq. 2.1 and 2.3 serve as an efficient channel for energy loss from the thermosphere.

Another potential source of energy loss from the thermosphere is the nascent vibrational excitation of nitric oxide as it is created in the thermosphere. Experimental (Whitson et al.,

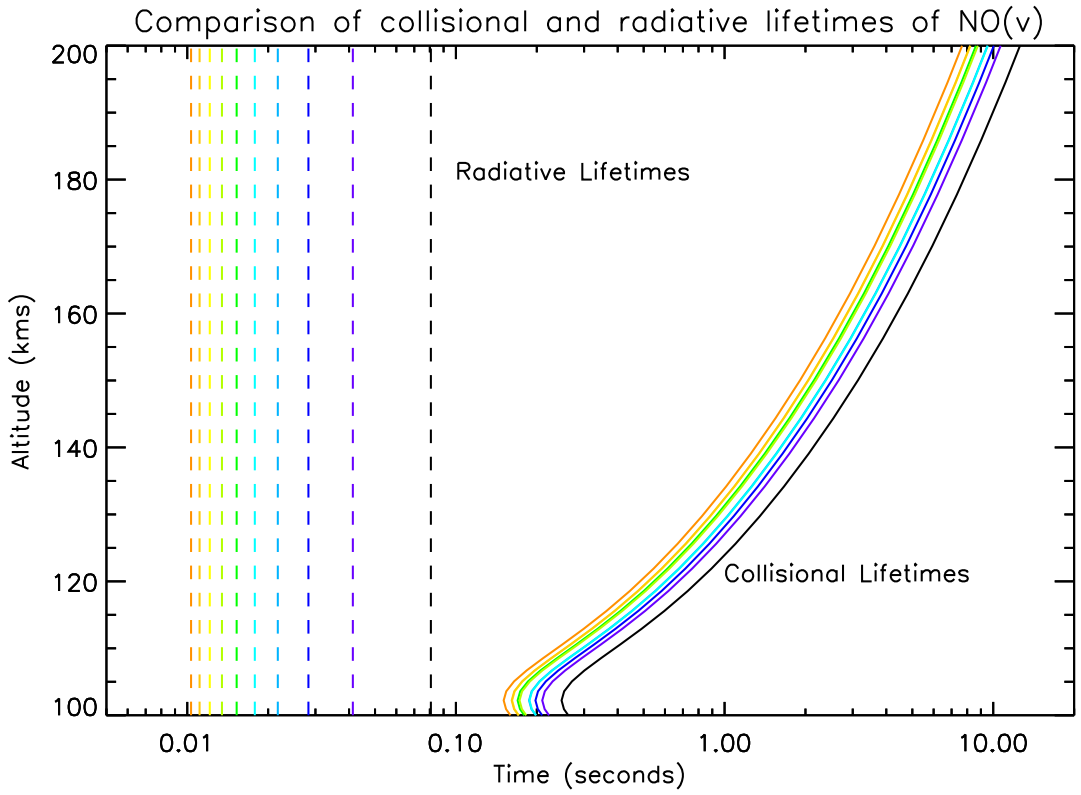

Figure 2.1: Comparison of radiative and collisional lifetimes for various vibrational levels in the thermosphere, where black corresponds to $v = 1$ and orange corresponds to $v = 10$. Both radiative and collisional lifetimes decrease with increasing vibrational level, but for a given vibrational level it is seen that radiative losses generally dominate in the thermosphere. Radiative lifetimes are calculated by accounting for the possibility of a $\Delta v = 1$ or $\Delta v = 2$ transition for each level, while collisional lifetimes are calculated by using the net rate coefficient of a given level being quenched to any lower lying level.

1976; Kennealy et al., 1978; Winkler et al., 1986; Rawlins et al., 1989) and theoretical studies (Duff et al., 1994; Braunstein and Duff, 2000; Caledonia et al., 2000; Miquel et al., 2003; Sultanov and Balakrishnan, 2006) have examined the primary processes that produce NO in thermosphere - the exothermic reactions of atomic nitrogen with molecular oxygen - and have shown them to be signicant sources of vibrationally excited nitric oxide:

$$N(^4S) + O_2 \rightarrow NO(v \geq 1) + O \tag{2.9}$$

$$N(^2D) + O_2 \rightarrow NO(v \geq 1) + O \tag{2.10}$$

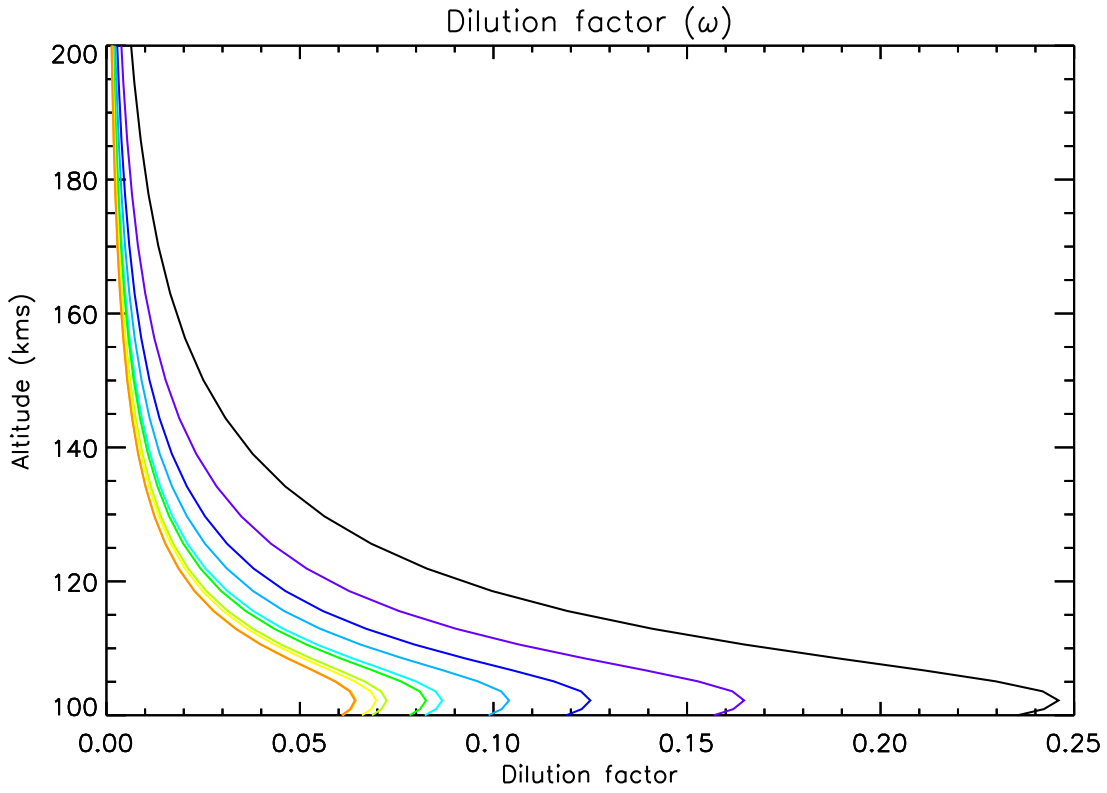

Figure 2.2: The dilution factor ω for vibrational levels $v = 1 - 10$, where black corresponds to $v = 1$ and orange corresponds to $v = 10$. The dilution factor serves as a measure of the vibrational level populations departing from LTE, where a value of $\omega = 1$ indicates LTE, and a lower value indicates the extent to which the level population is less than that of the expected Boltzmann distribution.

where N(^{4}S) and N(^{2}D) are the ground and excited state atomic nitrogen respectively. These reactions are exothermic by 1.4 and 3.77 eV respectively (Kennealy et al., 1978), and can potentially create NO($v = 6$) and NO($v = 16$) which may consequently radiatively de-excite or be quenched to a lower level:

$$NO(v) \rightarrow NO(v' < v) + h\nu \quad (\Delta v = 1, 2) \tag{2.11}$$

$$NO(v) + O \rightarrow NO(v' < v) + O^* \tag{2.12}$$

Similar to the case for the $v = 1$ level, the radiative lifetimes of these higher vibrational levels is much smaller than their collisional lifetimes (Fig. 2.1) in the thermosphere, and it is possible for the NO molecule to return to its ground state purely by means of radiative de-excitation, emitting multiple photons. These processes indicate the existence of an airglow mechanism that is concurrent with energy deposition and nitric oxide production in

the thermosphere. As existing thermospheric models do not account for this process, it is necessary to investigate the role played by this emission in the thermospheric energy budget. The primary goal of the work presented in this chapter is to calculate the magnitude of the emission produced from Eq. 2.9-2.12, and quantify its importance to the thermospheric energy budget.

2.2 Modeling NO($v \leq 10$) populations

2.2.1 Vibrational level distributions

Knowledge regarding the fraction of NO molecules initially excited to each accessible vibrational level (i.e., the fractional yield for each product channel) from from Eq. 2.9 and 2.10 is of primary importance when calculating the steady state level populations for NO($v \leq 10$). In this section we discuss the various values that have been presented in literature and the justification for those used in the present work.

The vibrational level yields from N(^{4}S) have been the subject of experimental (Whitson et al., 1976; Winkler et al., 1986) and theoretical (Caledonia et al., 2000; Duff et al., 1994; Sultanov and Balakrishnan, 2006) studies. Except for the result discussed by Caledonia et al. (2000) which was obtained for NO production from superthermal N(^{4}S), these studies are in reasonable agreement with each other. The theoretical values most recently presented by Sultanov and Balakrishnan (2006) have been used here. Their calculations for yields for $v = 0 - 8$ have been extrapolated to obtain the yields for $v = 9$ and 10. These additional vibrational levels however contribute less than 2% of the total yield and including them does not change the average vibrational level excited significantly. On average, the N(^{4}S) + O_2 reaction produces an NO molecule excited to the $v = 4$ level.

While there are similar studies regarding the vibrational yields from N(^{2}D), the nature of the products has been a subject of some debate. Kennealy et al. (1978) and Rawlins et al. (1989) provided initial measures of the vibrational distributions, suggesting a relatively uniform yield of 10% for $v = 1 - 7$, beyond which the distribution decreased monotonically. However, both these studies interpreted their results assuming two product channels for the atomic oxygen produced, the ground state O(^{3}P) and the electronically excited O(^{1}D). Miller and Hunter (2004) have since shown the reaction to strongly prefer the O(^{3}P) channel, and theoretical calculations of the vibrational distribution assuming this channel have been presented by Braunstein and Duff (2000) and Miquel et al. (2003). We use the values given by Miquel et al. (2003) for a collision energy of 0.039 eV, which is typical for the reactants at 300 K. As the model presented here only calculates populations for NO($v \leq 10$), we add the yields calculated for $v > 10$ given by Miquel et al. (2003) into the yield for $v = 10$. The average vibrational level excited from the N(^{2}D) + O_2 reaction is calculated to be $v = 6$. The vibrational distributions from Eq. 2.10 and 2.9 used in this work are shown in Figure

2.3, and have been tabulated in Table 2.1.

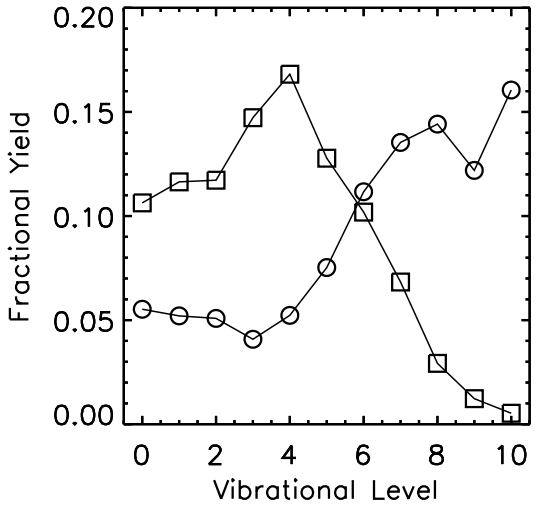

Figure 2.3: Nascent vibrational level distributions for the NO produced from Eq. 2.9 and 2.10. The yields from N(^{4}S) are denoted by squares, that from N(^{2}D) are denoted by circles. Yields for $v > 10$ from N(^{2}D) presented by Miquel et al. (2003) have been summed into the yield of $v = 10$, while the yields for $v = 9, 10$ from N(^{4}S) where obtained by extrapolating the values presented by Sultanov and Balakrishnan (2006).

Table 2.1: Vibrational level yields for NO(v) from Eq. 2.10 and 2.9

Vibrational level	N(^{2}D)	N(^{4}S)
0	0.055	0.106
1	0.052	0.116
2	0.051	0.117
3	0.041	0.147
4	0.052	0.168
5	0.075	0.128
6	0.112	0.102
7	0.135	0.068
8	0.144	0.029
9	0.122	0.012
10	0.161	0.007

The exothermic reactions of $N(^2P) + O_2$, $N_2(A) + O$ and $N^+ + O_2$ are relatively minor sources of nitric oxide in the thermosphere and are not considered here as the vibrational

distribution of the product NO from them is currently not known.

2.2.2 Relevant rate coefficients

The rate coefficient for the vibrational excitation of NO by collisions with atomic oxygen is generally determined by studying the reverse reaction, i.e. the collisional quenching of NO($v = 1$) by atomic oxygen, and using the relationship given in Eq. 2.4. Several values have been presented and used over the years for aeronomic calculations, with Kockarts (1980) and Roble et al. (1987) using a value of 6.5×10^{-11} cm^3 s^{-1}, Sharma et al. (1998) using a value of 2.8×10^{-11} cm^3 s^{-1}, and Lu et al. (2010) using a value of 4.2×10^{-11} cm^3 s^{-1}. Current thermospheric models generally follow the value used by Lu et al. (2010), obtained from the results presented by Hwang et al. (2003). For reasons outlined below, however, we suggest that this value may be an overestimate.

First, the results of Hwang et al. (2003) are in notable contrast to others (Dodd et al., 1996, 1999; Duff and Sharma, 1997; Caridade et al., 2008) that have shown the rate coefficient to be smaller by almost a factor of two. Secondly, Hwang et al. (2003) posited the higher value partly in response to the work done by Sharma and Roble (2001), where the use of a lower value for the rate coefficient resulted in model calculations of thermospheric temperatures and densities that were in significant disagreement with those obtained from MSIS. Sharma and Roble (2001) resolved this discrepancy by increasing the CO_2 cooling rate by a factor of two, though they noted this increase to be at odds with existing lab measurements of the CO_2 cooling rate. Measurements of the CO_2 cooling rate since then by Shved et al. (2003) and Castle et al. (2012) suggest that the CO_2-O de-excitation rate adopted by Sharma and Roble (2001) was indeed an overestimate by a factor of 2-7 in the lower thermosphere (Fig. 2.4), and cannot be used to explain the discrepancy between MSIS and the model.

However, the Global Mean Model used by Sharma and Roble (2001) scales down the radiative cooling effect of O(^{3}P) by a factor of two (Roble et al., 1987) to account for non-LTE effects following the suggestion of Offermann and Grossmann (1978). This assumption has been noted to be inaccurate by Sharma et al. (1994) and Grossmann and Vollmann (1997). Lastly, the reduction in the heating efficiency of the N(^{2}D) and N(^{4}S) reactions with O_2 due to the chemiluminescent emission mechanism discussed here has not been accounted for in previous thermospheric models.

To reflect our current understanding of energy loss from the thermosphere and resolve the above discrepancies, we assume the following rates and processes:

1. The "unscaled" O(^{3}P) cooling rate from Kockarts and Peetermans (1970),
2. The collisional excitation rate of NO due to collisions with atomic oxygen (2.1×10^{-11} cm^3 s^{-1}) from Caridade et al. (2008),
3. Energy loss from the thermosphere due to the chemiluminescence of NO.

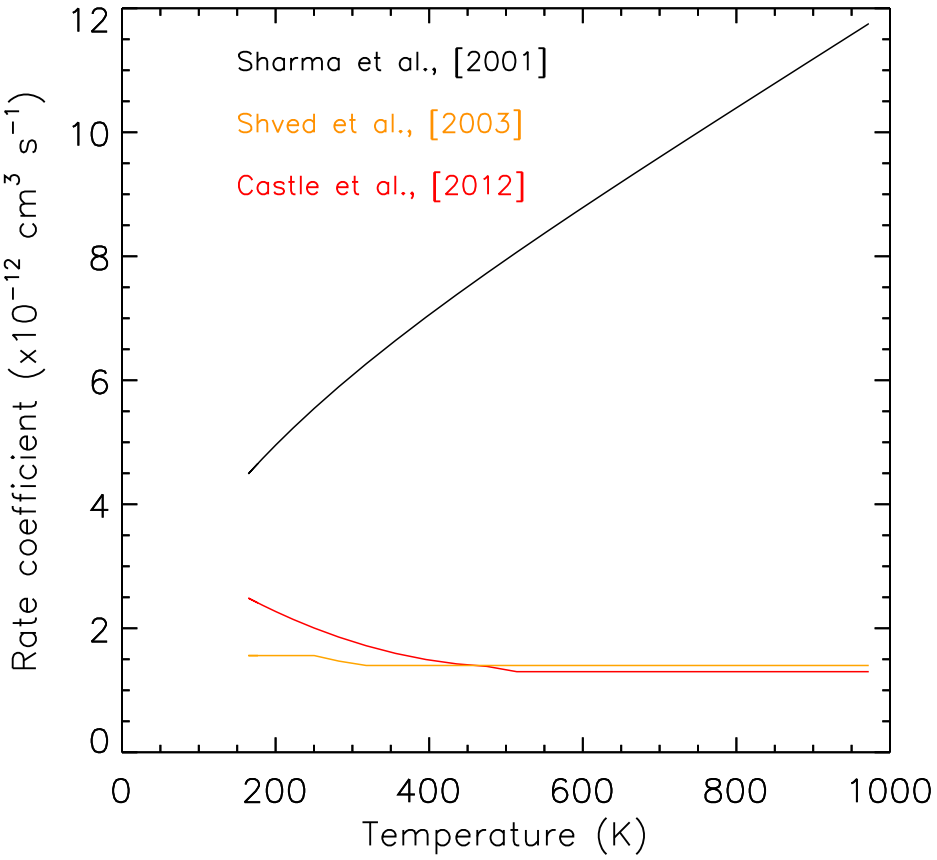

Figure 2.4: Comparison of rate coefficients for vibrational relaxation of CO_2 by $O(^3P)$.

Non-thermal $N(^4S)$ has been previously considered as a significant source of thermospheric nitric oxide (Gérard et al., 1997; Swaminathan et al., 1998) and is known to be the source of 5.3 µm emissions from rotationally and vibrationally excited NO in the thermosphere (Hubert et al., 1996; Sharma et al., 1998). However, Balakrishnan et al. (2000) have shown the contribution from non-thermal $N(^4S)$ to be small compared to that of $N(^2D)$ and thermal $N(^4S)$ in the thermosphere, and Swaminathan et al. (2001) have shown that agreement between modeled and measured NO densities can be improved instead by considering increased $N(^2D)$ yields from NO^+ recombination and increased scaling factors for solar EUV and soft X-ray fluxes. As a result, we do not consider the production of NO from non-thermal $N(^4S)$ in the present study.

The Einstein coefficients for the $\Delta v = 1$ and 2 transitions were found to be approximately constant over thermospheric temperatures, and the values presented at 300 K in Table 5 and 6 of Rawlins et al. (1998) have been used here.

2.2.3 Model

Accounting for the processes described in section 2.2, the vibrational levels of nitric oxide are populated by the following processes: 1) the reaction of N(^{2}D) and N(^{4}S) with O_2, 2) by cascade from a higher vibrational level via collisional quenching, or 3) via radiative de-excitation. Further, it is depopulated by 1) the emission of a 5.3 or 2.7 µm photon, 2) quenching by atomic oxygen to a lower level, and 3) loss via chemical processes. The vibrational level populations can then be assumed to be in photochemical equilibrium, expressed as:

$$\left(\sum_{v<v'}(A_{v,v'}+[O]k_{v,v'})+\sum_j L_j\right)[NO(v)] = \sum_{v''>v}(k_{v'',v}[O]+A_{v'',v})[NO(v'')]+\sum_i g_i(v)P_i \quad (2.13)$$

where the terms on the left and right hand side of the equation denote the net loss frequencies and production rates associated with the vibrational level v. In the above equation, [NO(v)] denotes the population of a specific vibrational level and $A_{i,j}$ denotes the Einstein coefficient for radiative de-excitation from the level i to a lower level j. Similarly, $k_{i,j}$ denotes the rate coefficient for quenching of NO by atomic oxygen from level i to a lower level j. The chemical losses are denoted by the summation over L, while the yield into a vibrational level from reactions Eq. 2.10 and 2.9 is represented as a summation over production rates P with the level specific yield $g(v)$.

For a set of vibrational levels, the above equation becomes a system of equations:

$$\bar{L}\bar{x} = \bar{P}, \quad (2.14)$$

where the matrices $\bar{L}$, $\bar{P}$, and $\bar{x}$ denote the loss, production and the populations of the vibrational levels being solved for, with the production terms due to collisional quenching and radiative cascade absorbed into the loss matrix. This equation is solved to obtain the density of NO($v \leq 10$) at a given altitude, which are then multiplied by the appropriate Einstein coefficients and photon energies to obtain the energy volume emission rates for the fundamental and overtone emission from each level.

2.2.4 The Thermosphere-Ionosphere-Electrodynamics General Circulation Model (TIE-GCM)

The TIE-GCM (Richmond et al., 1992) is a self-consistent, first principles, general circulation model that solves the continuity and energy equations for the coupled thermosphere and ionosphere at a 2 minute time step, producing a representation of the upper atmospheric structure in terms of winds, temperatures and densities of various neutral and charged species. The primary input to the model is solar fluxes specified between $0.05 - 175$ nm, with high latitude energy inputs obtained from parameterized calculations using the K_p index. In order to obtain a global calculation of the chemiluminescent emission, we incorporate the model

described in section 2.2.3 into the TIE-GCM and solve Equation 2.13 at each time step. The TIE-GCM runs presented here were made using a horizontal resolution of $5^\circ \times 5^\circ$, and a vertical resolution of half a scale height. Apart from the processes listed in section 2.2.2, the model was updated in the present work to use the temperature dependent rate coefficient suggested by Duff et al. (2003) in Eq. 2.10.

2.3 Results

2.3.1 Comparison with CIRRIS-1A data

Since the photons emitted from the vibrational levels of nitric oxide have similar energies, it is not straightforward to distinguish between emissions produced as a result of collisional excitation and chemical excitation. One approach that may be used to identify the secondary emission is observing the 2.7 µm overtone emission from NO, corresponding to a Δv = 2 transition is produced only from the higher vibrational levels (v$\geq$2) of NO. As the vibrational levels in NO are separated by approximately 0.23 eV, excitation of the $v \geq 2$ levels via inelastic collisions with atomic oxygen is unlikely to occur in the thermosphere, and solar pumping from the ground state to $v = 2$ is known to be a negligible source of excitation (Sharma et al., 2000). It can then be assumed that the higher vibrational levels are initially populated only by means of chemical processes, and the overtone emission is completely chemical in origin. We can thus validate our model by comparing our calculations of the 2.7 µm emission with measurements. The Cryogenic Infrared Radiance Instrumentation for Shuttle (CIRRIS-1A) was flown aboard the Space Shuttle Discovery between 29 April and 1 May 1991 (Ahmadjian et al., 1990). The payload consisted of a Michelson interferometer, a radiometer, and an IR telescope which were used in tandem to obtain high spectral and spatial resolution limb measurements of infrared emissions from the Earth's atmosphere in the 2.5 - 25 µm wavelength region (Wise et al., 2001). Observations were made between $\pm 68^\circ$ latitude for moderate to high levels of geomagnetic activity (K_p = 3 - 7). Daytime measurements of the emission were collected in the Northern Hemisphere with the solar zenith angle varying between 60 and 90° for low (15°) to middle (45°) latitudes. The 2.7 µm overtone emission from NO was measured in the 2.5 - 3.4 µm band pass of the radiometer, which also recorded emission from CO_2 , H_2O, and OH near 2.7 µm. However, these emissions are not detectable above 100 km and do not interfere with the measurement of the emission from nitric oxide. The instrument noise for this band pass is approximately 0.13 ergs cm^{-2} s^{-1}. In Figure 2.5, we plot the modeled and measured line-of-sight column emission along with the instrument noise as a function of altitude for the low and middle latitude cases. The modeled peak column emission rates vary between 0.2 and 0.28 ergs cm^{-2} s^{-1} and are in reasonable agreement with the measurements.

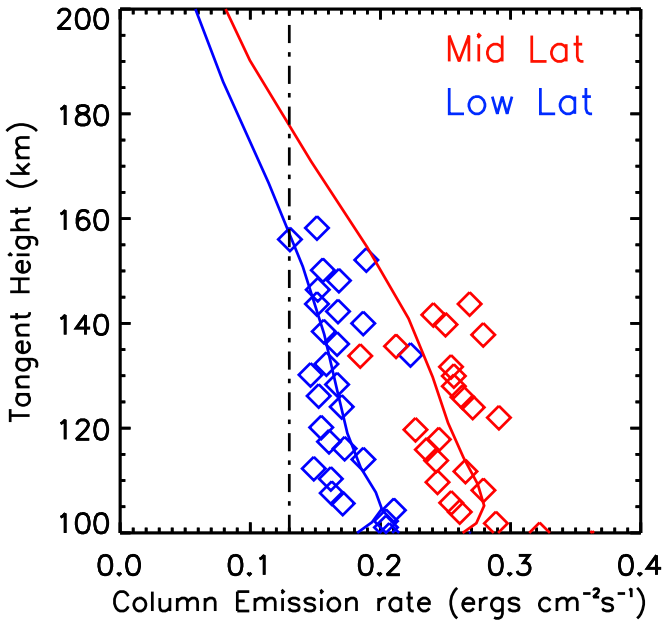

Figure 2.5: Comparison of CIRRIS-1A data with the modeled (diamonds = data and solid line = model), zonally averaged, 2.7 µm emission for April 19th, 1991 for low latitudes (blue) and mid-latitudes (red) along with instrument noise (dash dotted).

2.3.2 Model calculations for 2003 spring equinox

In Figure 2.6 we plot the modeled equatorial column emission rates from thermal collisions and chemiluminescence as a function of local time for typical thermospheric conditions (F10.7d = 90.3, F10.7a = 126, K_p = 2-5) on day 80 of 2003. The column emission rates are obtained by integrating the volume emission rates between the lowest (97 km) and highest (> 500 km) grid points of the TIE-GCM calculations, though majority of the emission from either case is from below 200 km. It can be seen that the peak daytime contribution of chemiluminescence occurs near noon where it is approximately 40% of the total emission, and varies between 0.2-12.8$\times$ 10^{-2} ergs cm^{-2} s^{-1} from midnight to noon. The emission from both processes show a strong diurnal variation, although the underlying drivers in each case are different. The emission produced by collisional excitation varies as a function of NO densities and neutral temperatures, while variations in the chemiluminescence reflects the local production rate of NO in the thermosphere. Thus at low latitudes the emission is a function of the EUV energy deposition and the solar zenith angle. Since the production of N(^{2}D) at low latitudes ceases after sunset, the main driver for NO production is from N(^{4}S) above 150 km. The 2.7 µm column emission rate is on average 14% of the total chemiluminescence.

Figure 2.7(a) shows the model calculations of the different sources for NO($v = 1$) for equato-

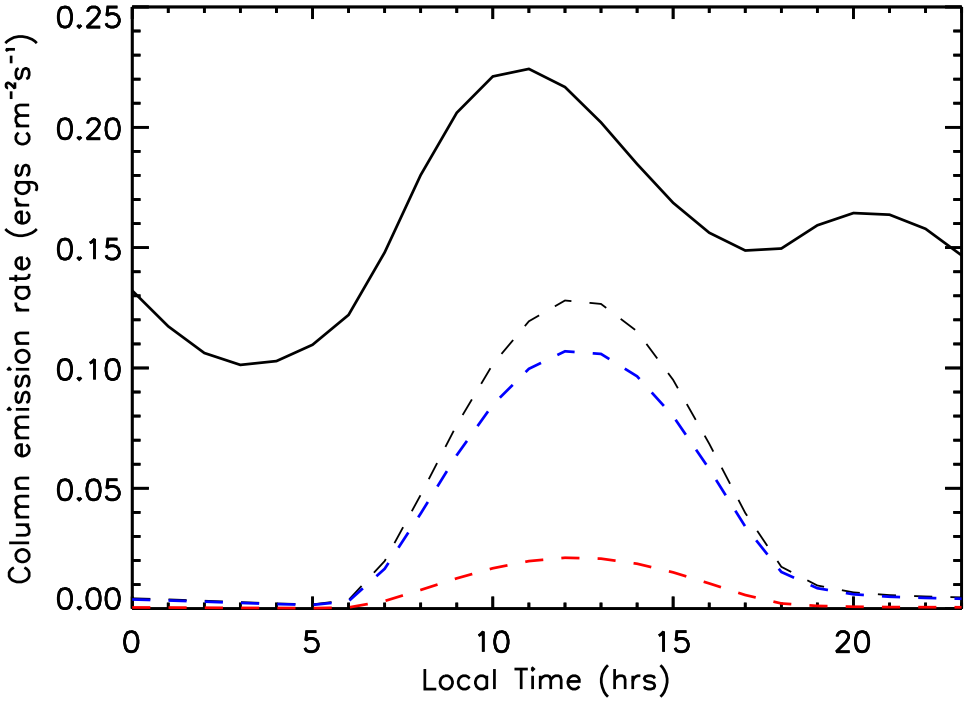

Figure 2.6: Diurnal variation of different sources of thermospheric IR emissions from nitric oxide for day of 2003 at the equator. Solid black line corresponds to emissions as a result of thermal excitation, and the dotted black line corresponds to chemiluminescent emission. Also shown are the individual contributions of the fundamental 5.3 µm (blue dashed) and overtone (red dashed) emissions.

rial noon. As expected, the dominant source of the first vibrationally excited level above 120 km is thermal collisions between NO($v = 0$) and atomic oxygen. Below 105 km, secondary processes become the dominant source of NO(v = 1), and collisional excitation is a negligible contributor. In particular, cascade via radiative deexcitation and collisional quenching from $v = 2$ accounts for nearly 70% of the production of the $v = 1$ level population. While radiative pumping by sunshine and earthshine influence the NO ($v = 1$) population below 120 km (Funke and López-Puertas, 2000; Sharma et al., 1998), these processes contribute to less than 2% of the total emission and have not been considered here. We plot the calculated vibrational level densities for the first four vibrational levels in Figure 2.7(b), distinguishing between NO(v = 1) produced via thermal collisions and chemiluminescence. It is important to note that though the net population of chemically produced NO(v) is less than that produced via collisional excitation, these molecules tend to return to the ground state purely via radiative de-excitation producing multiple photons on average, as compared to the single photon produced as a result of collisional excitation.

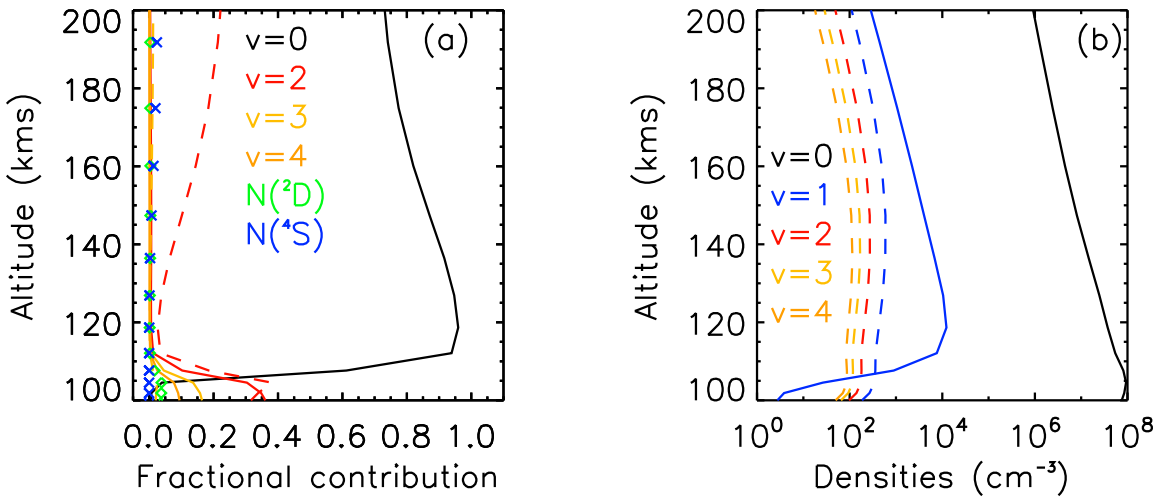

Figure 2.7: (a) Fractional contribution of sources to NO($v = 1$) production in the thermosphere. Production due to collisions of NO($v = 0$) with atomic oxygen has been shown in black. Production due to radiative cascade from higher vibrational levels is shown by dashed lines, while cascade via collisional quenching is shown by solid lines. Also shown are the direct population by N(^{2}D) (green diamonds) and N(^{4}S) (blue crosses). (b) Model calculations of vibrational level populations for NO($v = 0 - 4$), with the solid blue line showing NO(v = 1) produced only by thermal collisions and the dashed lines showing production as a result of Eq. 2.9 - 2.12.

In Figure 2.8(a) the equatorial volume emission rates from thermal collisions and chemiluminescence at noon are plotted as a function of altitude, along with their fractional contribution to the total emission. The emission produced from thermal collisions has a peak value of 6.3×10^{-8} ergs cm^{-3} s^{-1} near 120 km, while chemiluminescence peaks near 135 km and has a maximum value of 1.7×10^{-8} ergs cm^{-3} s^{-1}. Below 110 km where the radiative lifetimes are comparable to the collisional lifetimes, chemiluminescence is the dominant source of the emissions, as highly vibrationally excited NO may still emit after being quenched to a lower level. Above 160 km chemical and collisional processes are seen to contribute equally to thermospheric energy loss. The components of the chemiluminescent emission have been plotted as a function of altitude in Figures 2.8(b) - 2.8(d). In Figure 2.8(b) we plot the volume emission rates for $v = 1$, 2 and $v \geq 3$. The higher vibrational levels (v≥3) have a peak volume emission rate of 1.14×10^{-8} ergs cm^{-3} s^{-1} near 135 km and contribute to about 75% of the chemiluminescence between 100 and 200 km on average, while the contributions from $v = 1$ and 2 are approximately equal. Vibrationally excited NO produced by N(^{2}D) is the dominant source of the emission in the sunlit thermosphere, contributing to 77% of the emission near 135 km and contributes approximately 40% on average to the total emission (2.8(c)). Recalling that the production of NO from N(^{4}S) is strongly temperature dependent,

NO production from this process contributes to the emission predominantly above 150 km. The transition probabilities for the 2.7 µm emission are smaller than those for the 5.3 µm emission as the $\Delta v = 2$ transition is not favored by quantum mechanical selection rules. As a result, the overtone emission is generally weaker than the $\Delta v = 1$ emissions. The maximum energy loss rate due to it is 2.8×10^{-8} ergs cm^{-3} s^{-1} at 135 km and is on average 15% of the total chemiluminescence (2.8(d)). The individual components of NO emissions as a function of latitude and longitude/local time are shown in Figure 2.9, while the contribution of chemiluminescence to the total column-integrated emissions from NO has been plotted in Figure 2.10. Both figures correspond to 12:00 UT. The emission shows a strong dependence on the solar zenith angle and is a significant contributor to thermospheric 5.3 µm emissions in the sunlit hemisphere at low and middle latitudes, with a minimum value of 8×10^{-4} ergs cm^{-2} s^{-1} and a maximum value of 13.2 ergs cm^{-2} s^{-1}. Chemiluminescence accounts for 25 - 40% of the column emissions produced during noon at these latitudes and contributes similarly at high latitudes (between 65° and 75° in both hemispheres) where energetic particle precipitation causes the ionization and dissociation of N_2, driving the production of NO.

2.3.3 Effect on Neutral Temperatures

The infrared emissions produced as a consequence of vibrational excitation of the NO produced from the $N(^2D)/N(^4S) + O_2$ reaction is not a cooling in the strictest sense of the word, as this implies that the process extracts energy from the background thermosphere and radiates it away. Instead, chemiluminescence of NO reduces the effective exothermicity of these reactions, removing energy from the thermosphere before it becomes part of the energy budget. While the net effect is a reduction in the modeled neutral temperatures of the thermosphere, it is necessary to make this distinction in order to accurately account for the process in numerical models.

Figure 2.11 shows the difference in modeled exospheric temperatures after accounting for the effect of the additional emission for the case of day 80 of 2003. The process results in an overall reduction of 2-3% in the exospheric temperatures, with the largest reductions occuring on the dayside at low to mid latitudes. Including this process does not significantly alter the global mean temperature structure below 150 km, as downward molecular conduction of heat from above this altitude compensates for the reduction in heating. The process however results in a net reduction of global mean exospheric temperatures by 27 K ($\approx 2.7\%$).

2.4 Parameterization

It is computationally expensive to solve the matrix equation (Eq. 2.13) at every time step to obtain the vibrational level populations of NO, especially for use in global atmospheric models. A parameterization scheme is presented here that approximates the emission rates from

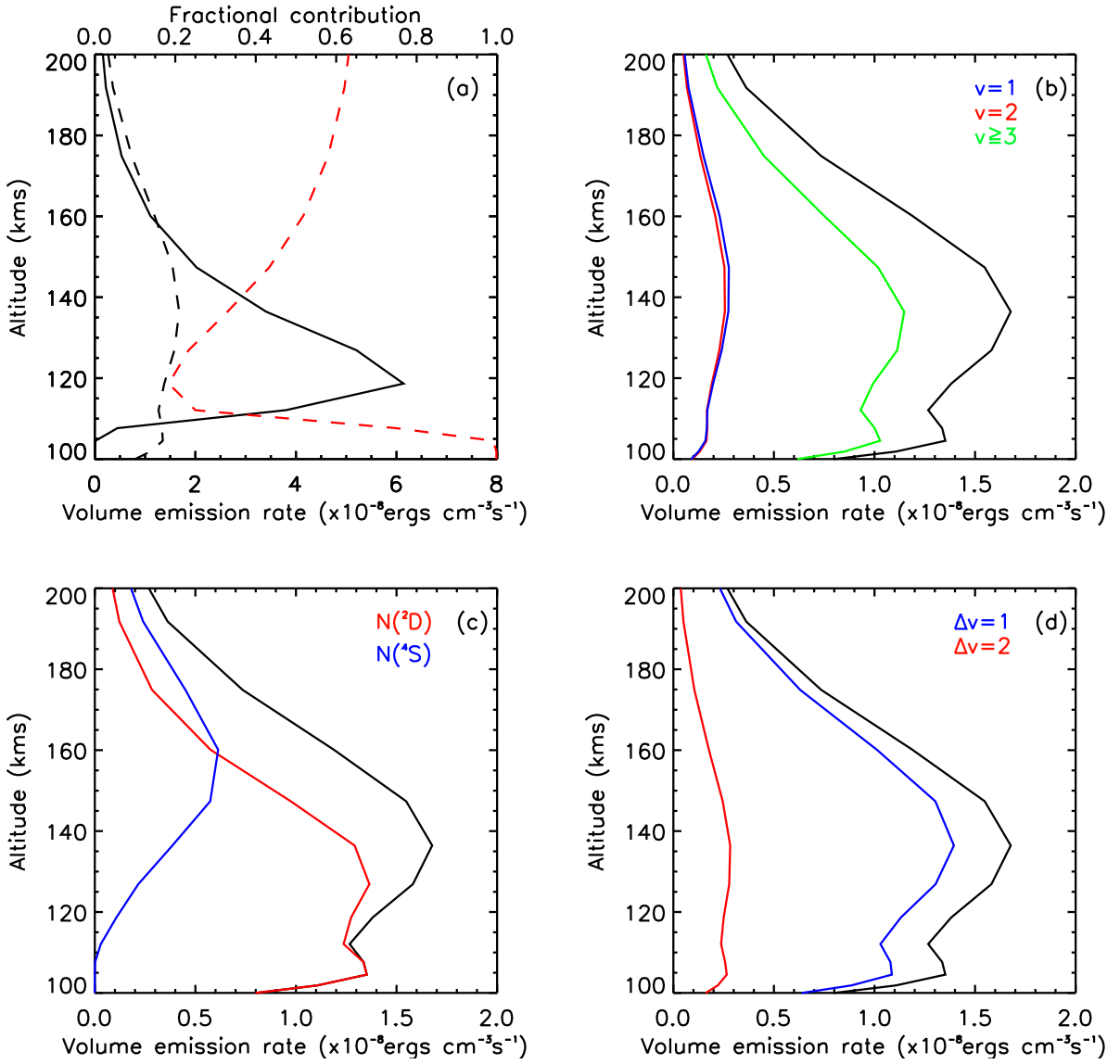

Figure 2.8: (a) Comparison of the NO IR emissions due to thermal collisions (solid black) and chemiluminescence (dashed black). Also shown is the fractional contribution of chemiluminescence (dashed red); The net chemiluminescent emission produced (black) compared to (b) emissions from $v = 1$ (dark blue), $v = 2$ (red) and $v \geq 3$ (green); (c) emission produced by N(^{2}D) (red) and N(^{4}S) (blue) and (d) emissions due to the Δv = 1, 5.3 µm transitions (blue) and the Δv = 2, 2.7 µm transitions (red). All the above plots correspond to day 80 of 2003, equatorial noon.

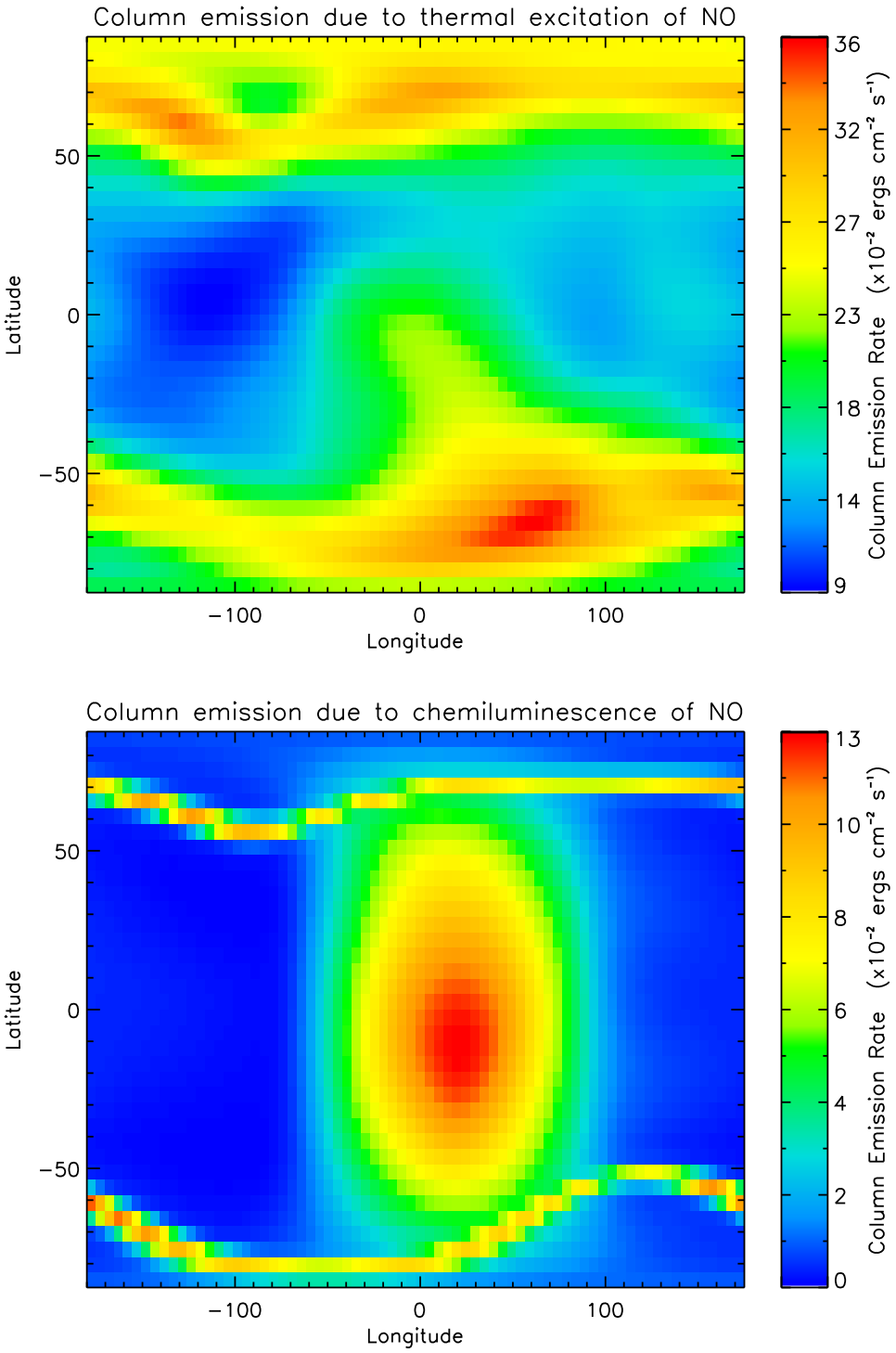

Figure 2.9: Column integrated NO emissions as a result of collisional excitation (top) and that from chemiluminescence (bottom) at noon UT for day 80 of 2003.

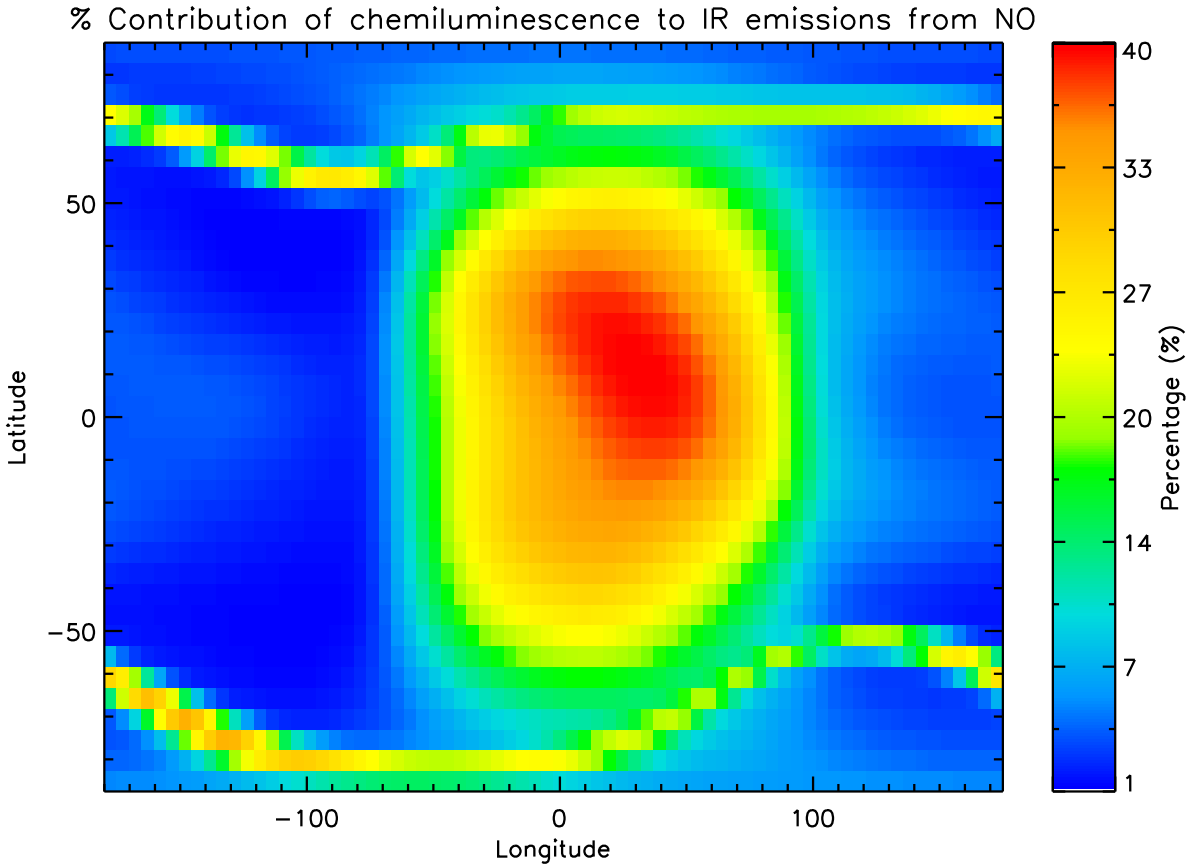

Figure 2.10: Ratio of the contribution of column-integrated chemiluminescence to total emissions from nitric oxide at noon, day 80 of 2003.

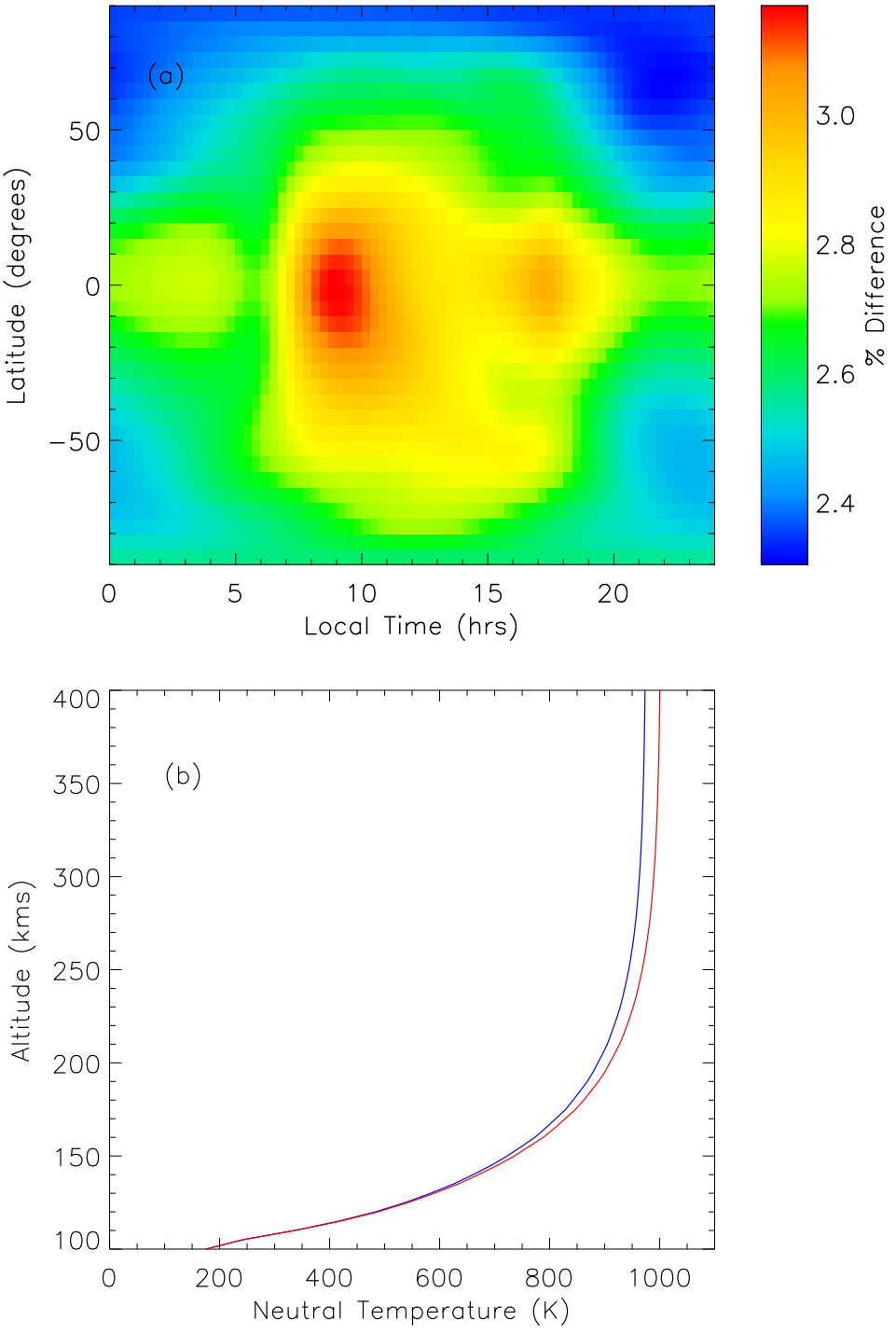

Figure 2.11: Effect of including chemiluminescence in TIE-GCM on modeled thermospheric temperatures. (a) Percentage difference in zonally averaged neutral temperatures at 400 km; (b) Global mean neutral temperatures with chemiluminescence included in the model run (blue) and without (red).

a given vibrational level, without the need to explicity solve for individual level populations.

As shown in Figure 2.1, the radiative lifetimes of the vibrational levels of NO are much shorter than their respective collisional lifetimes above 100 km, and it can be assumed that a NO($v = n$) molecule will return to the ground state only by means of $\Delta\ v = 1$ or $\Delta\ v = 2$ radiative transitions. We can then ignore the population of a given vibrational level by means of collisional quenching from a higher vibrational level, and express the level population as a balance between its chemical production processes and the radiative and collisional losses. The energy loss rate from a NO($v = n$) molecule returning to the ground state only by means of $\Delta\ v = 1$ transitions can then be approximated as:

$$E_{NO(v=n)} = n\ h\nu\ \frac{\overline{A_{\Delta v=1}}}{\overline{A_{\Delta v=1}} + \overline{A_{\Delta v=2}} + f\overline{k}[O]} \sum_i g_i(v_n) P_i \tag{2.15}$$

where we use the Einstein coefficients $\overline{A_{\Delta v=1}}$ and $\overline{A_{\Delta v=2}}$ averaged across $v \leq n$ for the $\Delta v = 1$ and $\Delta v = 2$ transitions respectively, and $\overline{k}$ denotes the average collisional quenching rate from a given level. As before, $g_i(v_n)$ refers to the vibrational yield from processes P_i, referring to production from N(^{2}D) and N(^{4}S). The energy loss rate due to the 2.7 µm emission can be calculated similarly, assuming a $v = n$ level returns to the lowest possible level by means of $\Delta v = 2$ transitions. A parameterization factor of f=13.5 is used to obtain the best fit between the full calculation and the above parameterization. The values used for $\overline{A_{\Delta v=1}}$ and $\overline{A_{\Delta v=2}}$ are given in Table 2.2.

Table 2.2: $\overline{A}$ and $\overline{k}$ used for parameterized calculation of chemiluminescence from NO

Vibrational level	$\overline{A_{\Delta v=1}}$ (s^{-1})	$\overline{A_{\Delta v=2}}$ (s^{-1})	$\overline{k}$($\times 10^{-12}$ $cm^3 s^{-1}$)
0	0.0	0.0	0.0
1	12.396	0.0	21.000
2	17.901	0.786	12.390
3	22.974	1.534	8.7567
4	27.637	2.489	6.938
5	31.911	3.630	5.531
6	35.816	4.932	5.101
7	39.374	6.372	4.302
8	42.604	7.927	4.011
9	45.523	9.574	3.578
10	48.150	11.292	3.449

Figure 2.12 plots the emission rates modeled using the full calculation and the above parameterization scheme against local time and altitude for day 80 of 2003 at the equator. The

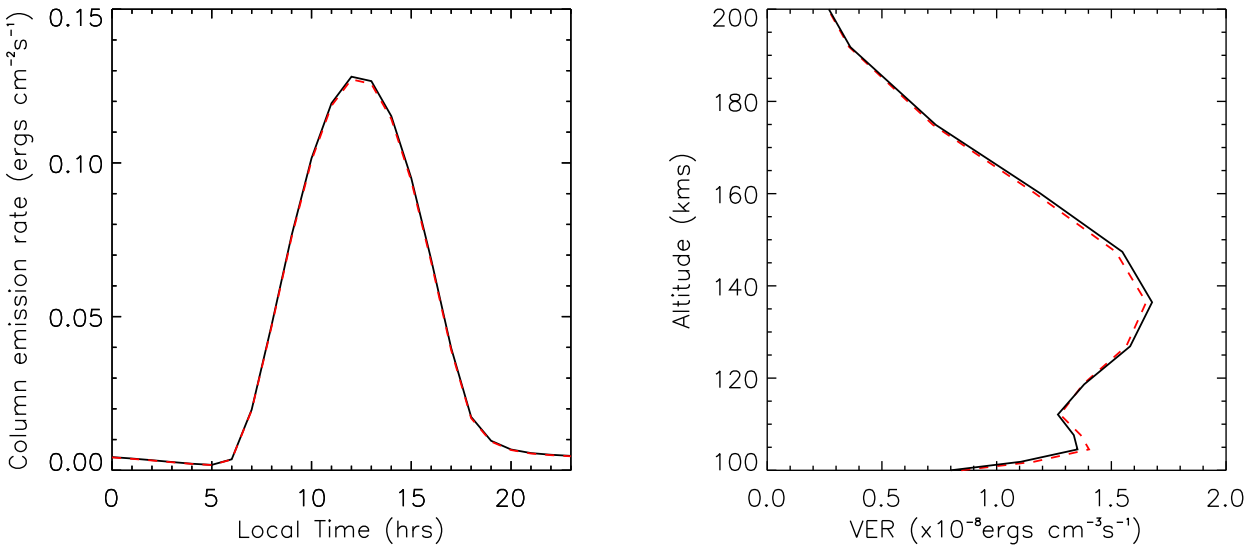

Figure 2.12: Comparison of parameterized calculation (red dashed) with full model (black) for day 80 of 2003.

plot shows that the parameterized calculation retrieves both quantities within 5% of the full calculation at all local times and altitudes, validating our assumption that vibrationally excited NO generally undergoes radiative de-excitation instead of being quenched by atomic oxygen.

The percentage difference between the full calculation E_{full} and the parameterization E_{param} for column emissions due to chemiluminescence was also calculated as a function of latitude and longitude for day 80 of 2003 as $100 \times (E_{full} - E_{param})/E_{full}$ and is shown in Figure 2.13. The parameterization is a good representation of the chemiluminescence at all latitudes on the dayside, but underestimates the column emission on the nightside. The column emission calculated using the parameterization is however within 5% of the full calculation at all latitudes and local times.

2.5 Chemiluminescence during enhancements in solar activity

As is evident from section 2.3, chemiluminescence is an importance source of thermospheric infrared emissions when nitric oxide is produced in the thermosphere, which under quiescent solar conditions occurs mainly at low latitudes on the dayside, and at auroral latitudes where energetic particle precipitation occurs. The contribution of this additional source of energy loss from the thermosphere during periods of enhanced solar activity is then worth inves-

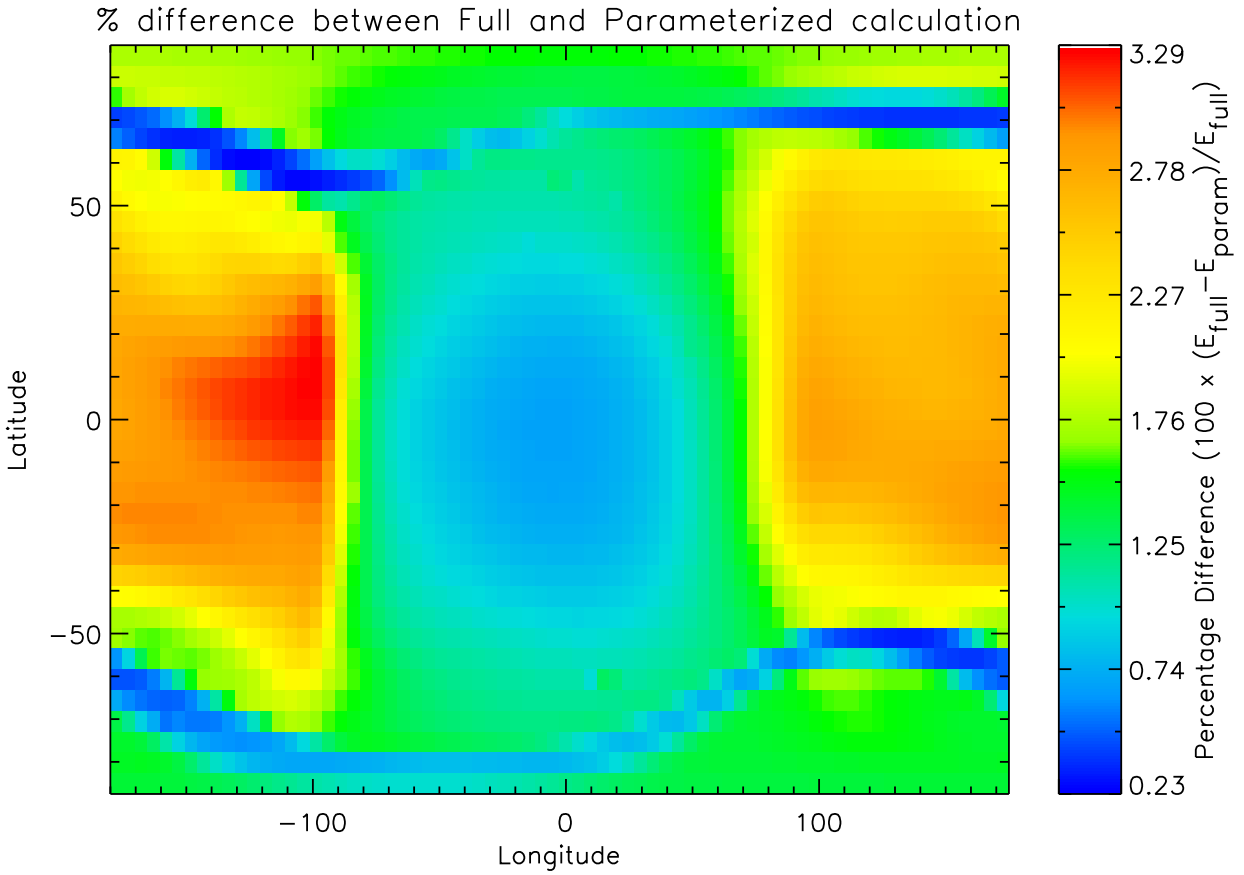

Figure 2.13: Percentage difference between calculations of chemiluminescence using full model and parameterization for day 80 of 2003.

tigating, during which NO production is known to increase significantly. As an illustrative example, we consider the geomagnetically active period during October-November 2003 and model the chemiluminescence for a solar flare and geomagnetic storm.

2.5.1 X-class Solar Flare

October 19th - November 5th 2003 was a period of high solar activity, marked by the occurrence of multiple solar flares. Among the strongest of these was an X17 flare which occurred on October 28th, during which the solar X-ray flux increased by over two orders of magnitude. The thermospheric response to this flare was modeled using the TIE-GCM, with 2 minute time resolution solar flux data from the Flare Irradiance Spectral Model (FISM) (Chamberlin et al., 2007, 2008) used to drive the model.

Figure 2.14 shows the 1-8 Å solar flux on October 28th measured by the GOES satellite, followed by model results of the zonally averaged dayside column emission due to chemiluminescence and thermal cooling, and chemiluminescence as a fraction of the total infrared emission from NO. Prior to the occurrence of the flare, the peak column emissions from the two processes are 1.97×10^{-1} and 6.94×10^{-1} ergs cm^{-2} s^{-1} respectively. The enhancement of chemiluminescence corresponds to the enhancement in the solar flux, with large increases primarily occurring at low to mid latitude and a factor of 4 increase at the subsolar point. Increases in the emission are localized to the subsolar point on the dayside hemisphere, and no significant effect from the flare was seen on the nightside emission. By comparison, the emission due to thermal collisions increases on average by 20% across all latitudes and its effects are seen well beyond the occurrence of the flare. This is due to the fact that the production rate of NO is tied to the instantaneous EUV energy deposition rate, while NO densities depend on both its production rate and loss frequencies. The increase in NO densities persist beyond the occurence of the flare and undergo diffusion and horizontal transport, resulting in additional cooling on the dayside and nightside. The zonally averaged peak emission from chemiluminescence and thermal collisions are 6.2×10^{-1} and 9.1×10^{-1} ergs cm^{-2} s^{-1} respectively. Figure 2.15 plots the contribution of chemiluminescence to total NO emissions as a function of latitude during the flare peak, where it is seen to be the dominant energy loss mechanism at the subsolar point, forming 60% of the emissions.

The components of the chemiluminescent emission at the flare peak have been plotted in Figure 2.16. Increases in the emission occur below 110 km, which reflects where the flare energy is primarily deposited. The structure of the emission in this case differs significantly from that during quiescent solar conditions, and is seen to have a peak value of 2.92×10^{-7} ergs cm $^{-3}$ s^{-1}, which is nearly twice the magnitude of the energy loss due to thermal cooling (1.51×10^{-7} ergs cm $^{-3}$ s^{-1}). On average, 65% of this additional emission is produced from the v$\geq$3 levels, with nearly equal contributions from the $v = 1$ and $v = 2$ levels. The enhancement is driven by increases in N(^{2}D) densities, produced as a consequence of N_2 dissociation by the flare. The increase in population of the v>1 levels also results in an

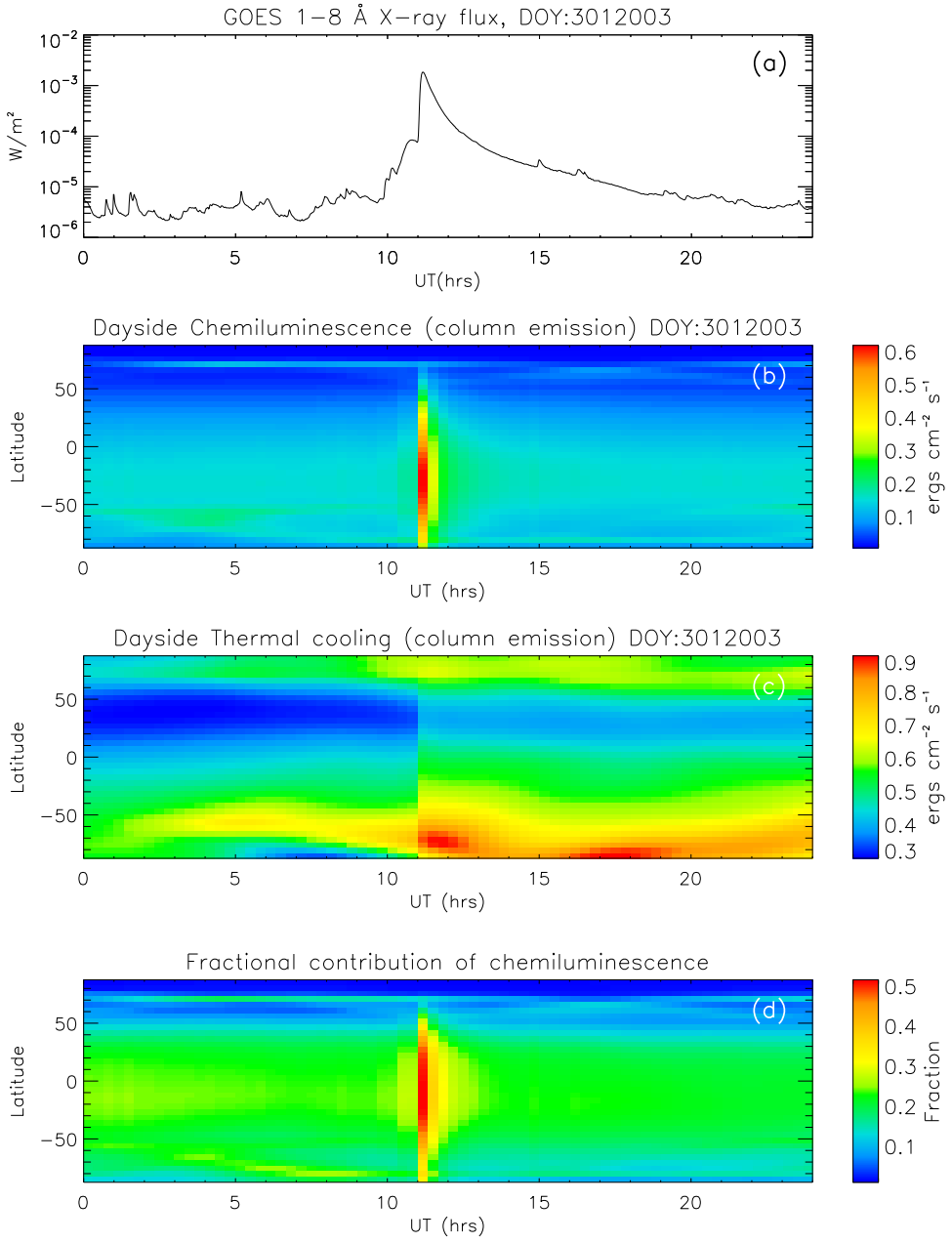

Figure 2.14: (a) 1-8 Å solar flux data from GOES satellite for October 28th 2003. (b) Dayside, Column integrated, zonally averaged emissions dayside chemiluminescence and (c) themal NO-O collisions. (d) Fractional contribution of chemiluminescence to the total energy loss rate from the thermosphere due to NO.

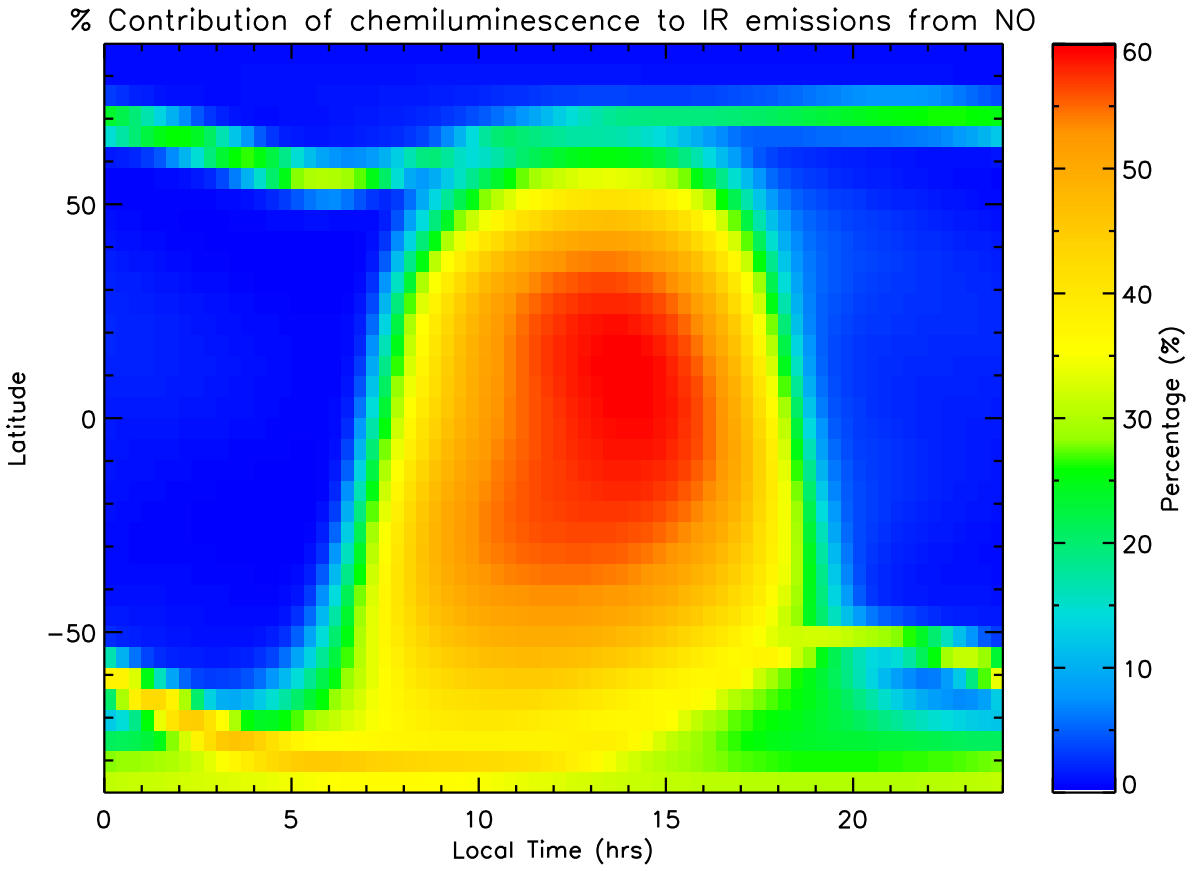

Figure 2.15: Fractional contribution of chemiluminescence to total emission from NO at 11:15 UT (flare peak) for October 28th, 2003.

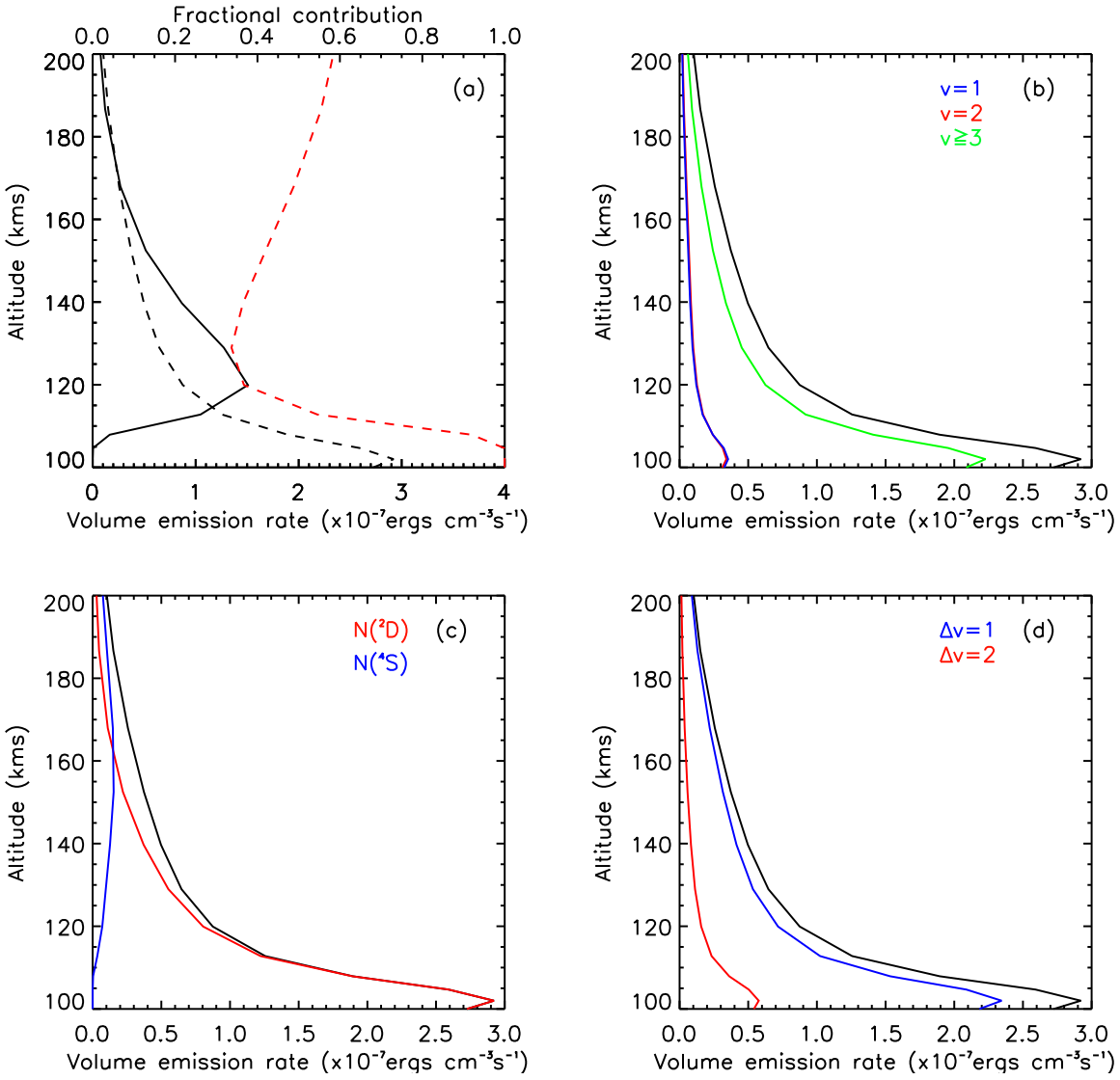

Figure 2.16: (Top-bottom) (a) Comparison of the NO IR emissions due to thermal collisions (solid black) and chemiluminescence (dashed black) at the X-class flare peak on October 28th, 2003. Also shown is the fractional contribution of chemiluminescence (dashed red); The net chemiluminescent emission produced (black) compared to (b) emissions from $v = 1$ (dark blue), $v = 2$ (red) and $v \geq 3$ (green); (c) emission produced by N(^{2}D) (red) and N(^{4}S) (blue) and (d) emissions due to the $\Delta\ v = 1$, 5.3 µm transitions (blue) and the $\Delta\ v = 2$, 2.7 µm transitions (red). The plots correspond to equator, 0° longitude at 11:15 UT.

increase in the 2.7 µm emission which has a peak value of 5.7×10^{-8} ergs cm $^{-3}$ s^{-1}, but its contribution to the emission remains at approximately 20% of the energy loss below 110 km.

2.5.2 2003 "Halloween" storms

The model was also run to study the effect of two geomagnetic storms that were triggered as a result of coronal mass ejections from the Sun arriving on October 29th and 30th (day of year 302 and 303) 2003. Figure 2.17 shows GOES X-ray fluxes and the B_z component of the interplanetary magnetic field (IMF) from the ACE satellite for the period, along with the modeled zonally averaged dayside nitric oxide densities. Coupling between the the solar wind and the Earth's magnetosphere (and consequently the thermosphere) is facilitated when $B_z < 0$ (southward IMF) which are followed by periods of thermospheric recovery when B_z is positive. The effect of this coupling and deposition of the storm energy is seen in the response of NO densities at 110 km and 150 km on the dayside (Fig. 2.17) and nightside (Fig. 2.18). An asymmetrical density response is seen between the two hemispheres at 150 km due to underlying differences in the temperature structure, caused by seasonal effects (Fig. 2.19). Neutral temperatures at 150 km are greater in the southern hemisphere during this period, resulting in increased production of NO from N(^{4}S), while at 110 km the temperature differences are smaller resulting in similar density enhancements. It is seen that the increase in the NO densities persist in the thermosphere after the first storm event on October 29th (day 302), and as a result the largest density is seen following the storm event on October 30th (day 303). At auroral latitudes, the densities are seen to increased by a factor of 2 on average on both the dayside and the nightside.

The effect of the increased NO production rate due to the storms is consequently seen in the zonally averaged chemiluminescent emission (Fig. 2.20), particularly on the nightside at 110 km where most of the storm energy is deposited. The enhancement in NO production is spatially and temoporally restricted to auroral latitudes during the period when the IMF B_z is southward, and returns to quiescent levels during periods of recovery on day 303 and day 304. In contrast, enhancements in the cooling due to thermal processes follow NO densities, beginning at high latitudes and extending to lower latitudes as a result of transport and associated heating processes (Barth et al., 2009). Similar to the case of the X-class flare presented in the previous section, enhancements in the thermal cooling persist well beyond the periods of storm energy deposition. Figures 2.21 and 2.22 show the column emission rate due to chemiluminescence and thermal collisions for the dayside and the nightside, along with the fractional contribution of chemiluminescence. The peak contribution of chemiluminescence occurs on the nightside during the storm, and is approximately 45% of the total energy loss due to emissions from nitric oxide. The fractional contribution of this process to the total emission reduces at low latitudes between days 303 and 306 due to the overall increase in NO densities and hence cooling due to collisional excitation, and returns to quiescent levels on day 306.

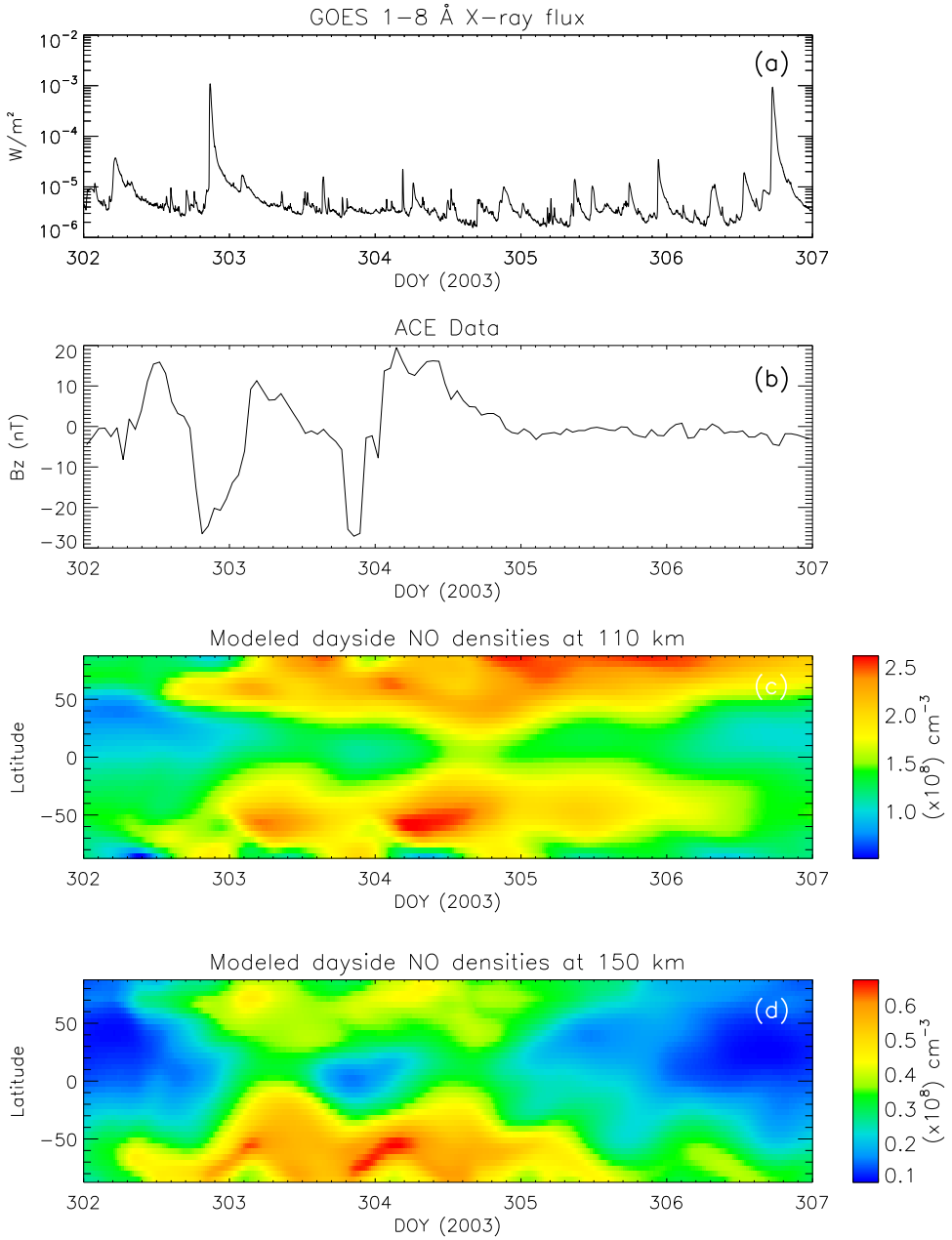

Figure 2.17: (Top-bottom) (a) 1-8 Å solar flux data from GOES satellite for Oct 29th November 2nd (day of year 302-306) 2003; (b) B_z component of solar wind data from ACE satellite for the same period; (c) Zonally averaged modeled dayside NO densities at 110 km and (d) at 150 km.

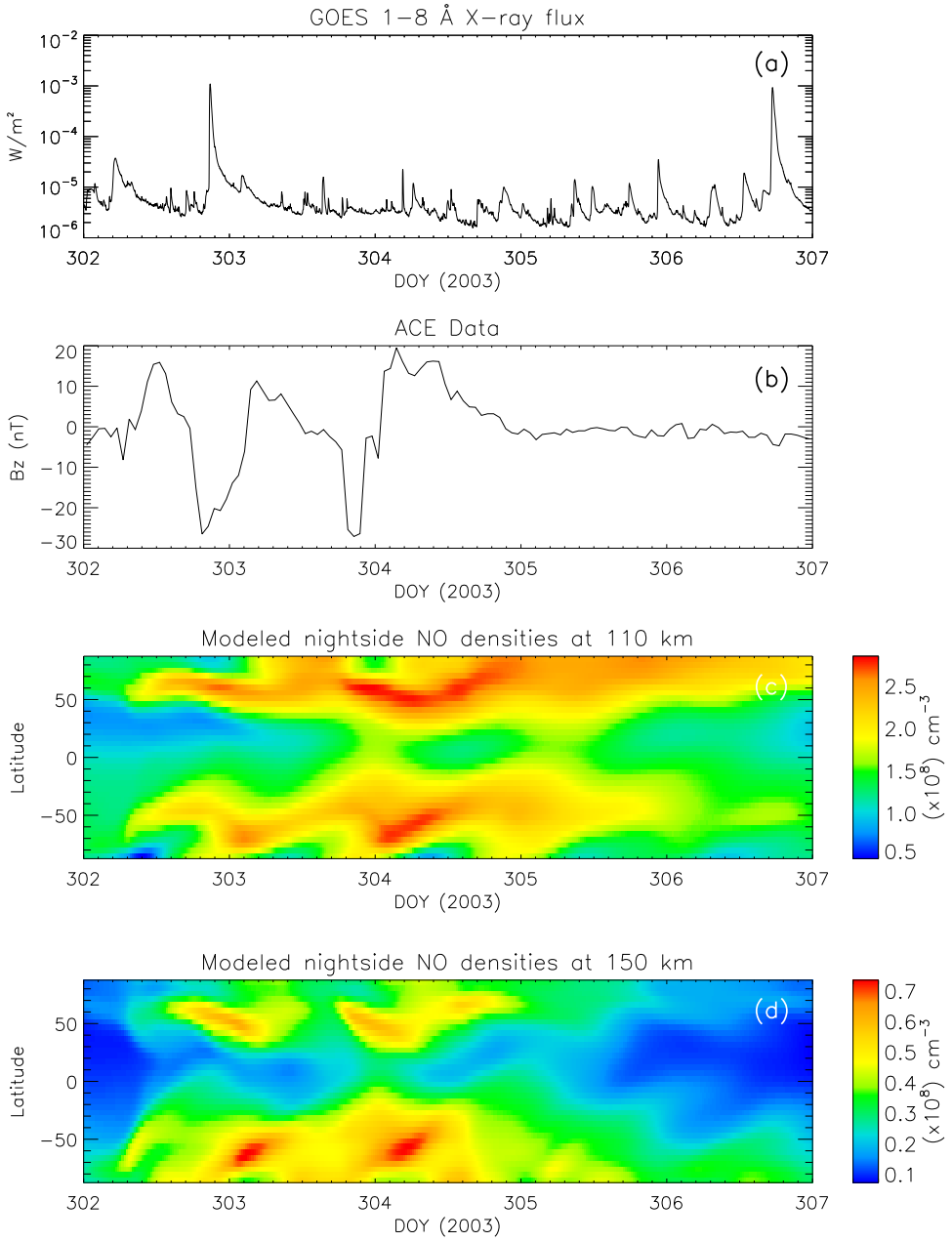

Figure 2.18: (Top-bottom) (a) 1-8 Å solar flux data from GOES satellite for Oct 29th - November 2nd 2003 (b) B_z component of solar wind data from ACE satellite for the same period; (c) Zonally averaged modeled nightside NO densities at 110 km and (d) at 150 km.

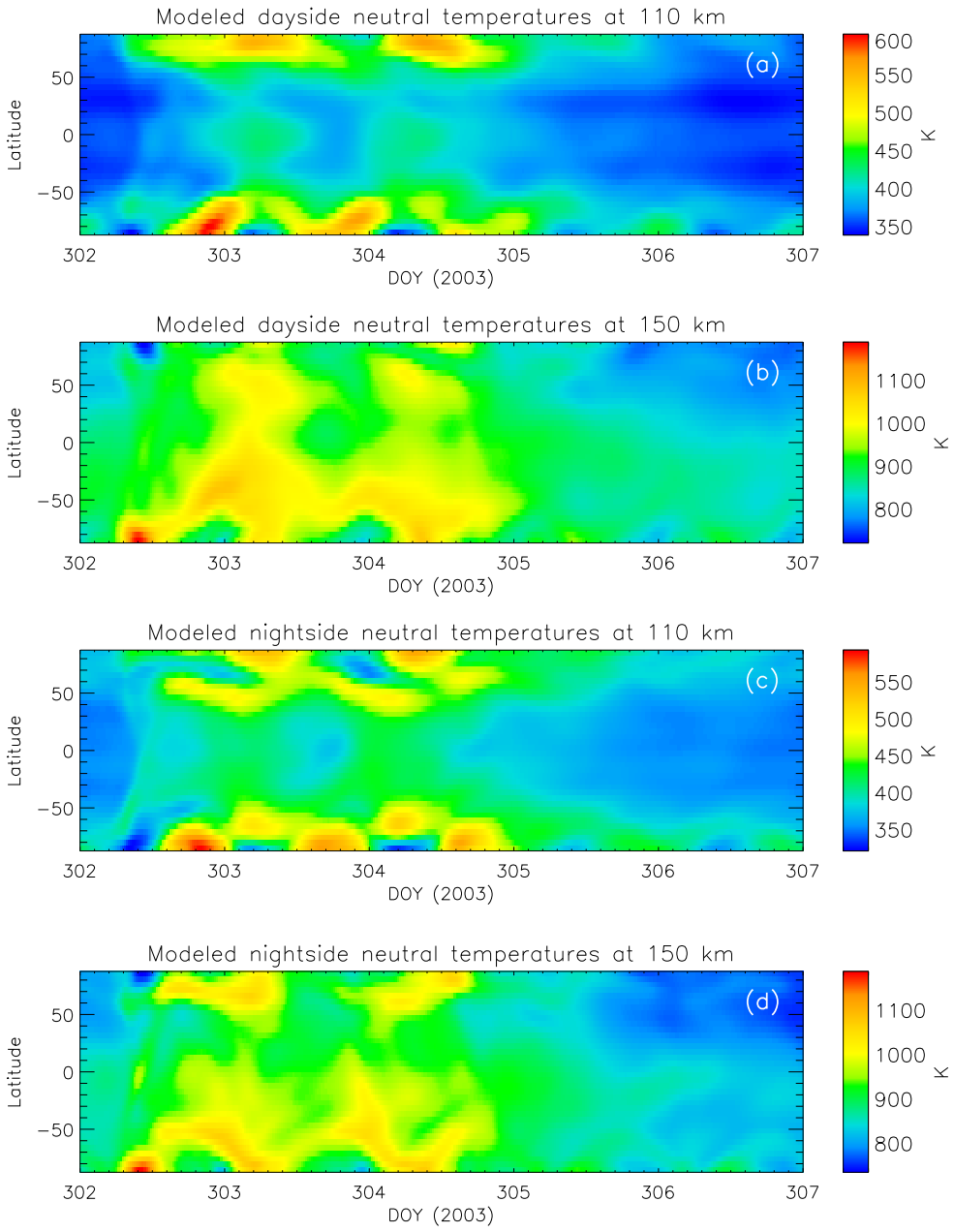

Figure 2.19: Modeled thermospheric neutral temperatures for Oct 29th - November 2nd 2003 on the dayside and nightside, at 110 km and 150 km.

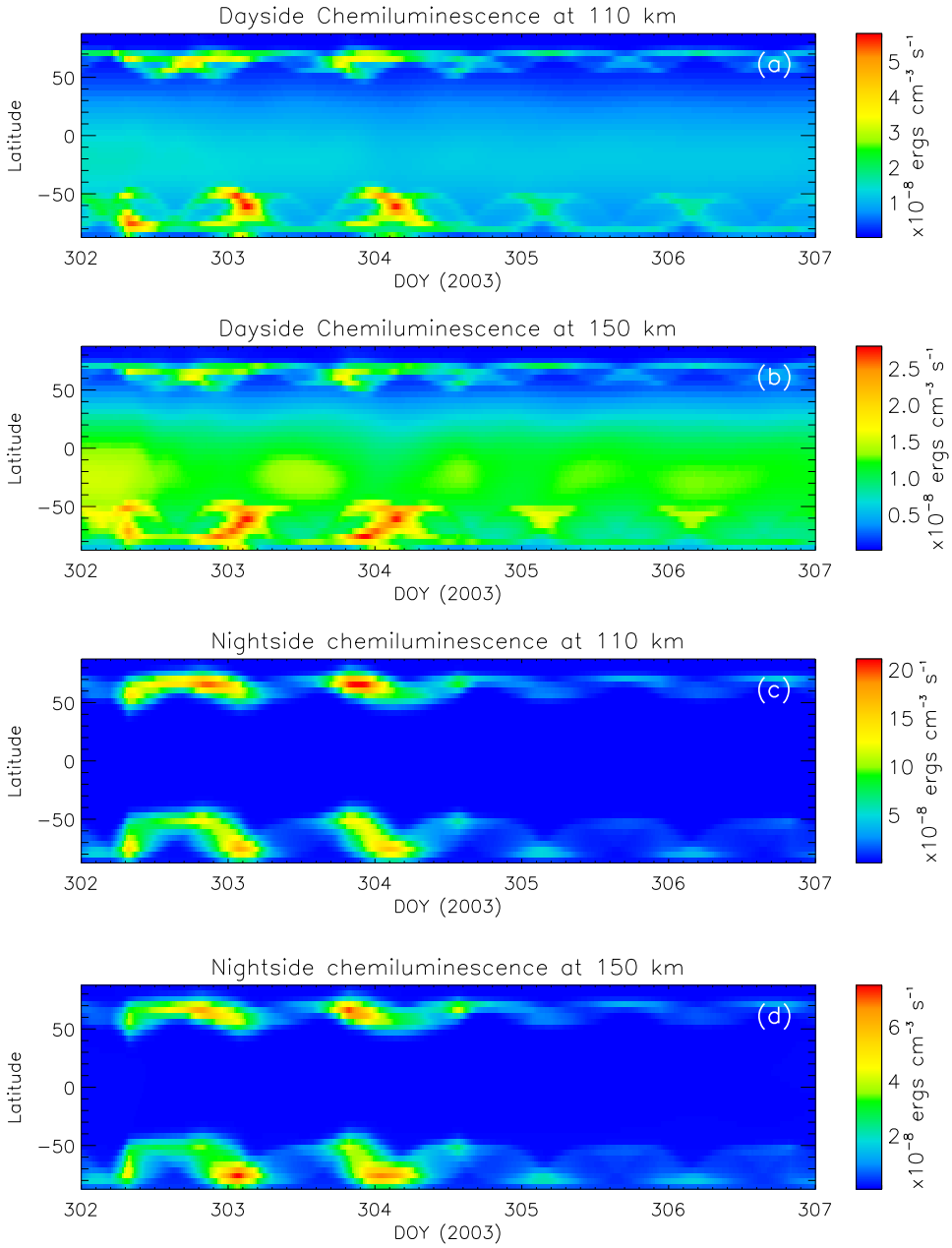

Figure 2.20: Volume emission rate of the chemiluminescent emissions from NO during day Oct 29th - November 2nd 2003. (Top-bottom) (a) On the dayside at 110 km and (b) 150 km; (c) On the nightside at 110 km and (d) 150 km.

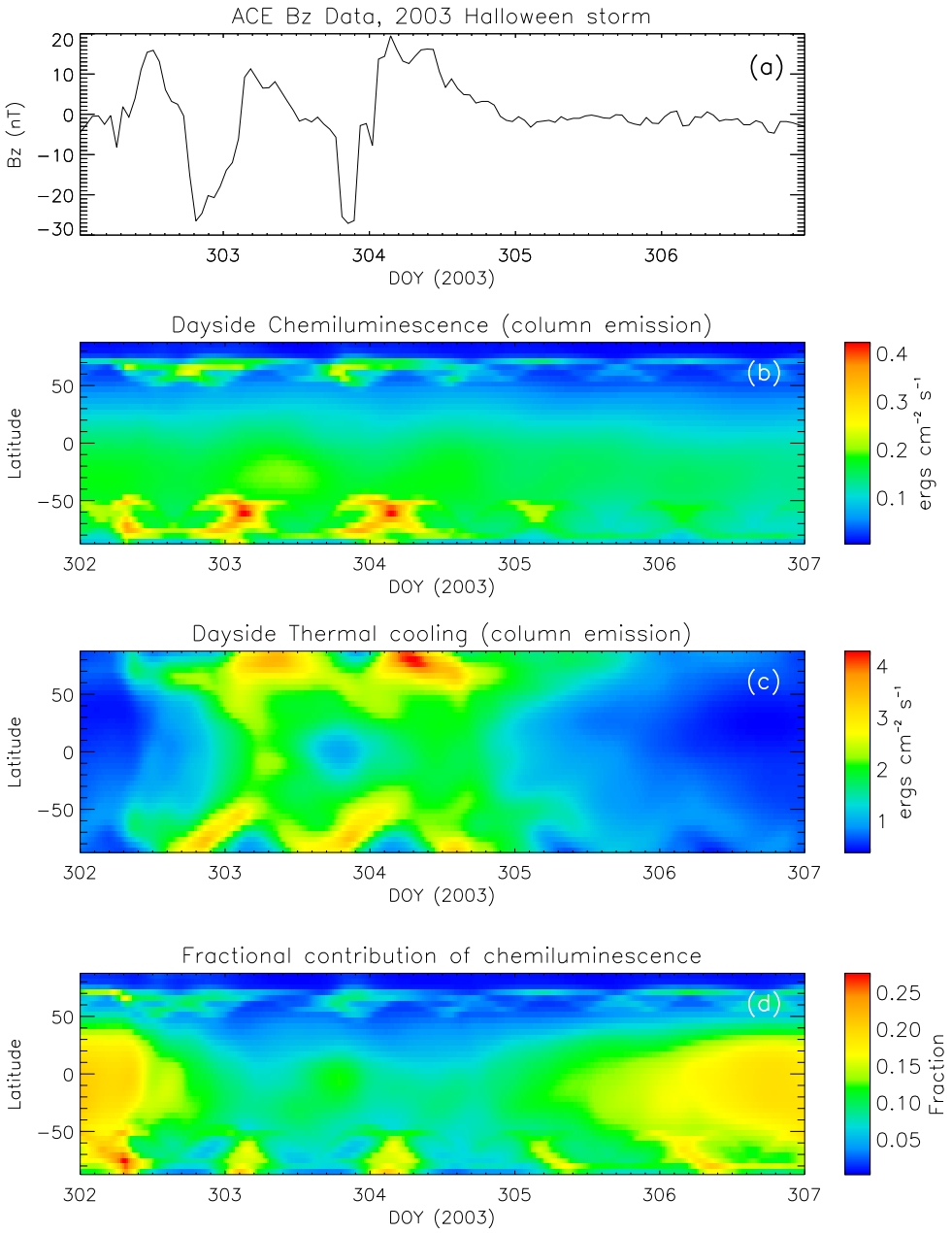

Figure 2.21: (Top-bottom) (a) B_z component of solar wind data from ACE satellite for Oct 29th - November 2nd 2003; (b) Dayside column emission rate due to chemiluminescence and (c) due to collisional excitation; (d) Fractional contribution of chemiluminescence to the total energy loss due to NO on the dayside.

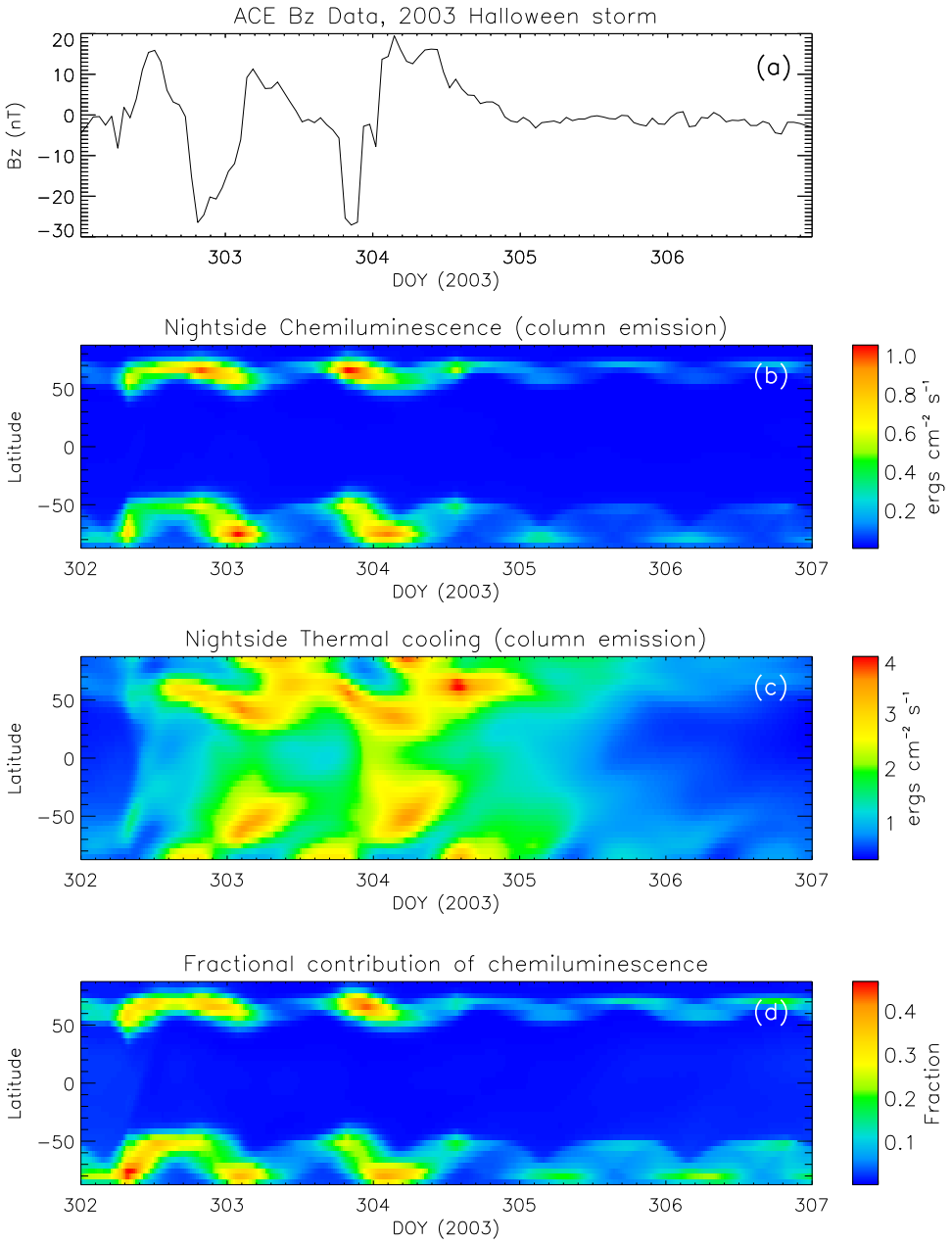

Figure 2.22: (Top-bottom) (a) B_z component of solar wind data from ACE satellite for Oct 29th - November 2nd 2003; (b) Nightside column emission rate due to chemiluminescence and (c) due to collisional excitation; (d) Fractional contribution of chemiluminescence to the total energy loss due to NO on the nightside.

2.5.3 Recovery of thermospheric densities following geomagnetic storms

Studies regarding the response of the thermosphere to geomagnetic storms have noted significant discrepancies between the modeled and observed neutral densities, particularly during the recovery period following the storms (Lei et al., 2011; Lu et al., 2014; Sheng et al., 2017). Energy deposition by the storm results in an increase in the thermospheric temperature and neutral density in the upper atmosphere, followed by a return to equilibrium when the storm energy has been dissipated away. As has been shown in the previous sections, nitric oxide densities and emissions play a crucial role during the recovery of the thermosphere.

The parameter of interest in these studies has typically been the relaxation time τ of neutral densities or temperature, which is defined as the amount of time taken for either quantity to reduce to $1/e$ of a reference value, typically the value observed at the start of the recovery phase following the storm. Numerical simulations have been shown to overestimate the relaxation times by a factor of 1.5 - 2 when compared to observations, and while some of the deficiencies in reproducing the thermospheric response has been attributed to inadequate specification of geomagnetic indices and energy inputs used to drive the model, there is also a need to re-examine the nitric oxide chemistry and associated energetics in models due to its importance during periods of enhanced energy deposition. The effect of introducing the additional emission from NO on thermospheric recovery is examined here.

The October 2003 storms show two distinct disturbed periods on day 302 and 303 when B_z was southward and energy deposition occurred; the period following these events when B_z is northward is referred to as the recovery period. Changes to the TIE-GCM model discussed in section 2.2 were implemented over three model runs (referred to as R1-R3 in the text) listed in Table 2.3. Model results of thermospheric neutral densities at 400 km are shown in Figure 2.23, normalized to the modeled peak density between days 302 and 306 for each case. The neutral density relaxation time calculated for the recovery period on day 303 is referred to as T1, while that on day 304 is referred to as T2. In each case, τ is obtained by calculating the average rate of density change during the recovery period, and then calculating the time taken for the densities to reduce to $1/e$ of the peak value at the beginning of each recovery period.

Table 2.3: Model run descriptions for the 2003 October geomagnetic storms

Run 1	Original TIE-GCM code
Run 2	"Unscaled" O(^{3}P) cooling,
	Reducing NO thermal cooling by a factor of 2,
	Temperature dependent rate for Eq. 2.10
Run 3	Run 2 changes + chemiluminescence

For the reference TIE-GCM run R1, the calculated relaxation times for the two recovery periods on the dayside were 27 hours and 35.5 hours respectively, and the values on the nightside were 19 hours and 27.7 hours respectively. Previous modeling results (Lei et al., 2011) have noted the inability of the model densities to fully return to pre-storm levels during R1 before the onset of the second storm, and this feature is seen to persist in the present model runs. For the second model run R2, the NO cooling rate was reduced by a factor of 2 following the results of Caridade et al. (2008), while that due to O(^{3}P) was increased by a factor of 2 following Grossmann and Vollmann (1997). The run also used the temperature dependent reaction rate for the production of NO from N(^{2}D), as recommended by Duff et al. (2003). It is seen that the net effect of these changes was an average increase of 50% in the relaxation time following both storms on the dayside and the nightside. Finally, the model run R3 incorporates the chemiluminescent energy loss due to NO production in addition to the changes made in R2. Marginal changes are seen in the recovery time as compared to R2, except for the nightside recovery period T1 which reduces by 18% between R2 and R3. However, it is noted that these changes do not account for the increase in relaxation times introduced by the reduction in the NO collisional cooling rate.

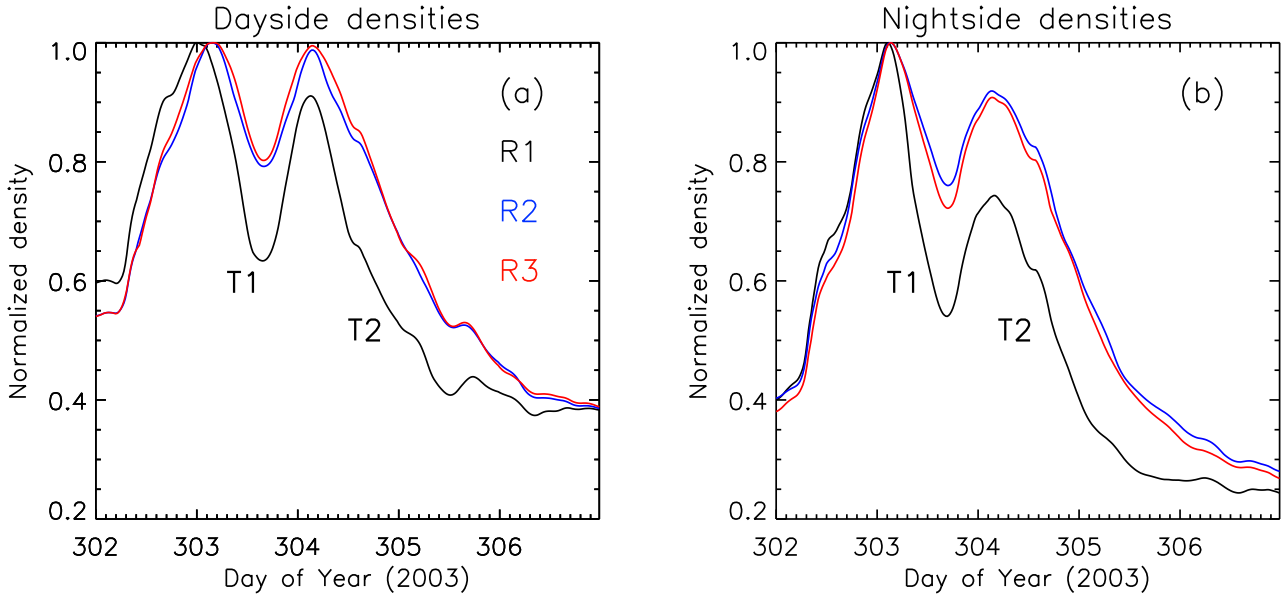

Figure 2.23: Modeled response of thermospheric neutral densities at 400 km, normalized to peak density over the period of the geomagnetic storm for the model runs R1-R3. Responses are shown separately for the (a) dayside (LT 1200 hrs) and (b) nightside (LT 0000 hrs). T1 and T2 indicate the recovery periods for which the relaxation times are calculated. Differences between the model runs are detailed in the text.

Table 2.4: Relaxation times in hours (T1/T2) obtained from TIE-GCM runs

	Run 1	Run 2	Run 3
Dayside τ	27/35.5	37.5/51.2	38.4/50.9
Nightside τ	19.3/27.7	37/37.7	30.3/37.2

2.6 Conclusions

Building upon the work of Sharma et al. (1998) and Funke and López-Puertas (2000), an additional source of infrared emission from nitric oxide at 5.3 and 2.7 µm has been modeled by calculating the level populations of NO(v≤10). These emissions are concurrent with the production of NO in the thermosphere, and serve to significantly reduce the exothermicity of the reactions of N(^{4}S) and N(^{2}D) with O_2. Our present model uses up-to-date results regarding the nascent vibrational distribution of NO produced in the thermosphere, relevant reaction rates, and assumed product channels to calculate the emission. We estimate the additional emission to contribute between 25-40% of the total energy removed from the dayside thermosphere by NO, and expect this value to increase slightly after accounting for other minor sources of vibrationally excited NO (N_2(A), N(^{2}P) and N^+) that are not presently considered. Strictly speaking, this emission is not a cooling process as it serves to remove energy deposited by solar irradiance before it becomes part of the thermal energy budget. However, the reduction in energy available to heat the thermosphere reduces modeled exospheric temperatures by 2-3%. A parameterization scheme that calculates the emission without the need to compute the vibrational level populations is also presented, and is shown to reproduce the full calculation to within 5% at all latitudes under quiescent solar conditions.

The emission is modeled for periods of enhanced solar energy deposition, namely, for an X-class solar flare and geomagnetic storms that occurred during October-November 2003. In both cases, the peak contribution of the emission was seen to be equivalent, if not greater, than that produced via collisional excitation of NO. However, increases in this emission is constrained to periods of increased NO production, while enhancements in NO density persist over longer timescales in the thermosphere and have a greater overall cooling effect on the thermosphere. It is shown that while chemiluminescence improves the post-storm thermospheric recovery time of neutral densities to a small extent, it alone cannot resolve the existing model-data discrepancy. This suggests the need to re-examine the underlying physics and chemistry of current thermospheric models in order to identify processes that need to be improved upon.

Chapter 3

The Atmospheric Chemistry and Energetics (ACE) 1D model

3.1 Motivation

Numerical modeling has been an invaluable tool that has been used to further our understanding of processes occurring in the upper atmosphere. Of particular note is the development and use of global thermospheric ionospheric models such as the Thermospheric-Ionospheric General Circulation Model (TIE-GCM) (Qian et al., 2014) and Global Ionospheric Thermospheric Model (GITM) (Ridley et al., 2006), which has been enabled by relatively easy access to large computational power. While these three dimensional models serve well to reproduce satellite observations and atmospheric phenomena, their complexity also hinders the ability to test new ideas quickly and obtain a first order understanding of changes introduced into the model. This gap in analytical tools is well served by simpler models that reduce the order of the problem by accounting for fewer spatial dimensions. Such models have previously been used to test hypothetical solar spectra, variations in physical proceses and new chemistry schemes (Smithtro and Sojka, 2005; Qian et al., 2006; Roble, 1995; Swaminathan et al., 2001). In this vein we develop a new one dimensional model that incorporates up-to-date aeronomic results including those presented in the previous chapter to compute a globally averaged thermosphere.

3.2 Description

The Atmospheric Chemistry and Energetics (ACE) 1D model self-consistently solves the continuity and energy equations in order to obtain an average one dimensional representation of the global thermosphere in terms of densities of various neutral and ionic species, along

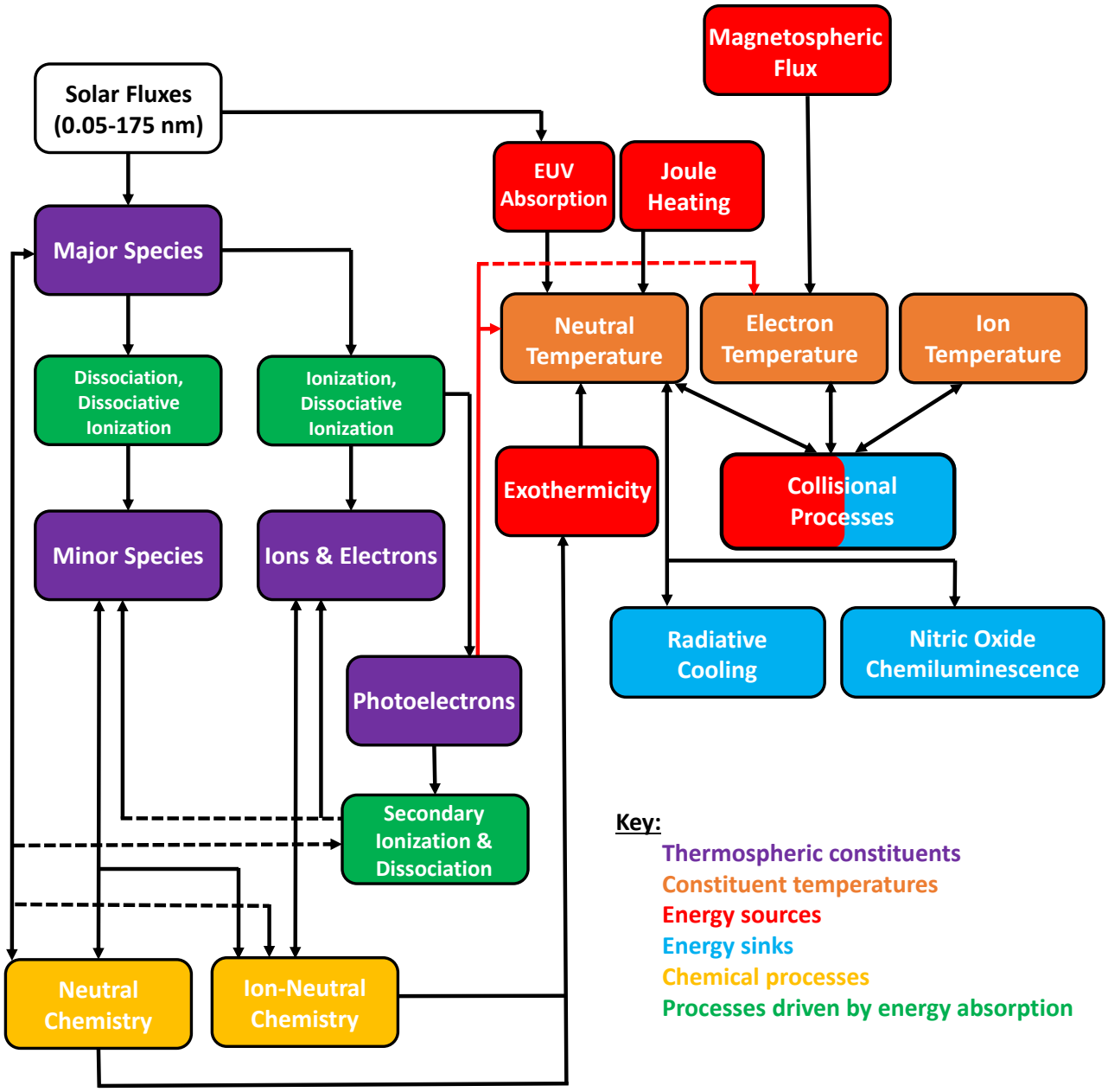

Figure 3.1: Block diagram of the ACE1D model. The model produces a global average representation of the thermosphere and ionosphere by solving for the densities of major and minor neutral species, ion and electron densities, and the neutral, ion and electron temperatures. The primary input to the model is solar fluxes between 0.05-175 nm, with fixed values specified for energy input from the magnetosphere and joule heating. Neutral-neutral and ion-neutral chemistry couple the major, minor and ionic species, while collisional processes couple energy exchange between the neutral thermosphere and the ionosphere.

Table 3.1: ACE model parameters

Major Species	N_2, O_2, O
Minor Species	$N(^2D)$, $N(^4S)$, $N(^2P)$, NO, $N_2(A)$, $O(^1D)$
Ions	$O^+(^4S)$, $O^+(^2D)$, $O^+(^2P)$, N^+ NO^+, N_2^+, O_2^+
Vertical grid	$Z = -\ln(p/P_0)$, Z=-7 to 7 ΔZ=0.25, z_{lb}=97 km
Neutral Temperature (T_n)	LBC: 177 K, UBC: $\frac{\partial T_n}{\partial Z} = 0$
Electron/Ion Temperatures (T_e, T_i)	LBC: $T_e = T_i = T_n$, UBC: $\lambda \frac{\partial T_e}{\partial Z} = f$
Solar input	Solar Flux (0.05-175 nm) / F10.7
Joule Heating Input	70 GW

with neutral, ion and electron temperatures. The various components of the model and their interconnections are shown in Figure 3.1, and an overview of the model parameters is given in Table 3.1. The model uses a pressure based vertical co-ordinate system, with grid points defined as:

$$Z = -\ln(p/P_0) \tag{3.1}$$

where p is the pressure at the grid point under consideration and P_0 is a reference pressure of 50 µPa. A change of ΔZ=1 in this grid scheme corresponds to a change in altitude by one scale height, or the reduction in pressure by a factor of e. The boundaries of the model are denoted by $Z = \pm 7$, with a resolution of ΔZ=0.25. The lower boundary of the model is fixed at an altitude of 97 km, which corresponds to the approximate location of the mesopause averaged over a solar cycle. The location of the $Z = 7$ pressure level is tied to solar activity and exospheric temperatures, and varies approximately between 450 and 750 km.

3.3 Major species

Following the formulation of Dickinson et al. (1984), the model computes for the mass mixing ratios of the major species, which for a species with mass m_i and density n_i is given as:

$$\Psi_i = \frac{m_i \; n_i}{\sum\limits_j m_j n_j} \tag{3.2}$$

where the summation in the denominator is over the three major species (N_2, O_2 and O) in the ACE model. The O_2 and O densities are coupled in the thermosphere through dissociation and recombination reactions, and we define the vector $\mathbf{\Psi} = [\Psi_{O_2}, \Psi_O]$ in order to solve for their mass mixing ratios using the continuity equation:

$$\frac{\partial \mathbf{\Psi}}{\partial t} = -e^Z \tau^{-1} \frac{\partial}{\partial Z} \left[\frac{\bar{m}}{m_{N_2}} \left(\frac{T_{00}}{T} \right)^{0.25} \boldsymbol{\alpha}^{-1} \mathbf{L} \mathbf{\Psi} \right] + e^Z \frac{\partial}{\partial Z} \left(K_E \, e^{-Z} \left(\frac{\partial}{\partial Z} + \frac{1}{\bar{m}} \frac{\partial \bar{m}}{\partial Z} \right) \mathbf{\Psi} \right) + (\mathbf{S} \text{ - } \mathbf{R}) \tag{3.3}$$

where τ is the diffusion timescale characteristic of the thermosphere, $\bar{m}$ is the mean molecular mass, T_{00} is a reference temperature equal to 273 K, and $\mathbf{S}$ and $\mathbf{R}$ are the coupled production and loss terms for O_2 and O. The above equation relates the time rate of change of the mass mixing ratios of O_2 and O to the gradient of the flux due to molecular and eddy diffusion (first and second terms) and the chemical production and loss of the species (third term).

The matrix $\boldsymbol{\alpha}$ governs diffusion of the major species, with its elements defined as:

$$\begin{aligned} \alpha_{11} &= -[\phi_{13} + (\phi_{12} - \phi_{13})\psi_2] \\ \alpha_{22} &= -[\phi_{23} + (\phi_{21} - \phi_{23})\psi_1] \\ \alpha_{12} &= (\phi_{12} - \phi_{13})\psi_1 \\ \alpha_{21} &= (\phi_{21} - \phi_{23})\psi_2 \end{aligned} \tag{3.4}$$

where the subscripts 1, 2 and 3 refer to O_2, O and N_2 respectively. ϕ_{ij} refers to the mutual diffusion coefficients given as:

$$\phi_{ij} = \frac{D}{D_{ij}} \frac{m_3}{m_j} \tag{3.5}$$

with the characteristic diffusion coefficient D:

$$D = D_0 \frac{P_{00}}{P} \left(\frac{P}{T_{00}} \right)^{1.75} \tag{3.6}$$

D_{ij} are the mutual diffusion coefficient for gases, with the values of D_{12}, D_{13}, D_{23} equal to 0.26, 0.18, 0.26 respectively. D_0 is the characteristic diffusion coefficient at temperature T_{00} (= 273 K) and pressure P_{00} (= 10^5 Pa) and equals 0.2×10^{-4} m^2 s^{-1}. $\mathbf{L}$ is a diagonal matrix operator with the elements

$$L_{ij} = \delta_{ij} \left(\frac{\partial}{\partial Z} - \epsilon_{ii} \right) \tag{3.7}$$

where

$$\epsilon_{ij} = 1 - \frac{m_i}{\bar{m}} - \frac{1}{\bar{m}} \frac{\partial \bar{m}}{\partial z} \tag{3.8}$$

The eddy diffusion coefficient K_E is a prescribed parameter that is used to approximate turbulent mixing processes in the lower thermosphere and improve agreement between models

and observational data. While K_E does not have a definitive formulation, previous models have generally specified an altitude dependent value (Dickinson et al., 1984; Roble et al., 1987; Smithtro and Sojka, 2005), supplemented using harmonic functions to include seasonal effects (Qian et al., 2009). We use the expression given by Roble et al. (1987):

$$K_E(Z) = 5 \times 10^{-6} \exp(-7 - Z) \text{ s}^{-1} \tag{3.9}$$

This expression is converted to dimensional units by multiplying it by the scale height squared, and has a value of approximately 150 m^2 s^{-1} at the lower boundary.

The list of chemical reactions that form the source terms **S** and **R** in Eq. 3.3 have been given in Appendix A along with their rate coefficients. These terms account for coupled processes that serve as a source for one species but as a sink for the other (e.g., photodissociation of O_2), as well for other reactions that form explicit source/sink terms.

While the thermospheric models of Roble et al. (1987) and Smithtro and Sojka (2005) have specified number densities of the major species at the lower boundary, analysis of data from the MSIS empirical model (Picone et al., 2002) suggests that the O/O_2 ratio at 97 km is not a constant. Rather, it increases with solar activity due to greater dissociation of O_2 into O. As a result we constrain Eq. 3.3 at the lower boundary by specifying ψ_O and ψ_{O_2} values obtained from MSIS. At the upper boundary we assume diffusive equilibrium and use the condition $\mathbf{L\Psi} = 0$.

The model solves for the vector $\mathbf{\Psi}$ at each time step, and obtains the mass mixing ratio for N_2 using the relation:

$$\Psi_{N_2} = 1 - \Psi_{O_2} - \Psi_O \tag{3.10}$$

3.4 Minor species

For netural minor species, the model calculates the densities of odd nitrogen species - NO, $N(^4S)$, $N(^2D)$, $N(^2P)$, the first excited state of molecular nitrogen, $N_2(A)$, and excited atomic oxygen, $O(^1D)$. The densities of many of these species are considered to be in steady state ($\partial n_i/\partial t = 0$) or photochemical equilibrium (PCE), in which case the densities can be calculated as the ratio of their net production rate and loss frequency:

$$n_i = \frac{P_i}{L_i} \tag{3.11}$$

However, it is necessary to consider diffusion effects to accurately model densities of NO and $N(^4S)$ due to their comparatively long lifetimes ($\approx 10^3$ seconds for NO, 10^4 seconds for $N(^4S)$ at 200 km) in the thermosphere. The model solves for the mass mixing ratios of these

two species using a form of the continuity equation similar to Eq. 3.3 (Roble, 1995):

$$\frac{\partial \psi_i}{\partial t} = -e^Z \frac{\partial}{\partial Z} A_m \left[\frac{\partial}{\partial Z} - E_i \right] \psi_i + e^Z \frac{\partial}{\partial Z} e^{-Z} K_E(Z) \left[\frac{\partial}{\partial Z} + \frac{1}{\bar{m}} \frac{\partial \bar{m}}{\partial Z} \right] + (S_i - R_i) \quad (3.12)$$

where

$$E_i = \left[1 - \frac{m_m}{\bar{m}} - \frac{1}{\bar{m}} \frac{\partial \bar{m}}{\partial Z} \right] - \alpha_i \frac{1}{T} \frac{\partial T}{\partial Z} + \bar{F} \psi_i \quad (3.13)$$

where the first two terms once again describe the gradient of the flux due to molecular and eddy diffusion processes, and the third term refers to chemical sources and sinks. α_i denotes the thermal diffusion coefficient, and $\bar{F}$ denotes a matrix operator which accounts for the frictional interaction between the minor species and the background atmosphere. Following the work of Colegrove et al. (1966), the thermal diffusion coefficient is set to zero for NO and N(^{4}S). We assume diffusive equilibrium at the upper boundary for both species, while at the lower boundary we specify a downward flux for NO and photochemical equilibrium for N(^{4}S).

Production of N_2(A) in the thermosphere has been shown to play a significant role in nitric oxide chemistry (Yonker, 2013) by directly and indirectly influencing the production rates of NO and N(^{2}D). Its densities are calculated by considering vibrational level specific production rates, obtained by scaling the photoelectron ionization rate of N_2, and considering losses to atomic oxygen and radiative relaxation in the Vegard-Kaplan bands. O(^{1}D) is assumed to be produced via photodissociation of O_2 (Lee et al., 1977) and recombination of O_2^+ (Schunk and Nagy, 2009), and is lost to quenching by the neutral background atmosphere and via radiative relaxation at 630 nm. CO_2 is included as a chemically inert constituent in the model as it is an important source of radiative cooling in the lower thermosphere, with a value of $\psi_{CO_2} = 3.5 \times 10^{-4}$ specified at the lower boundary.

3.5 Ionospheric densities

The ACE model calculates production of ionospheric species by accounting for direct photoionization and dissociative ionization of neutral species, ionization due to energetic photoelectrons, and charge exchange processes. Charge exchange processes also serve as the dominant loss mechanism for ions, except for NO^+ which forms the terminal ion in these reactions. NO^+ is lost only via dissociative recombination, which results in the production of N(^{4}S) and N(^{2}D) and is an important component of the NO chemistry (Swaminathan et al., 2001). The list of ionospheric reactions implemented in the model is given in Appendix A.

Densities of ionospheric species are calculated assuming photochemical equilibrium, except for O^+(^{4}S) and N^+ which are assumed to undergo diffusion. The continuity equation in this case takes the form:

$$\frac{\partial n_i}{\partial t} = (S_i - R_i\, n_i) - \frac{\partial \phi_i}{\partial Z} \quad (3.14)$$

Where S_i and R_i are the net production rate and loss frequency respectively. The flux term ϕ_i is expressed as:

$$\phi_i = -sin^2 I \, D_a \left(\frac{\partial n_i}{\partial Z} \frac{n_i}{H_p} + \frac{n_i}{T_p} \frac{\partial T_p}{\partial Z} \right) \tag{3.15}$$

Where D_a is the ambipolar diffusion coefficient, and H_p and T_p are the plasma scale height and temperature respectively. Ion densities are well represented by photochemical equilibrium at altitudes where eddy diffusion is important and is not included in the above equation. The magnetic dip angle I denotes the orientation of the local magnetic field with the horizontal, and dictates the effectiveness of the field aligned diffusion in the vertical direction. A value of 0° corresponds to the direction of the field near the magnetic equator, where the field is parallel to the ground and there is no diffusion in the vertical direction. Similarly, 90° corresponds to the condition at the magnetic poles. The magnetic dip angle does not have a well defined value in the context of a global average thermospheric model (Smithtro, 2004), and we presently use a value of 75° to account for the deviation from a perfectly vertical magnetic field. The model assumes net charge neutrality and calculates the electron density to be equal to the sum of the ion densities.

3.6 Photoelectrons

The electrons produced as a result of ionization of neutral species in the thermosphere by solar EUV radiation and soft X-rays are termed as 'photoelectrons'. It is possible for the incident radiation to be more energetic than the ionization potential of the absorbing species, in which case the additional energy is carried away by the photoelectron produced. These energetic photoelectrons may in turn continue to ionize, dissociate, excite and impart energy to other atoms and molecules until their excess energy is spent.

As the production of photoelectrons are tied to a portion of the solar spectrum that varies significantly over various time scales, accurately accounting for their presence is an important aspect of modeling the thermosphere. Previous atmospheric models have included photoelectrons in their calculations by various means, such as by applying a scaling factor to the total photoionization rate (Roble et al., 1987), parameterizing the photoelectron cascade calculations to approximate fluxes (Richards and Torr, 1983; Smithtro and Sojka, 2005), and obtaining a full numerical solution for the fluxes by solving electron transport equations (Bailey et al., 2002).

A more recent approach that has been implemented in global thermospheric-ionospheric models involves multiplying the wavelength dependent photoionzation rate by appropriate scaling factors (Solomon and Qian, 2005) to account for the secondary ionizations, dissociative ionizations and dissociations caused by photoelectrons. This method avoids the need to calculate photoelectron fluxes themselves and reduces computational complexity, and has

also been shown to agree well with the full numerical solution obtained from the GLOW model of Solomon et al. (1988). The ACE model uses this parameterization scheme to account for photoelectron effects in the thermosphere.

Collisions with photoelectrons also serve as the primary heat source for ambient ionospheric electrons, and thus have to be accounted for in electron temperature calculations. A parameterization for the volume heating rate of electrons due to photoelectrons between 120 - 325 km was initially given by Swartz and Nisbet (1972), where the heating rate was expressed as the product of a heating efficiency factor and the local photoionization rate. The heating efficiency factor in turn was expressed as a polynomial fit to a deposition parameter, a measure of the relative concentration of electrons to the neutral background atmosphere. An improved polynomial fit was subsequently given by Smithtro and Solomon (2008) that accurately reproduced the heating rate between 100 - 750 km. A further improvement of the parameterization was also given by Smithtro and Solomon (2008), where the photoelectron heating rates were calculated using separate fits for two broad band bins between 0-55 nm and 55-105 nm, which were defined on the basis of overall heating efficiency and variability under active solar conditions. This parameterization scheme has been shown to reproduce the electron heating rates for nominal and solar flare conditions within 15% of those calculated using the GLOW model, provided that the solar flux below 5 nm is well specified. The ACE model fits this requirement (section 3.7), and implements the above method to calculate the photoelectron heating rate of the ambient ionospheric electrons. Expressions for the heating efficiency factor, the deposition parameter and the polynomial fit coefficients used to calculate the heating rates are given in Appendix B.

3.7 Solar Fluxes

Energy input into the model is specified primarily as solar fluxes between 0.05 - 175 nm, which covers the soft x-rays, extreme ultraviolet and far ultraviolet (XUV, EUV, FUV) regions of the solar spectrum. The model uses the 22 wavelength bin structure proposed by Solomon and Qian (2005) which was designed to efficiently reproduce calculations obtained from high spectral resolution solar fluxes. Reference spectra for this model was obtained from the following sources - GOES data (0.05 - 0.8 nm), satellite and sounding rocket measurements (0.8 - 1.8 nm), a scaled version of the HFG model (Hinteregger et al., 1981) (1.8 - 5 nm) and the EUVAC model (5 - 105 nm). A separate bin is used to specify the Lyman-alpha flux, and multiple overlapping bins are used between 65 - 97.5 nm in order to account for the significant band structure that occurs in the absorption cross-sections of the major species at those wavelengths. An additional fifteen 5 nm wide bins are used to specify the fluxes between 105 - 175 nm following the work of Woods and Rottman (2002).

Given the reference solar spectrum obtained from the above mentioned sources, the spectrum for a given level of solar activity is calculated by scaling the photon fluxes in individual

wavelength bins, following the method used in the EUVAC model (Richards et al., 1994):

$$F(\lambda) = F_{ref}(\lambda)[1 + A(\lambda)(P - 80)] \tag{3.16}$$

where λ is the wavelength, F_{ref} refers to the refence solar minimum spectra and A is a wavelength dependent scaling factor. P is a proxy for solar activity, defined as:

$$P = (F10.7_d + F10.7_a)/2 \tag{3.17}$$

where $F10.7_d$ and $F10.7_a$ are the daily and centered 81 day average of the 10.7 cm solar flux index. The model is designed to reproduce the reference solar spectra for $P = 80$, and the fluxes are scaled to 80% of their reference value at all wavelengths for $P < 80$. Values for the wavelength intervals are given along with the reference solar spectra and scaling factors in Appendix C.

3.7.1 Globally averaged inputs

To compute a globally averaged thermosphere and account for the fact that only one hemisphere is sunlit at any given time, the solar irradiance input to the model is scaled by a factor of 1/2 across all wavelengths. Further, it is necessary to specify an average value for the solar zenith angle to account for the local time variation on the sunlit side. Using the expression for solar zenith angle (Jacobson, 2005):

$$\cos\theta_s = \sin\phi\sin\delta + \cos\phi\cos\delta\cos H_a \tag{3.18}$$

θ_s, ϕ, δ and H_a refer to the solar zenith angle, latitude, solar declination angle and local hour angle of the Sun, respectively. Then, the area weighted average of the cosine of the solar zenith angle for the sunlit half of the Earth is evaluated as:

$$< \cos\theta_s >= \frac{1}{2\pi r^2}\int_{-\frac{\pi}{2}}^{\frac{\pi}{2}}\int_{-\frac{\pi}{2}}^{\frac{\pi}{2}} r^2\,\cos^2\phi\cos H_a\,d\phi\,dH_a \tag{3.19}$$

where we take advantage of the spherical symmetry and simplify the expression to integrate about the subsolar point ($\delta = 0$). Here r refers to the Earth's radius, and we integrate between $-\pi/2$ and $\pi/2$ for the local solar angle ($H_a = 0$ refers to local noon). Evaluating this expression yields a value of $\theta_s = 60°$.

3.8 Neutral Temperatures

Neutral temperatures are solved for in the model using the one-dimensional time-dependent heat equation which accounts for molecular diffusion, eddy diffusion, and neutral heating and cooling processes:

$$\frac{\partial T}{\partial t} = \frac{g\ e^Z}{P_0\ C_p}\frac{\partial}{\partial Z}\left(\frac{K_T}{H}\frac{\partial T}{\partial Z} + K_E H^2 C_p \rho\left(\frac{g}{C_p} + \frac{1}{H}\frac{\partial T}{\partial Z}\right)\right) + \frac{(Q - L)}{C_p} \tag{3.20}$$

Here, T is the neutral gas temperature, C_p is the specific heat per unit mass, H refers to the scale height, K_T and K_E are the thermal and eddy diffusion coefficients and ρ is the average mass density. Q and L are the heat sources and sinks which are expanded upon in section 3.10 and 3.11. P_0 and g are the model reference pressure of 50 µPa and the acceleration due to gravity respectively.

The specific heat capacity and thermal conductivity are defined as (Banks and Kockarts, 1973):

$$C_P = k\left(\frac{7}{2}\left(\frac{v_{N_2}}{m_{N_2}} + \frac{v_{O_2}}{m_{O_2}}\right) + \frac{5}{2}\frac{v_O}{m_O}\right) \tag{3.21}$$

$$K_T = (56\ (v_{O_2} + v_{N_2}) + 75.9\ v_O)T^{0.69} \tag{3.22}$$

where v_i and m_i refer to the volume mixing ratio and molecular/atomic masses of the respective species, k is Boltzmann's constant, and T is the neutral temperature.

The temperature at the lower boundary of the model is fixed to a global average value obtained from MSIS, and is dependent on solar activity. The average temperature at the lower boundary is 182 K, with variations on the order of 1% over a solar cycle. At the upper boundary thermal conduction dominates as the heat transport process and we specify the condition $\frac{\partial T}{\partial Z} = 0$.

3.9 Electron and Ion Temperatures

Compared to the background neutral atmosphere, the electron temperature responds quickly to changing conditions and can be solved for by assuming steady state conditions. The electron energy equation takes the form:

$$\sin^2 I \frac{\partial}{\partial z}\left[K_e \frac{\partial T_e}{\partial z}\right] + Q_e - L_e = 0 \tag{3.23}$$

Where I is the magnetic dip angle. An expression for the electron conductivity K_e has been given by Rees and Roble (1975) which accounts for the deviation from that of a fully ionized plasma due to electron-neutral collisions:

$$K_e = 7.5 \times 10^5\, T_e^{5/2}\left(1 + 3.22 \times 10^4 \frac{T_e^2}{n_e}\sum_{n=1}^{3} n_n \bar{Q_{Dn}}\right)^{-1} \tag{3.24}$$

where n_n refers to neutral densities and $\bar{Q_{Dn}}$ are the velocity averaged momentum transfer cross sections. The summation in the above expression is over the densities of the major species.

Ambient ionospheric electrons are primarily heated by collisions with photoelectrons and are cooled by inelastic and elastic collisions with neutrals and ions. Expressions for the

energy loss rates from electrons have been given by Schunk and Nagy (2009) and have been reproduced in Appendix B. Quenching of $N(^2D)$ is also known to be a significant source of electron heating in the F2 region of the ionosphere (Richards, 1986), and is included in the model calculations. It is necessary to specify a heat flux at the upper boundary corresponding to the energy input from the magnetosphere in order to obtain a reasonable electron temperature profile. We adopt a fixed value of 3×10^9 eV cm^{-2} s^{-1} following Roble et al. (1987) as the upper boundary condition in solving for the electron temperature.

The ion temperatures are solved for by assuming local thermodynamic equilibrium. The coloumb collisions that serve as a cooling mechanism for ionospheric electrons serves as the heating mechanism of the ions, while collisions with neutrals serves as the heat sink. Expressions for these energy loss rates have been reproduced from Rees and Roble (1975) in Appendix B. Both electron and ion temperatures are set to be equal to the neutral temperature at the lower boundary of the model.

3.10 Thermospheric heating processes

Neutral gas heating in the thermosphere occurs via a number of processes, namely, 1) absorption of solar radiation by O_2 in the Schumann Runge bands and continuum, 2) joule heating, 3) exothermic neutral-neutral reactions 4) exothermic ion-neutral and ion recombinations reactions, 5) quenching of excited species and 6) thermal collisions with electrons and ions.

A parameterized expression for heating due to absorption of solar radiation by O_2 in the Schumann Runge bands (175-205 nm) has been given by Strobel (1978), which is accurate to within 5% of measurements above 75 km. Similarly, an expression for the heating due to absorption in the Schumann Runge continuum (125-175 nm) has been given by DeMajistre et al. (2001), which reproduces the heating rate within 2%, with uncertainty introduced primarily by the usage of the F10.7 index as a proxy for solar activity. However, the full calculation is not computationally expensive to implement for the low resolution solar flux specification used in the ACE model, and is obtained as:

$$E_c = E_{\min} - (1 - \phi)E_{630} \tag{3.25}$$

where E_c, $E_{\min}$, and E_{630} refer to the energy required to dissociate the O_2 molecule, the minimum energy required to excite one of the product oxygen atoms to the ^1D level, and the energy difference between $O(^1D)$ and $O(^3P)$ respectively. ϕ is the wavelength dependent yield of $O(^1D)$ from the dissociation of O_2, obtained from Lee et al. (1977). The heating rate is then calculated by summing the differences between E_c and the energy of the absorbed photon across all wavelength bins.

Previous thermospheric models by Roble et al. (1987) and Smithtro and Sojka (2005) have noted the need to include joule heating in order to bring the calculated global average neutral

temperatures into agreement with results from MSIS. In both these models, a global energy input of 70 GW proposed by Foster et al. (1983) for geomagnetically quiet conditions was used. More recently, Knipp et al. (2004) presented a value of 95 GW ± 93 GW for the daily average joule heating power, averaged for solar cycles 21 - 23. Due to the large variability present in this value, we continue to use a value of 70 GW here and test the sensitivity of the ACE model to changes in the joule energy input in Chapter 5. The joule heating rate is calculated using the equation:

$$Q_{Joule} = \sigma_P \, E^2 \tag{3.26}$$

Here, σ_P is the Pedersen conductivity and E is the superimposed electric field, assumed to vary between 6.74 - 4.07 mV m^{-1} to keep the net energy input constant.

The list of exothermic neutral-neutral reactions implemented in the model have been tabulated in Appendix A along with their respective rate coefficients and exothermicities. The recombination reaction of atomic oxygen is the dominant source of heating at the lower boundary of the model, while the quenching of excited species is important above 110 km. The exothermic reactions of N(^{2}D) and N(^{4}S) with O_2 are important near 150 km, but their efficiency is significantly reduced due to the chemiluminescence of NO discussed in the previous chapter. We assume that the heating rate of neutrals due to direct impact with photoelectrons is 5% of the total EUV energy absorbed (Stolarski, 1976; Roble et al., 1987). Energy exchange via collisions that serve as the heat sink for electrons and ions serve as the primary heat input into neutrals in the upper thermosphere.

3.11 Thermospheric cooling processes

Infrared emissions at 5.3, 15 and 63 µm by NO, CO_2 and O(^{3}P) respectively have been identified as the dominant sources of radiative cooling in the upper atmosphere. Cooling due to the emission from NO has been treated extensively in the previous chapter and is not repeated here. An expression for the cooling rate above 95 km due to the emission from CO_2 assuming non-local thermodynamic equilibrium (non-LTE) was given by Dickinson (1984):

$$L_{CO_2} = h\nu \; n(M) \; n(CO_2) \; \lambda_{VT1} \times 2 \, e^{-960/T} \tag{3.27}$$

Where n(M) is the density of the species with which CO_2 undergoes energy exchange. The rate coefficient of the process, λ_{VT1}, is given as:

$$\lambda_{VT1} = \lambda_{VT}^{M} + r_O \lambda_{VT}^{O} \tag{3.28}$$

$$\begin{aligned} \lambda_{VT}^{M} &= 2.5 \times 10^{-15} \text{ cm}^3 \text{ s}^{-1}, \qquad T < 200 \text{ K} \\ &= 2.5 \times 10^{-15}(1 + 0.03(T - 200)) \text{ cm}^3 \text{ s}^{-1}, \quad T \geq 200 \text{ K} \end{aligned} \tag{3.29}$$

$$\lambda_{VT}^{O} = 2 \times 10^{-13} \text{ cm}^3 \text{ s}^{-1} \tag{3.30}$$

where $M(= O_2, N_2)$ and O are the species which undergo energy exchange with CO_2. r_O is the volume mixing ratio of atomic oxygen. A revised expression for λ_{VT}^{O} has been obtained from the experimental results of Castle et al. (2012) which indicates a small negative temperature dependence. Using a quadratic fit to the temperature between 142 - 490 K, the rate coefficient is given as:

$$\begin{aligned} \lambda_{VT}^{O} &= (3.8 - 9.51 \times 10^{-3}\ T_n + 9.32 \times 10^{-6}\ T_n^2) \times 10^{-12} \text{ cm}^3 \text{ s}^{-1} \\ &= 1.38 \times 10^{-12} \text{ cm}^3 \text{ s}^{-1} \qquad T_n > 490 \text{ K} \end{aligned} \tag{3.31}$$

An expression for the cooling rate due to the 63 µm emission from O(^{3}P) given by Kockarts and Peetermans (1970) is used in the model:

$$L_{O(^3P)} = X' \ \frac{1.69 \times 10^{-18}\, n(O)\, e^{-228/T}}{1 + 0.6\, e^{-228/T} + 0.2\, e^{-326/T}} \text{ ergs cm}^3 \text{ s}^{-1} \tag{3.32}$$

The factor of 1.69×10^{-18} corresponds to the product of the energy of the 63 µm photon (3.16×10^{-14} ergs), the transition probability associated with the emission (8.95×10^{-5} s^{-1}) and a statistical weight associated with the ^{3}P level (0.6). In the above expression, X' is the altitude dependent reduction factor that varies from 0 near 100 km to 0.8 above 200 km. The reduction factor accounts for the efficiency of this cooling mechanism as a function of the optical thickness of the atmosphere. Roble et al. (1987) scaled this cooling rate by a factor of 0.5 following the measurements of Offermann and Grossmann (1978) which suggested that the O(^{3}P) population in the upper thermosphere was not in thermodynamic equilibrium (non-LTE conditions). Subsequent modeling work by Sharma et al. (1994) and measurements by Grossmann and Vollmann (1997) have shown this assumption to be incorrect, and we do not apply a scaling factor to equation 3.32. The sensitivity of thermospheric temperatures to this scaling factor is considered in Chapter 5.

Chapter 4

Model Results

The ACE1D model was run for a range of solar irradiances expected over the course of a solar cycle, the results of which are presented in this chapter. The model was initialized with a typical thermospheric profile for the major species and the neutral temperature, with the densities of neutral minor species and ions set to zero. For a given solar irradiance, the model first solves for the densities of minor species and ions until steady state conditions are achieved, and then solves the complete set of continuity and energy equations for all species and temperatures. The model is run with a time step of one minute, and steady state is reached in approximately 30 days of model time. We use the parameter P, defined as the average of the F10.7d and F10.7a solar indices as a proxy for solar activity. Geomagnetically quiet conditions are assumed for the model runs presented here.

4.1 Model Inputs

As described in the previous chapter, the ACE1D model uses a combination of solar fluxes, joule heating and magnetospheric flux as energy inputs to the thermosphere. Of these, only the solar fluxes are considered to vary as a function of solar activity (section 3.7). Figure 4.1 shows the solar fluxes used to drive the model at solar minimum and maximum ($P = 70,\ 250$), along with the reference solar spectrum to which the scaling factors are applied. To accurately reproduce the calculations obtained from high resolution solar spectra, the model uses variable bin sizes to specify the flux between $0.05 - 105$ nm, and 5 nm wide bins between 105 and 175 nm. A separate bin is used to specify the flux for the Lyman-α emission at 121.57 nm. The variability of the solar spectrum over the course of the solar cycle can be seen in the ratio S_{max}/S_{min}. The ratio shows significant variation in the EUV and XUV fluxes as a result of the variability present in the solar corona where they are produced, while longer wavelengths of the solar spectrum emitted by regions closer to the solar surface exhibit less variability over a solar cycle.

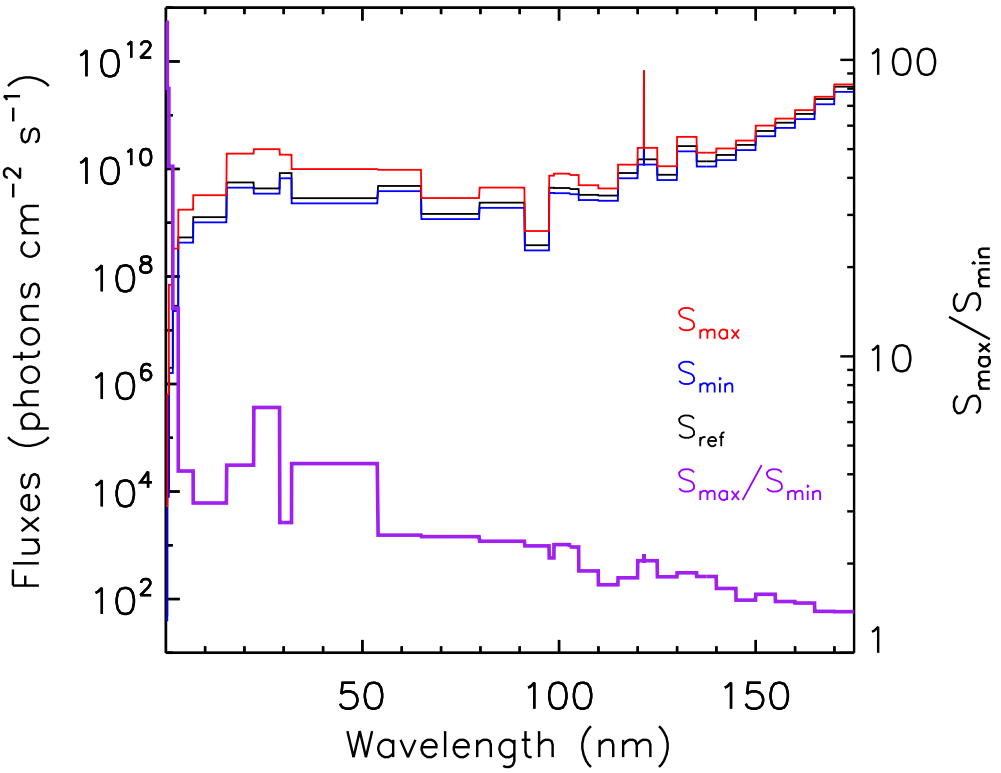

Figure 4.1: Solar flux inputs to the model at solar maximum (red), solar minimum (blue), and the reference solar spectrum (black). Also shown is the binwise ratio between the fluxes at solar maximum and minimum (purple).

4.2 Major Species

Model calculations of the densities of major species are shown in Figure 4.2 for solar minimum and maximum, along with the global average values predicted by MSIS. The model results are seen to be in reasonable agreement with MSIS values, with the largest difference between the two models seen in the O_2 densities at solar maximum near 200 km, where the ACE1D model predicts a value of 3.25×10^8 cm^{-3} compared to the MSIS value of 2.22×10^8 cm^{-3} (46% difference). The difference between MSIS and model calculations in the N_2 and O densities at this altitude are 25% and 5% respectively. The calculated mass densities from the model are found to be within 15% of the MSIS values at all altitudes.

4.3 Neutral, Electron and Ion temperatures

Neutral, electron and ion temperatures calculated from the model are shown in Figure 4.3, along with neutral temperatures from MSIS. When the model is run using solar fluxes as the only input, the calculated exospheric neutral temperatures are 546 and 1271 K at solar minimum and maximum respectively, compared to the corresponding MSIS values of 740 and 1273 K. While there is good agreement with the MSIS result for the case of $P = 250$, it was found necessary to include a joule energy input in the model in order to bring the temperatures into reasonable agreement with MSIS over a wide range of solar activity. Following Roble et al. (1987) and Smithtro and Sojka (2005) we specify a global joule energy input of 70 GW, resulting in a model calculated exospheric neutral temperature of 643 K and 1364 K which correspond to a difference of 13 and 8% with the respective MSIS results.

The slightly larger difference in exospheric temperatures at solar minimum is caused by the solar input specification (section 3.7), where fluxes are scaled to 80% of their reference value for $P < 80$. Figure 4.4 plots the exospheric temperatures from ACE1D and MSIS as a function of solar activity, which show agreement within 10% for $P \geq 80$. The figure also shows the integrated energy from XUV/EUV solar fluxes between 0.05 - 110 nm, which are well correlated with the calculated exospheric temperatures. The nearly linear response of the exospheric temperature to solar fluxes calculated by ACE1D is in contrast to the non-linear response predicted by MSIS over the course of a solar cycle. If we assume that the exospheric temperatures do respond linearly to increases in the solar energy input, the model calculations suggest that the variations in the solar input are not adequately captured by the solar flux model described section 3.7, particularly at higher levels of solar activity.

The modeled ion and electron temperatures are similar to the results of Roble et al. (1987) and Smithtro and Sojka (2005) in terms of structure and magnitude. While both temperatures are seen to be tied to the neutral temperatures in the lower thermosphere, the electron temperature profiles show a steep increase near 150 km that reflects the effect of photoelectron heating. Calculations of the photoelectron heating rate of the ambient electron gas is

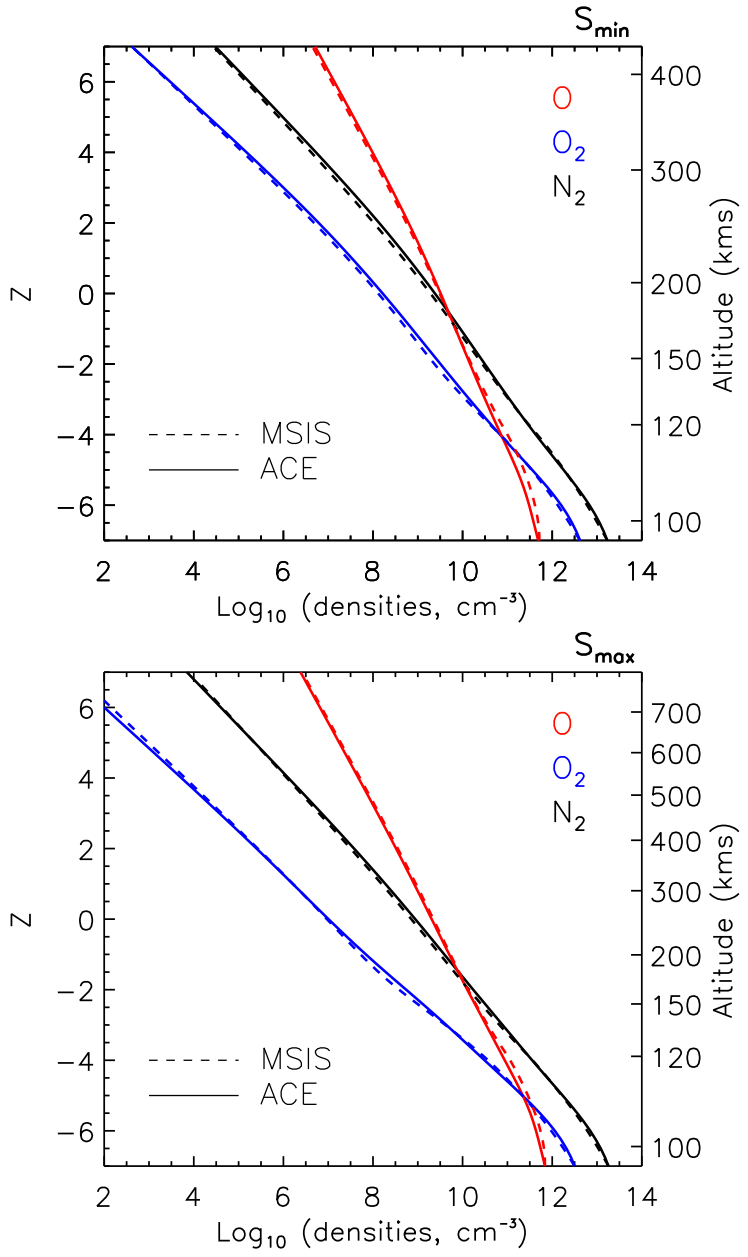

Figure 4.2: Comparisons between ACE1D calculations (solid lines) and MSIS00 results (dashed lines) of major species densities in the thermosphere for solar minimum ($P = 70$) (top) and solar maximum ($P = 250$) (bottom).

shown in Figure 4.5, which indicates that photoelectrons produced by solar fluxes between 0-55 nm are the primary source of electron heating. Above 150 km, energy exchange via collisions with neutrals and ions reduces the gradient of the elctron temperature. However, the positive gradient is maintained as a result of the magnetospheric energy flux of 3×10^9 eV cm^{-2} s^{-1} specified at the upper boundary.

4.4 Minor species

The calculated densities of neutral minor species are shown in Figure 4.6. The densities of N_2(A), O(^{1}D), N(^{2}D), and N(^{2}P) are calculated for assuming photochemical equilibrium (PCE), while diffusion effects are accounted for in the density calculations of NO and N(^{4}S).

The ACE1D model calculates the $v = 0 - 7$ level densities for N_2(A), and the sum of these densities are shown in Figure 4.6. For equatorial noon, Yonker (2013) indicated a peak density of approximately $2.95 - 3.8 \times 10^3$ cm^{-3} near 160 km for moderately high levels of solar activity ($P = 155,\ 183$). The ACE1D model calculates a peak density of $5.6 \times 10^2 - 1.4 \times 10^3$ cm^{-3} at solar minimum and maximum respectively, with a peak altitude ranging between $150 - 170$ km. The difference in densities is attributed to the strong diurnal variation in the production rate of N_2(A) noted by Yonker (2013), and the fact that ACE1D computes a global average profile of the N_2(A) density.

The electronically excited state of atomic oxygen, O(^{1}D), is the source of the 630 nm airglow emission from the thermosphere. It is primarily produced in the thermosphere via O_2^+ recombination, O_2 dissociation, and photoelectron excitation of atomic oxygen. As photoelectron fluxes are not explicitly calculated in the model, excitation of atomic oxygen is not presently included as a source of O(^{1}D). As a result, modeled densities are significantly smaller than the densities indicated by sounding rocket measurements (Solomon and Abreu (1989)). While the reaction of N(^{2}D) with O_2 as a potential source of O(^{1}D) has been debated in the past (Solomon et al., 1988; Link and Swaminathan, 1992), the ACE1D model the most recent experimental result of Miller and Hunter (2004) which indicated a negligible yield for the O(^{1}D) channel.

Densities of the excited atomic nitrogen species N(^{2}D) and N(^{2}P) are inferred in the thermosphere by observing emissions at 520 and 346.6 nm, denoting their radiative relaxation to the N(^{4}S) ground state. However, there are no definitive global measurements of these emissions. The model calculates a peak N(^{2}D) density of 2×10^5 cm^{-3} for solar minimum and 5.3×10^5 cm^{-3} for solar maximum, while the corresponding values for N(^{2}P) are 7.3×10^2 cm^{-3} and 1.5×10^3 cm^{-3}.

To ascertain the effect of the diffusion terms in Eq. 3.12, densities for N(^{4}S) and NO were also calculated assuming PCE conditions and are shown along with the full calculation in Figure 4.6. For N(^{4}S), the peak density is seen to move from 258 to 168 km during solar mininum, and from 329 to 201 km during solar maximum. In both cases, the peak N(^{4}S)

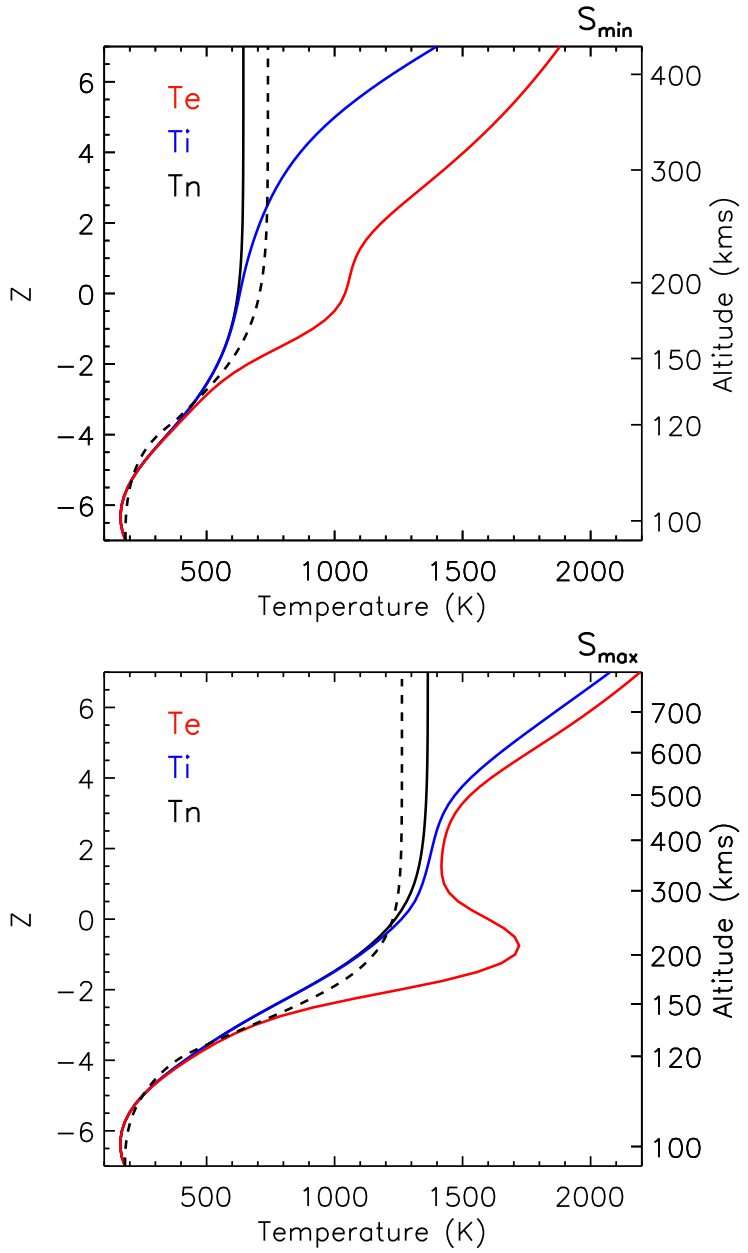

Figure 4.3: ACE1D model calculations of neutral, ion and electron temperatures in the thermosphere for solar minimum ($P = 70$) (top) and solar maximum ($P = 250$) (bottom). Also shown are neutral temperatures from MSIS (dashed line)

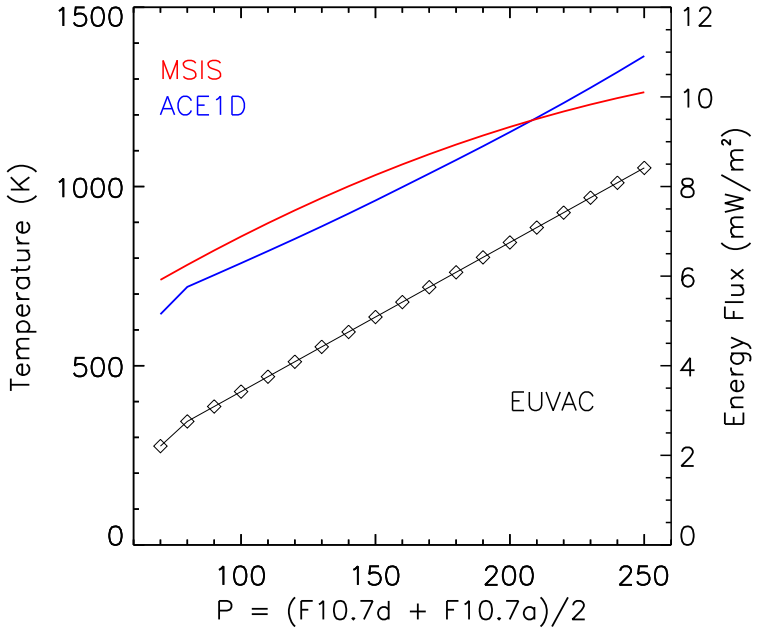

Figure 4.4: ACE1D model calculations (red) and MSIS predictions (blue) of exospheric temperatures, and integrated solar fluxes (0.05 - 110 nm) from EUVAC (diamonds) as a function of solar activity.

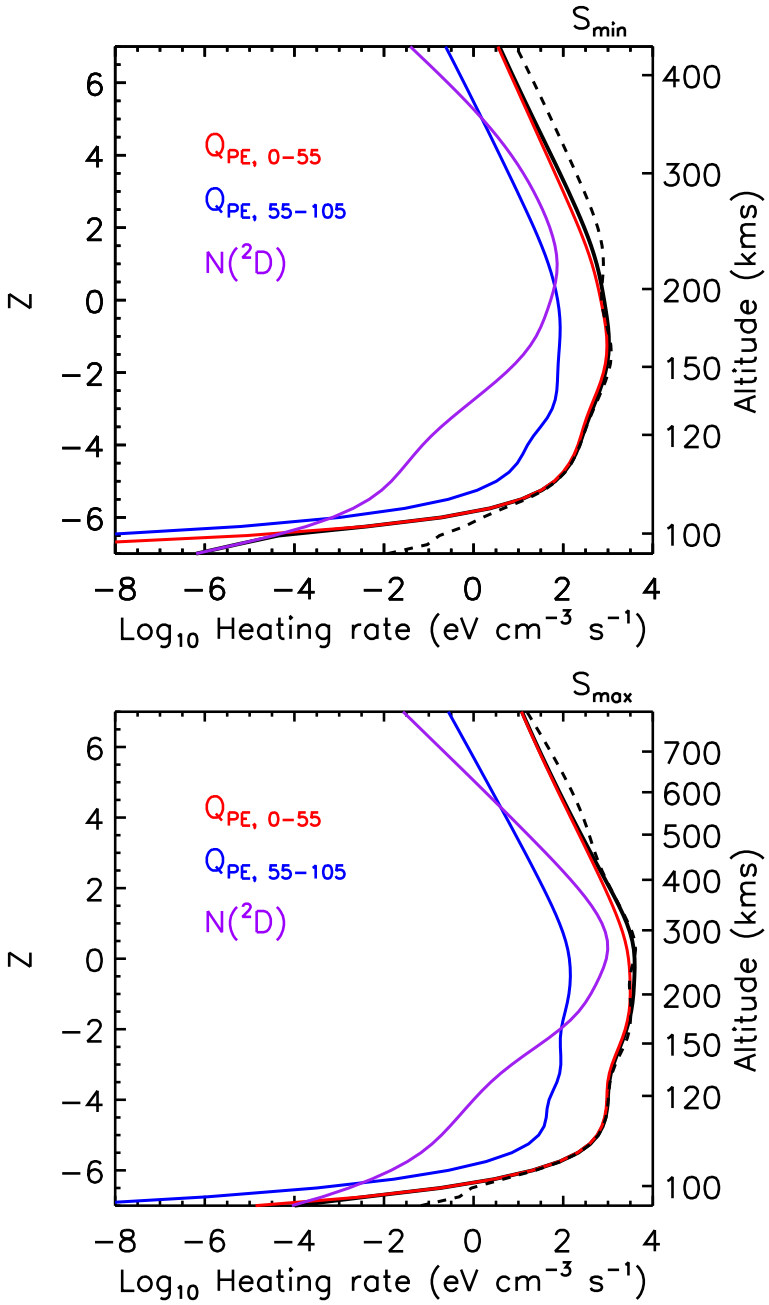

Figure 4.5: ACE1D model calculations of electron heating and cooling rates at solar minimum ($P = 70$) (top) and solar maximum ($P = 250$) (bottom). Shown are the heating rates due to collisions with photoelectrons produced by solar flux between 0-55 nm (red), 55-105 nm (blue) and the heating rate due to quenching of N(^{2}D) (purple). The net heating rate is denoted by the solid black line. The dashed black line denotes the net electron gas cooling rate due to collisions with ions and neutrals.

density decreases approximately by a factor of 5.

The NO chemistry implemented in the ACE1D model follows the comprehensive review of processes given by Yonker (2013). It can be seen from Figure 4.6 that diffusion has a negligible effect on the peak NO densities near 110 km, particularly for high solar activity. The peak density for the two cases are 3.7×10^7 cm^{-3} and 9.6×10^7 cm^{-3} respectively, which is a factor of $2 - 3$ larger than those predicted by Roble et al. (1987). Figure 4.7 shows the NO profile between 100 and 200 km calculated for $P = 70$, 150 and 200, which indicates a slight decrease in the location of the density peak from 109 to 106 km with increasing solar activity, caused by the increase in the production from N(^{2}D). The location of the peak was however found to be independent of the downward flux specified at the lower boundary to constrain Eq. 3.12.

The dominant production and loss sources used to calculate NO densities have been shown in Figure 4.8. The reaction of N(^{2}D) with O_2 is the dominant production source of NO, while the temperature dependent reaction of N(^{4}S) with O_2 is an important source only above 150 km. Loss to N(^{4}S) is also seen to be the dominant NO sink throughout the thermosphere, while charge exchange with O_2^+ and photolysis are important in the lower thermosphere below 120 km. The SNOE satellite made measurements of NO densities in the thermosphere between $100 - 170$ km from 1998 to 2003. Placed in a sun synchronous orbit, the satellite made 15 daily measurements at an average local time of 11 am with nearly pole-to-pole coverage. Figure 4.9 shows global average NO densities at 106 km obtained from SNOE plotted as a function of solar activity, along with the standard deviation of the measurements. The increase in the variability of the measurements with solar activity reflects the variability in the XUV and EUV solar fluxes that drive NO production in the thermosphere. While the ACE1D calculations agree with the general trend of the measurements from SNOE, they are approximately 25% smaller than the mean SNOE values at moderate to high solar activity levels. This is expected as the model calculates a global average value for the NO peak, whereas SNOE measurements were obtained for 11 am.

4.5 Ionospheric Densities

Figure 4.10 shows ACE1D calculations for globally averaged ion and electron densities. The model calculates a peak electron density of 1.5×10^5 cm^{-3} at 227 km for solar minimum and a density of 8.7×10^5 cm^{-3} at 329 km for solar maximum. The E region of the ionosphere below 200 km is comprised primarily of NO^+ and O_2^+ ions, while O^+ is the dominant ion in the F region above 200 km. N_2^+, N^+, O^+(^{2}D) and O^+(^{2}P) are seen to be minor ionospheric constituents at all altitudes, which are produced primarily by the ionization and dissociative ionization of N_2 and O_2.

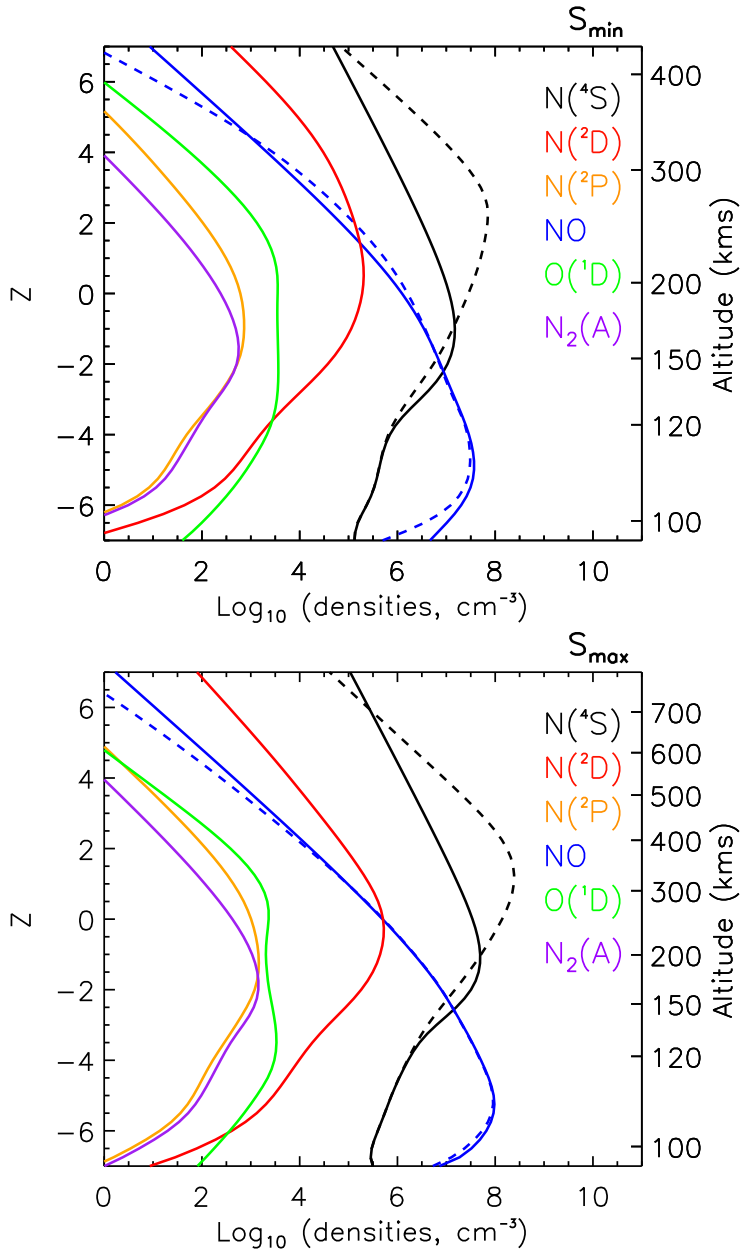

Figure 4.6: ACE1D model calculations of minor species densities in the thermosphere for solar minimum ($P = 70$) (top) and solar maximum ($P = 250$) (bottom). Dashed lines indicate calculations of NO and N(^{4}S) densities assuming PCE.

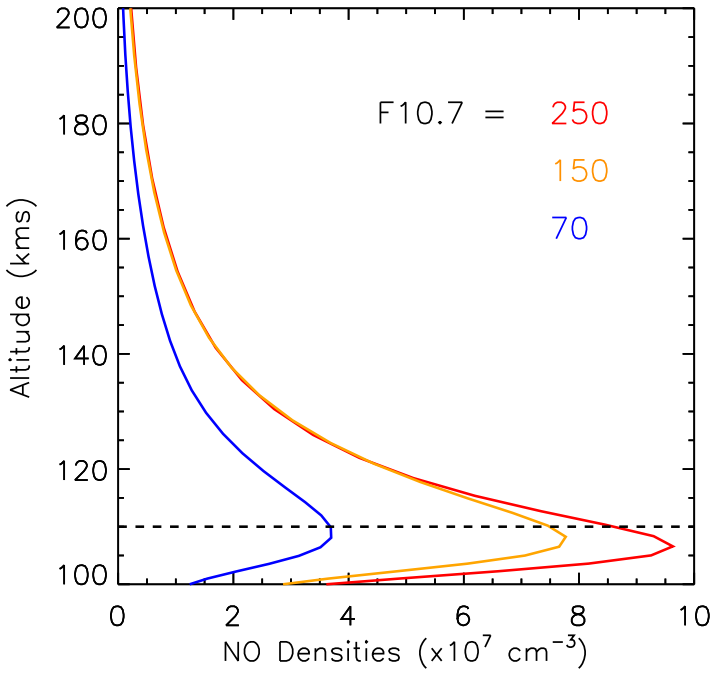

Figure 4.7: ACE1D model calculations of NO densities as a function of solar activity. The dashed line indicates an altitude of 110 km shown for reference.

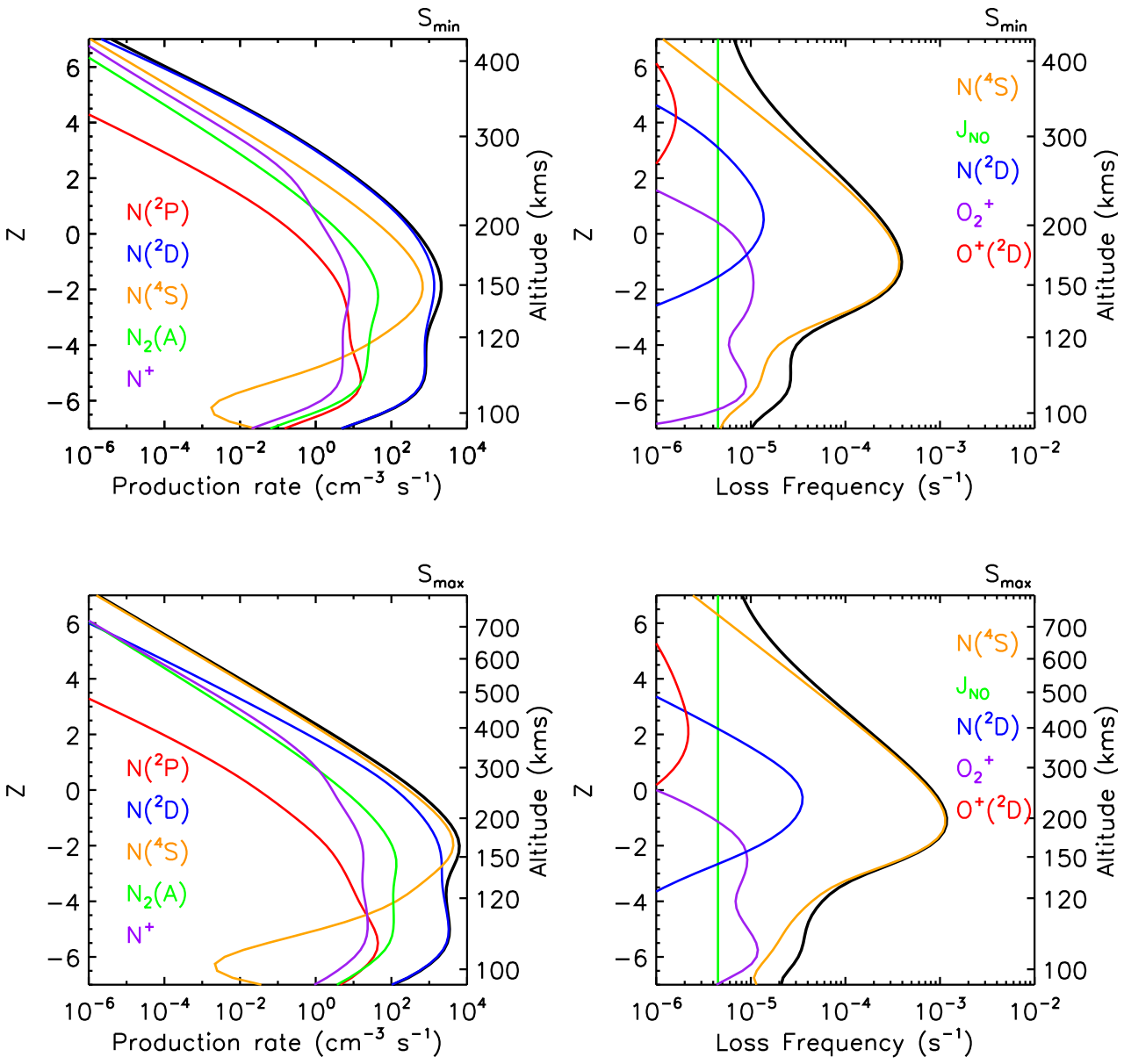

Figure 4.8: ACE1D model calculations of NO production rates and loss frequencies for solar minimum (top) and maximum (bottom). The production terms refer to the reaction of $N(^2P)$ (red), $N(^2D)$ (blue) $N(^4S)$ (orange), and N^+ (purple) with O_2, and $N_2(A)$ with atomic oxygen (green). The loss terms refer to reactions with $N(^4S)$ (orange), $N(^2D)$ (blue), photodissociation (J_{NO}, green), and charge exchange with O_2^+ (purple) and $O^+(^2D)$ (red). Minor losses to charge exchange with O^+, N^+ and N_2^+ are not shown. The net production rate and loss frequency in each case is shown in black.

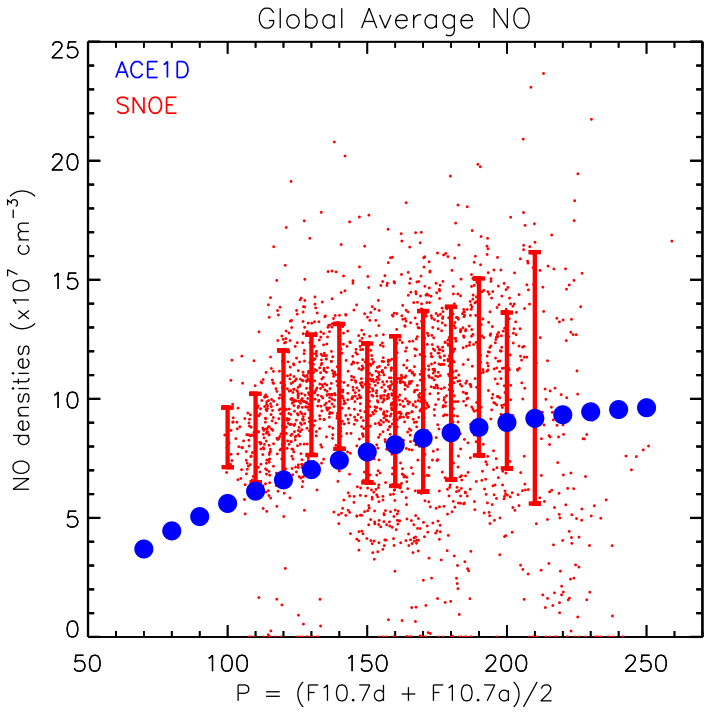

Figure 4.9: Comparison between measured and calculated global average peak NO densities from SNOE and ACE. Red points indicates measurements, along with red vertical lines that show the error bars of the measurements. Blue circles indicate modeled peak NO densities obtained from ACE.

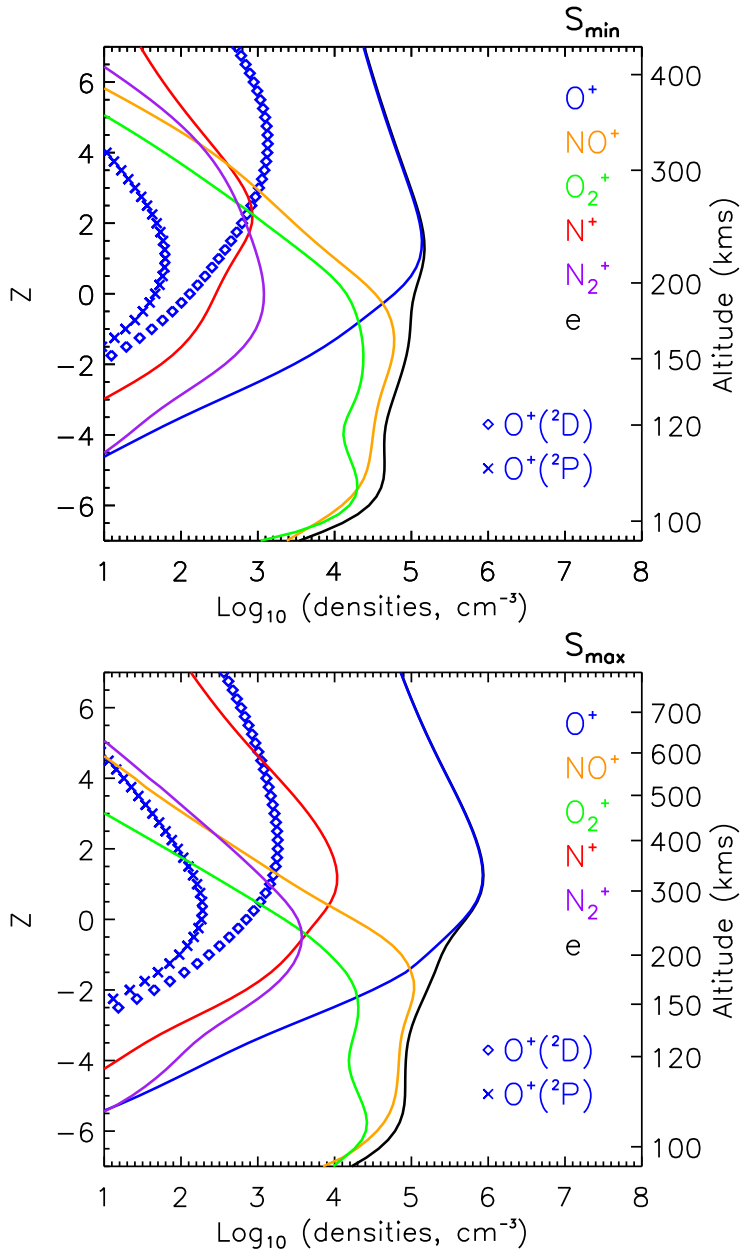

Figure 4.10: ACE1D model calculations of ion densities in the thermosphere for solar minimum ($P = 70$) (top) and solar maximum ($P = 250$) (bottom).

4.6 Model sensitivity to solar fluxes

In order to assess the importance of individual wavelength bins of the solar flux specification (Appendix C) on the model output, a series of model runs were made where each run corresponded to one bin of the solar flux being set to zero. As the solar spectrum does not exhibit uniform variability at all wavelengths (Figure 4.1), the sensitivity of the outputs were tested at both solar minimum and maximum conditions.

Figure 4.11 shows variations in the peak density of NO, N(^{4}S) and N(^{2}D) as a function of solar irradiance. The change in density is referenced to the model run where solar fluxes from all bins are included in the input, and the values plotted correspond to the effect of setting the flux of a given bin to zero. It is seen that the NO density peak reduces by an average of 45% as a result of the removal of XUV fluxes from the solar input. This is driven by a reduction in the ionization of N_2^+ which generally undergoes dissociative recombination to produce N(^{2}D). However, not all wavelength bins below 10 nm have an equal effect on the NO densities as the ionization rate also depends on the absorption cross-sections and the ionization branching ratios. The Lyman-β line at 102.6 nm which ionizes O_2 is a loss source for NO, as it undergoes charge exchange with the O_2^+ produced. Removing the solar flux at this wavelength results in an increase of NO densities by about 10%. Solar fluxes at FUV wavelengths ($>$ 150 nm) primarily cause the dissociation of O_2, in the absence of which the loss of N(^{4}S) to O_2 increases. The resulting reduction in N(^{4}S) densities below 200 km cause a corresponding increase in the peak NO density near 110 km. Variations in the NO column density as a function of solar irradiances are shown in Figure 4.12, along with the normalized absolute net changes due to soft x-rays, the He II line at 30.4 nm, extreme ultraviolet radiation, and far ultraviolet radiation. These plots show that NO production rates are most sensitive to energy deposition at XUV ($0.05 - 29$ nm) wavelenghts, while NO losses are influenced by FUV ($105 - 175$ nm) wavelengths.

Changes to the peak densities of ionospheric species are shown in Figure 4.13 . It is important to note that the location of the peak density of O_2^+ is a function of solar activity (4.10), as the peak altitude of solar energy deposition decreases with increase in solar activity. As a result the changes in the O_2^+ density shown in Figure 4.13 correspond to two different altitudes. This results in the reduction of NO densities due to changes in the XUV flux being reflected in that of O_2^+ at solar maximum but not at solar minimum. A similar effect is seen for the Lyman$-\beta$ emission.

The EUV portion of the solar spectra results in the ionization of O^+ and N_2^+, and the largest reduction in ion densities is seen on removing fluxes between $22-32$ nm. The ionization limit of N_2^+ (80 nm) is also seen in the plots, beyond which changes to the solar flux are not directly reflected in the densities. Reduction in the dissociation of O_2 causes the density trends at FUV wavelengths, resulting in reduced O^+ densities. As N_2^+ is lost to charge exchange with O, there is a corresponding increase in its densities at these wavelengths. Reductions in the F-region electron peak density is shown in Figure 4.14 and are seen to reflect the variations

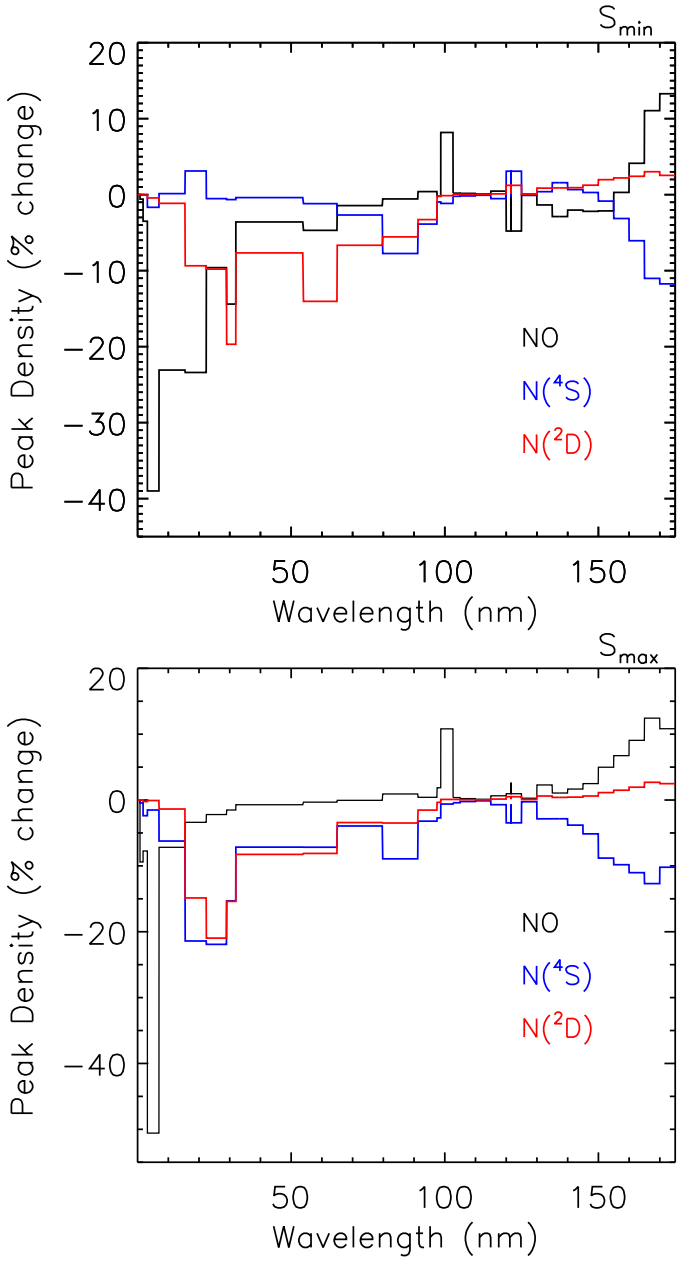

Figure 4.11: Variation in peak density of NO (black), N(^{4}S) (blue) and N(^{2}D) (red) in the thermosphere as a function of solar irradiance.

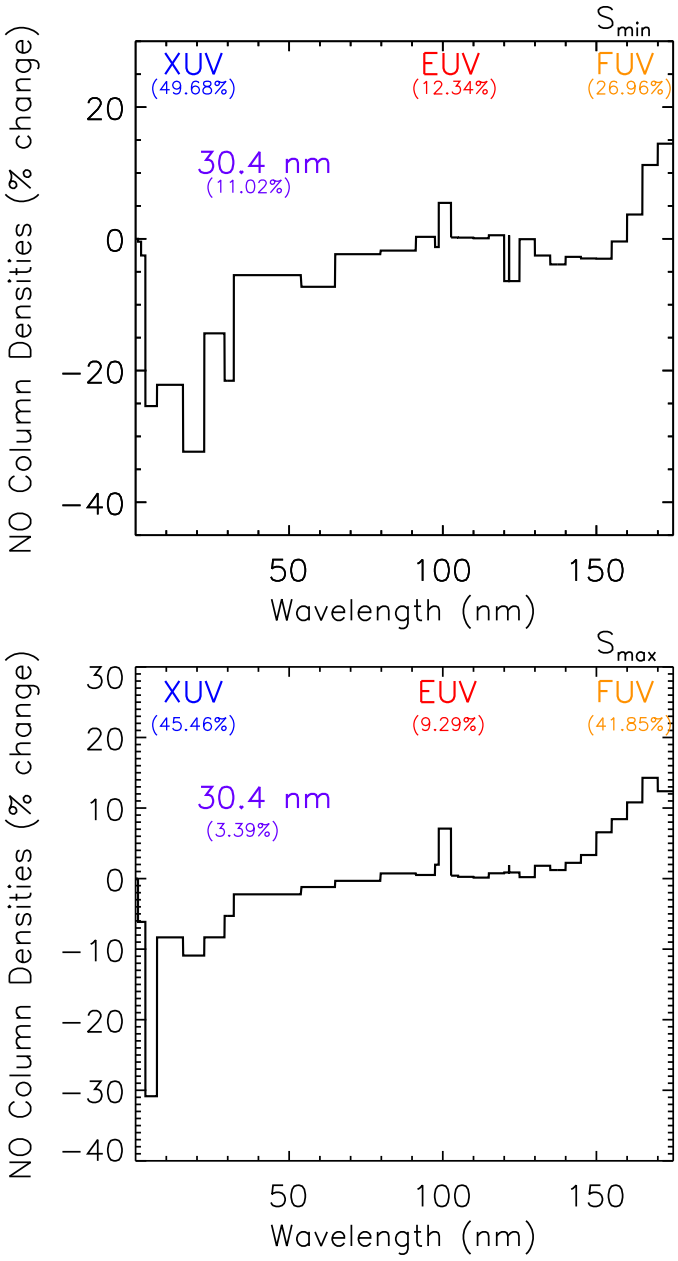

Figure 4.12: Variation in column densities of NO as a function of solar irradiance. The labels indicate contributions of different portions of the solar flux specification: soft x-rays (XUV, $0.05-29$ nm), the He II line (30.4, $29-32$ nm), extreme ultraviolet radiation (EUV, $32-105$ nm), and far ultraviolet radiation (FUV, $105-175$ nm).

in the O^+ density. As NO^+ is predominantly produced as a result of charge exchange of NO with other ionized species, variations in the solar input are generally not reflected in its densities. The exceptions to this are seen at XUV wavelengths which significantly influence the peak NO density, and for the Lyman-β bin, which influences NO and O_2^+ densities.

4.7 Review

The ACE1D model was developed in order to produce a global average representation of the coupled thermosphere and ionosphere system by using an updated physical and chemical scheme of upper atmospheric processes. The model solves a set of one dimensional continuity equations to obtain the density profiles of various neutral and charged species, and a set of energy equations to obtain the neutral, electron and ion temperatures in the upper atmosphere. Solar fluxes below 175 nm serves as the primary energy input to the model, with additional inputs specified to account for high latitude heating sources. The modeled neutral temperatures and densities of major species are shown to be in reasonable agreement with empirical results for a range of solar activities, and the modeled NO densities are in line with existing measurements.

The ACE1D model improves on existing global average thermospheric models by using radiative cooling rates from various processes that are consistent with values suggested in literature. In particular, it is shown that reducing the radiative cooling rate due to NO by a factor of 2 can be consistent with calculating thermospheric temperatures to within 10% of empirically derived values. This is achieved by implementing a comprehensive treatment of various heating and cooling processes including the chemiluminescent emission from NO discussed in Chapter 2. A further discussion on the importance of various heating and cooling parameters and the sensitivity of modeled exospheric temperatures to them is presented in Chapter 5.

While the ACE1D model cannot be used to study diurnal variations and localized phenomena in the upper atmosphere, the reduction in complexity allows it to be easily used for tests such as those shown in section 4.6. Consequently, the ACE1D model can serve to test variations in modeling parameters and processes before they are implemented into more complex models of the thermosphere.

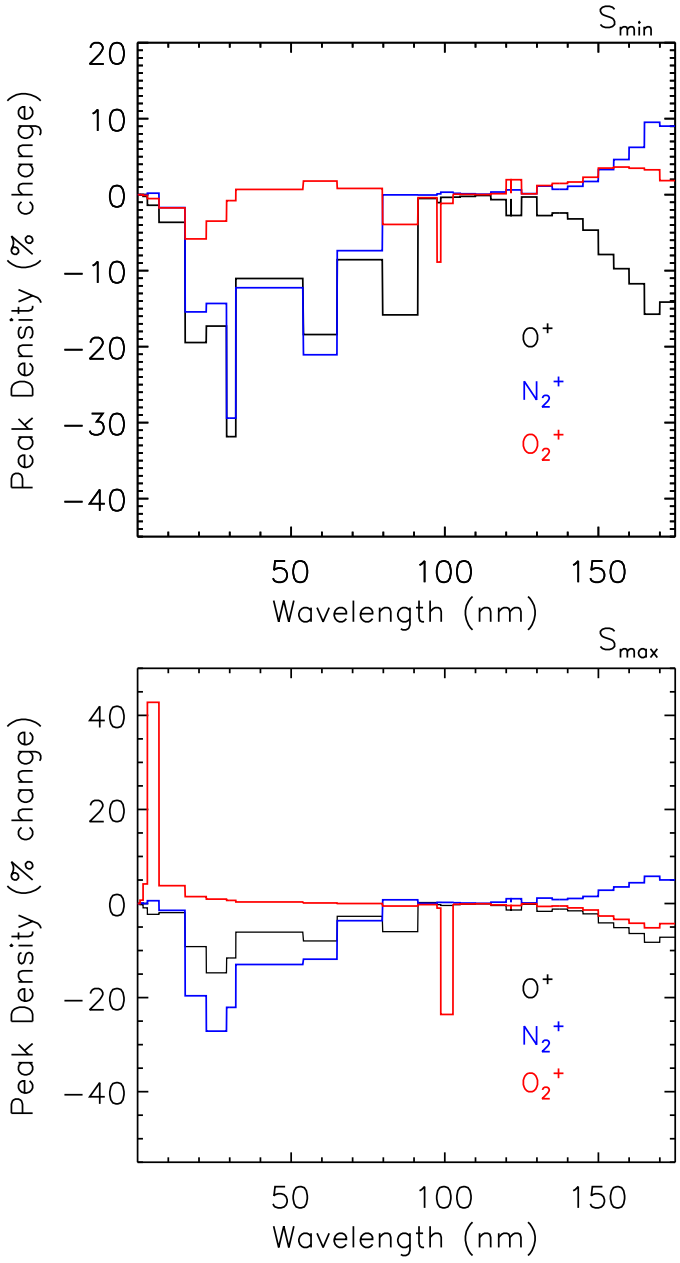

Figure 4.13: Variation in peak density of O^+ (black), N_2^+ (blue) and O_2^+ (red) in the thermosphere as a function of solar irradiance.

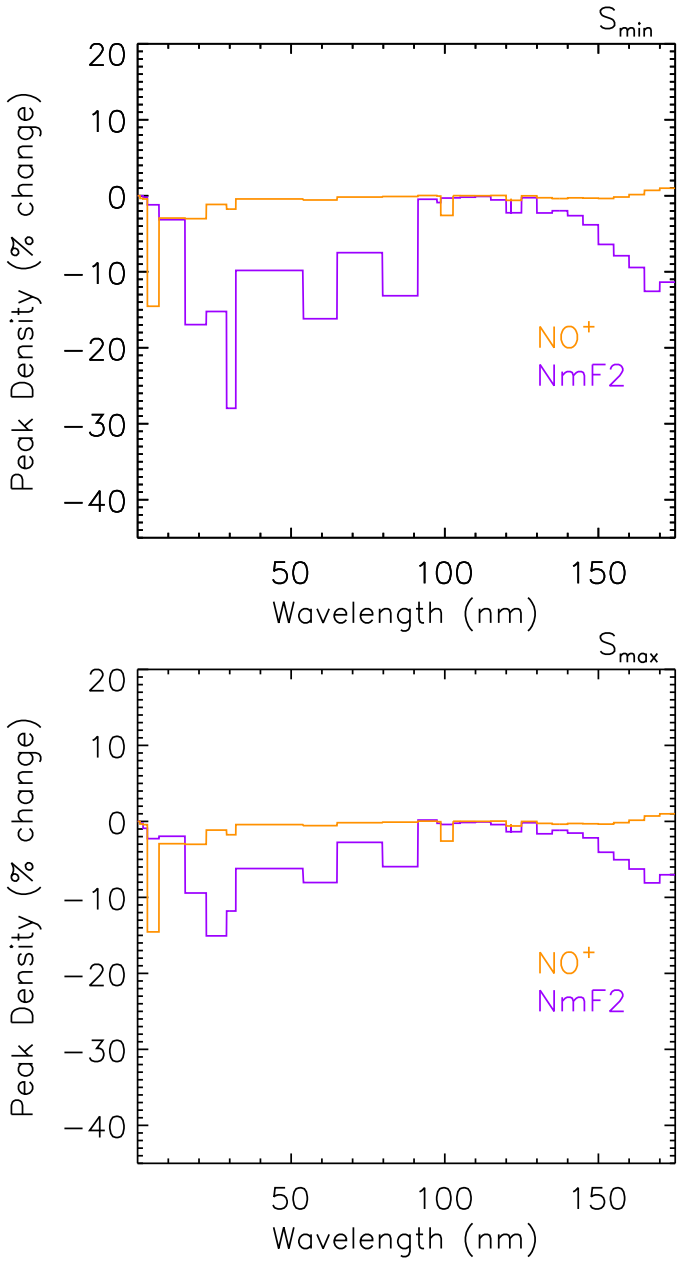

Figure 4.14: Change in the F2 region peak electron density and NO^+ density as a function of solar irradiance.

Chapter 5

The Thermospheric Energy Budget

Neutral temperatures in the thermosphere are governed by a number of heating and cooling processes, as shown in Figure 5.1. The ACE1D model calculates the heating and cooling rates from these processes at each time step to solve for the temperature using Equation 3.20. In this chapter, we examine the relative importance of each of these processes contribution of each of these processes to the thermospheric energy budget.

5.1 Thermospheric Heating

Model calculations of the various neutral gas heating sources are shown for solar minimum and maximum in Figure 5.2, along with the fractional contribution of each process as a function of altitude. The peak heating rates calculated for the two cases are 1.3×10^5 ergs g^{-1} s^{-1} and 5.2×10^5 ergs g^{-1} s^{-1} respectively, compared to the values of 1.5×10^5 ergs g^{-1} s^{-1} and 4.6×10^5 ergs g^{-1} s^{-1} obtained by Roble et al. (1987).

Thermospheric heating can broadly be considered to be dominated by processes involving neutral species below 200 km and charged species above this altitude. The importance of individual processes to the net heating rate is also a function of altitude and solar activity. It is seen that absorption at EUV wavelengths by O_2 in the Schumann Runge continuum and bands, and quenching of excited species are the dominant heating sources below 150 km. Absorption in the Schumann Runge continuum and bands has a peak contribution to the net heating rate that varies between 50% at solar minimum to 36% at solar maximum, while that due to quenching of excited species remains constant at approximately 55%.

Exothermic neutral-neutral reactions are important near the base of the thermosphere where atomic oxygen recombination occurs, and between 150-200 km where heating due to odd nitrogen chemistry is important. Components of the heating due to neutral chemistry and quenching of excited species are shown in Figures 5.3 and 5.4.

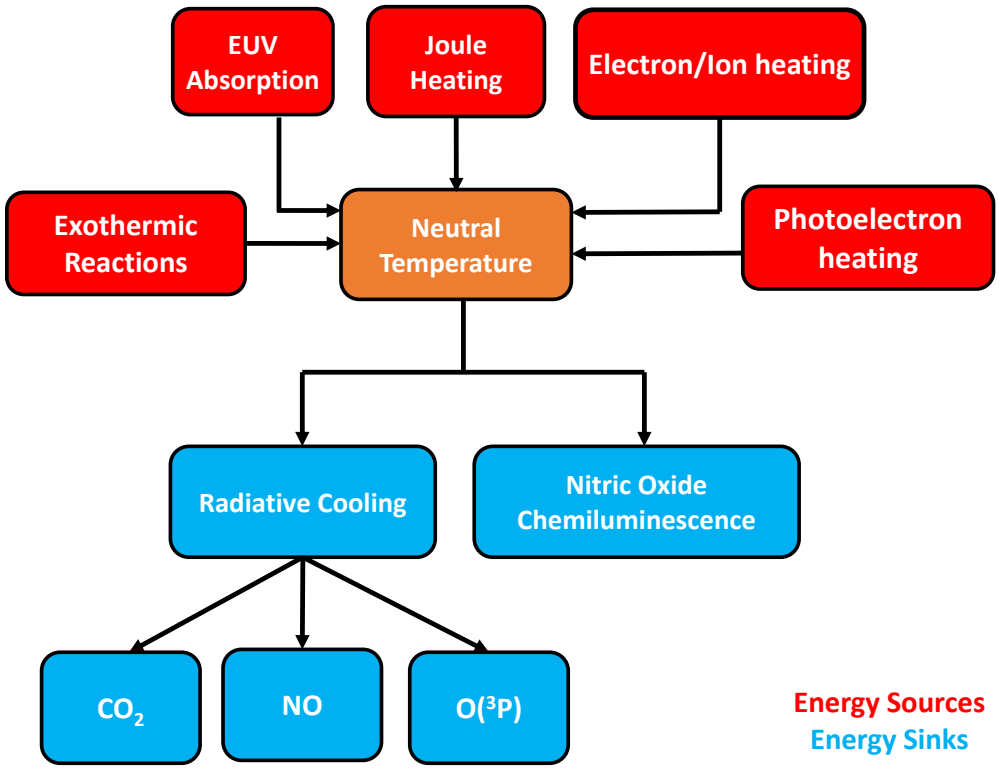

Figure 5.1: Schematic of the energy sources and sinks governing neutral temperatures in the thermosphere.

Joule heating, which is specified to have a fixed power input of 70 GW in the model, reduces in importance as a heating mechanism with increasing solar activity. At solar minimum, it has a peak contribution of 27% in the lower thermosphere, which reduces to 15% at solar maximum. Heating due to collisions with energetic photoelectrons has a peak contribution of approximately 10% for both levels of solar activity. In the upper thermosphere, collisions with ions and electrons are the dominant source of neutral heating.

5.2 Thermospheric Cooling

The components of thermospheric cooling are shown in Figure 5.5. It is important to note that molecular conduction and eddy diffusion are not strictly "cooling" processes, as they generally serve to transport heat from higher to lower altitudes. For example, it is seen that thermal conduction (K_T) serves as the dominant heat loss mechanism from the upper thermosphere, balancing the neutral heating processes above 150 km (Figure 5.2). However,

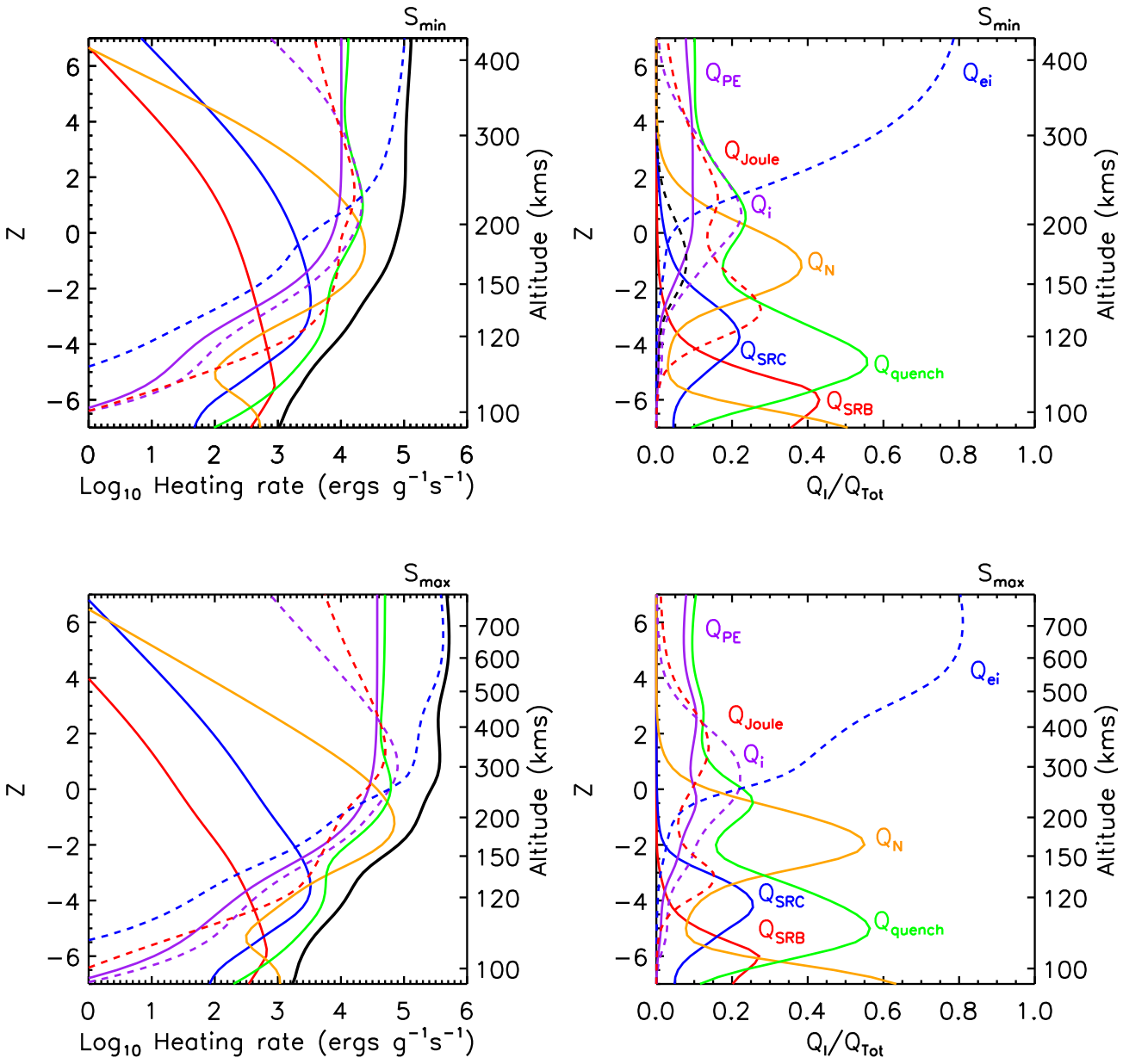

Figure 5.2: ACE1D model calculations of neutral gas heating rates for solar minimum ($P = 70$) (top) and solar maximum ($P = 250$) (bottom). On the left column are the magnitudes of the heating rates and on the right column are the fractional contribution of each process. Shown are the total heating rate (black), heating due to absorption in the Schumann Runge bands (Q_{SRB}, red) and Schumann Runge continuum (Q_{SRC}, blue), direct heating due to thermal collisions with photoelectrons (Q_{PE}, purple), exothermic reactions of neutral species (Q_N, orange), quenching of excited species (Q_{quench}, green), exothermic ion recombination and ion-neutral reactions (Q_i, purple dashed), joule heating (Q_{Joule}, red dashed) and thermal collisions of neutrals with ions and electrons (Q_{ei}, blue dashed).

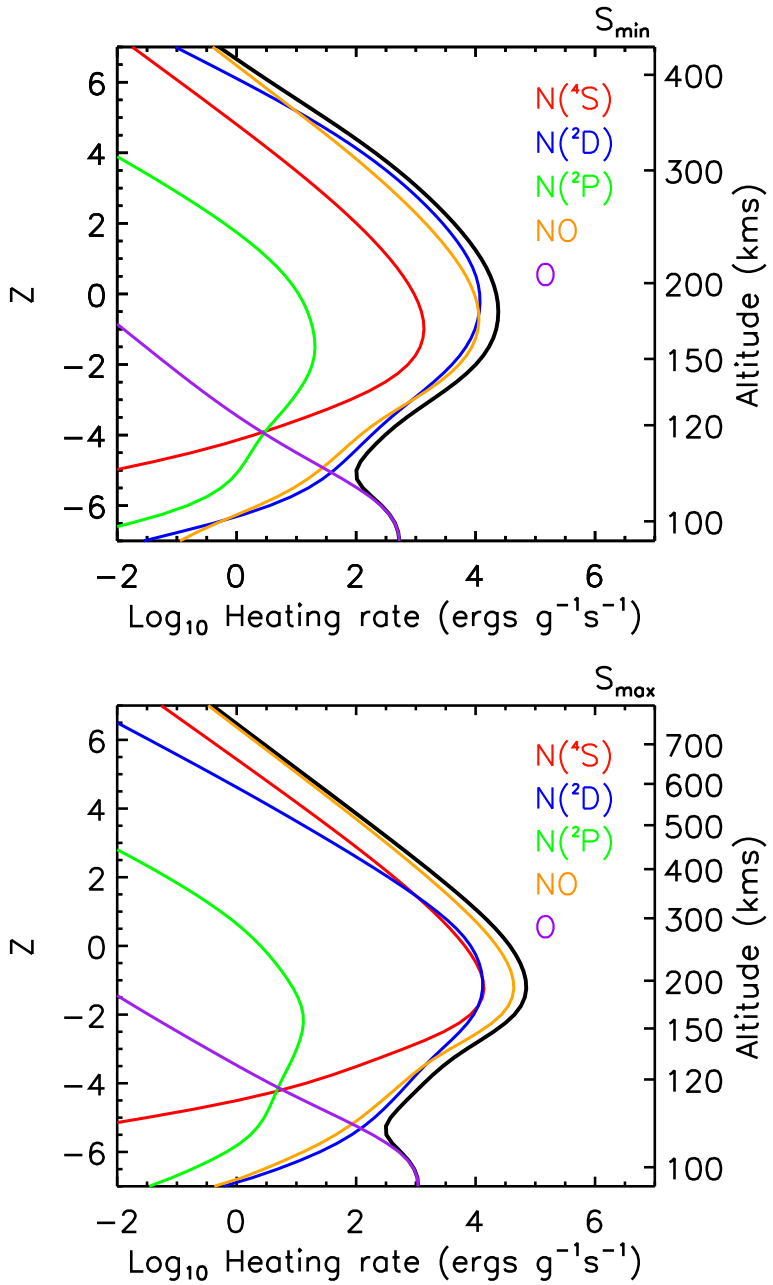

Figure 5.3: Components of the heating rate due to exothermic neutral-neutral reactions for solar minimum ($P = 70$) (top) and solar maximum ($P = 250$) (bottom). Shown are the heating rates due to the reaction of N(^{4}S) with O_2 (red), N(^{2}D) with O_2 (blue), N(^{2}P) with O_2 (green), NO with N(^{4}S) and N(^{2}D) (orange) and O recombination (purple). The above plot does not reflect the effective exothermicity of the N(^{4}S) and N(^{2}D) reactions with O_2, which are reduced due to the chemiluminescence of NO.

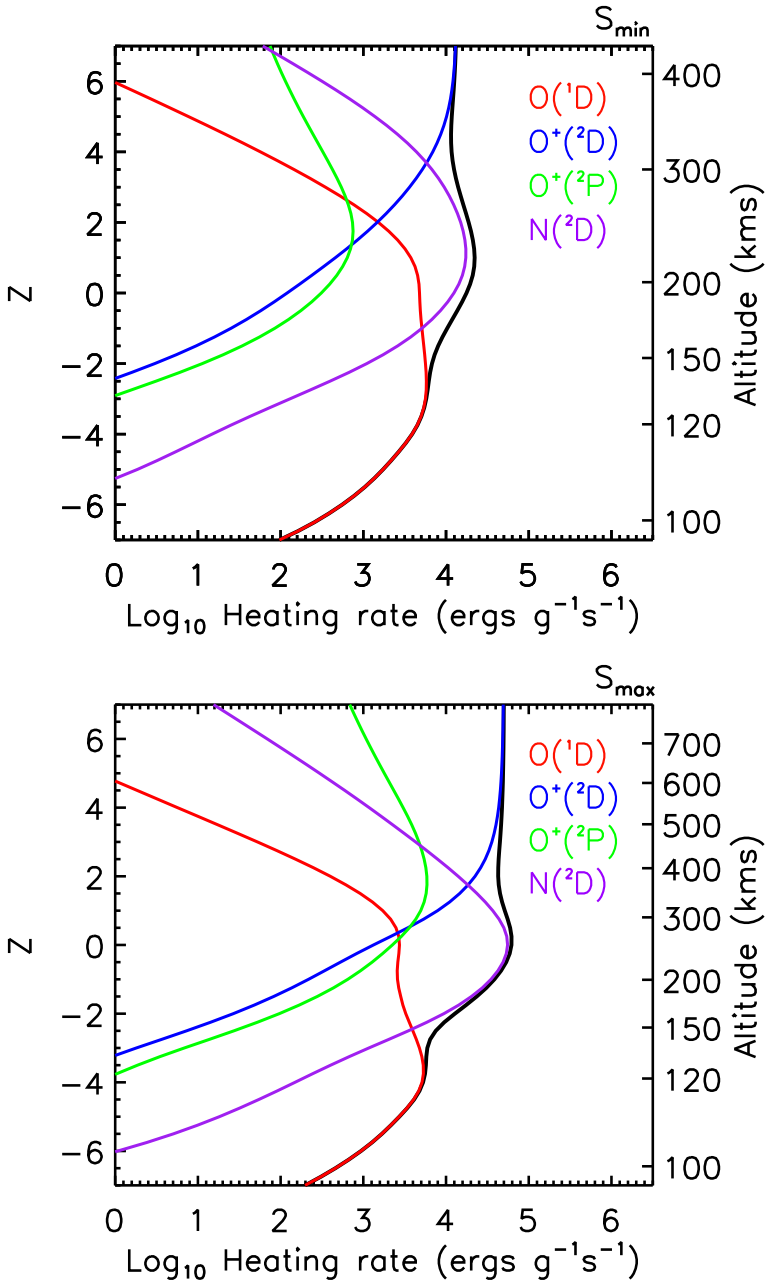

Figure 5.4: Components of the neutral heating rate due to quenching of excited species at solar minimum ($P = 70$) (top) and solar maximum ($P = 250$) (bottom).

this energy is conducted to lower altitudes and it serves as a neutral heating source to below 120 km.

Emissions at 15 µm from CO_2 are the dominant source of radiative cooling below 120 km, while the 63 µm emission from $O(^3P)$ is important above 200 km. At solar minimum, the contribution of the 5.3 µm emission from NO to the net cooling rate smaller that either of the above emissions. However, while the energy loss rates due to CO_2 and $O(^3P)$ are seen to increase by approximately 33% and 12% respectively betwen solar minimum and maximum, the peak cooling rate due to NO increases by nearly an order of magnitude, with the peak emission increasing from 3.2×10^3 ergs g^{-1} s^{-1} to 3×10^4 ergs g^{-1} s^{-1}. This increase results from a combination of increases in the NO densities and the temperature of the thermosphere, and serves to highlight the "thermostat" effect of the 5.3 µm cooling.

Figure 5.5 also shows the contribution of the chemiluminescent emission from nitric oxide to energy loss from the thermosphere. As previously noted in Chapter 2, this emission is not a cooling source in the traditional sense, as it does not convert kinetic energy from the background atmosphere into infrared radiation. Instead, it reduces the effective exothermicities of the reactions that produce nitric oxide in the thermosphere. With this in consideration, it is seen that the energy loss rate due to chemiluminescence has a peak value of 5.3×10^3 ergs g^{-1} s^{-1} at solar minimum and a value of 1.1×10^4 ergs g^{-1} s^{-1} at solar maximum.

A summary of the findings from this section is presented in Table 5.1, where the contribution of various processes to the net heating and cooling have been expressed as percentages for different altitudes at solar minimum and maximum. As molecular conduction (K_T) serves as an energy source near 110 km, we attach a negative sign to its contribution.

5.2.1 Exospheric temperature sensitivities

In order to test the sensitivity of exospheric temperatures to changes in the neutral heating and cooling rates, the ACE1D model was run using associated parameter values that have been previously presented in literature. The results of these tests are shown in Table 5.2, with the percentage change referenced to the default ACE1D run with the parameter values from Chapter 3.

The ACE1D model uses the NO cooling rate given by Caridade et al. (2008) which is in agreement with other values present in literature (Duff and Sharma, 1997; Sharma et al., 1998), but smaller than the value given by Hwang et al. (2003) by a factor of 2. As shown in the previous section, the NO cooling rate increases with NO densities and thermospheric temperatures, and forms a greater fraction of the net cooling rate at solar maximum. Hence, using the Hwang et al. (2003) rate in the model results in a 2.7% decrease in exospheric temperatures from the reference value during solar minimum, but a larger change of 6.2% at solar maximum. The model confirms results from Chapter 2 regarding the role of chemiluminescence in determining thermospheric temperatures. Excluding this process from the

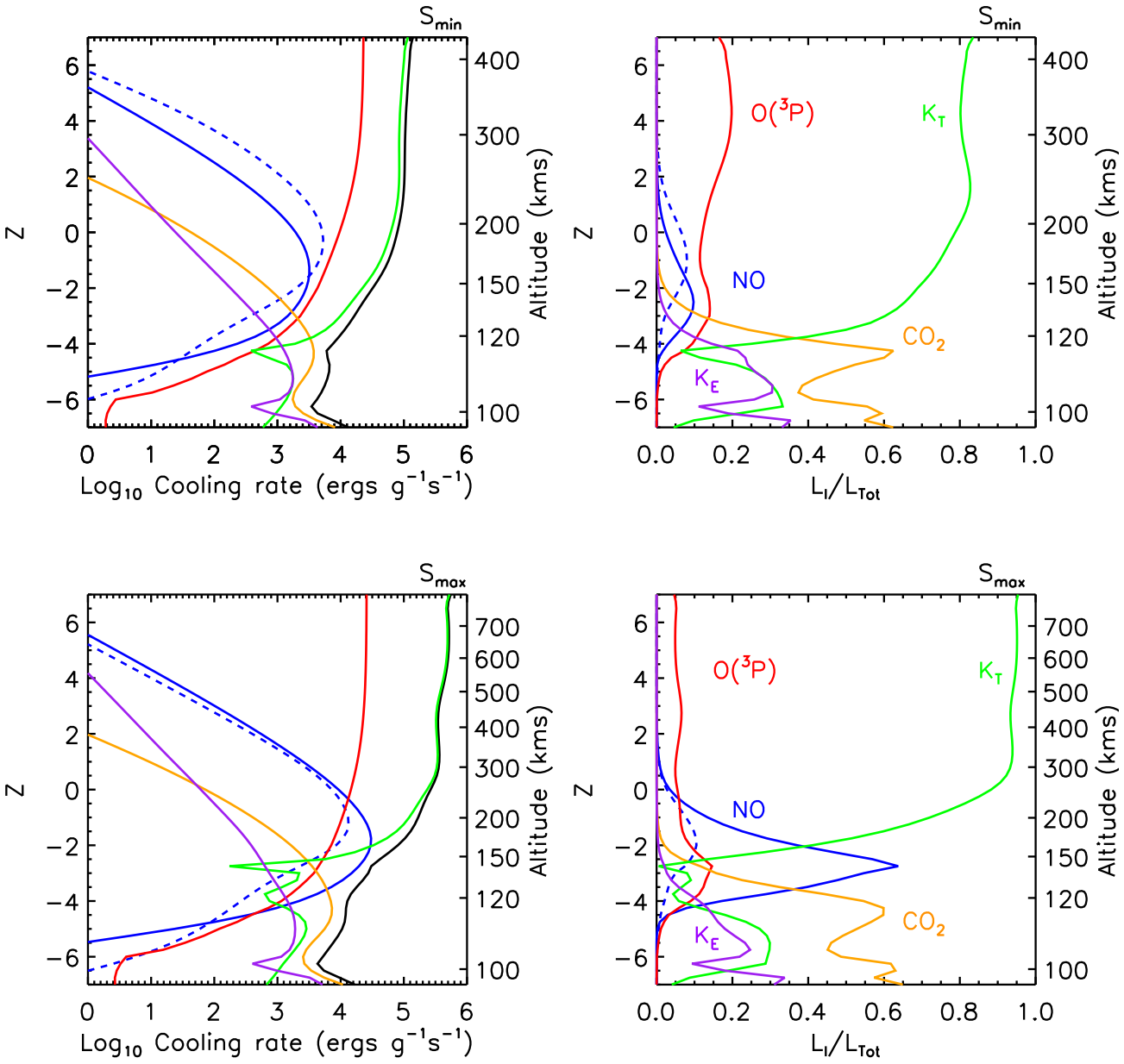

Figure 5.5: ACE1D model calculations of neutral gas cooling rates for solar minimum ($P = 70$) (top) and solar maximum ($P = 250$) (bottom). On the left column are the magnitudes of the cooling rates and on the right column are the fractional contribution of each process. Shown are the net cooling rate (black), heat transport due to thermal conduction (K_T, green) and eddy diffusion (K_E, purple), and the radiative cooling due to CO_2 (orange), NO (blue) and O(^{1}D) (red). The contribution of NO chemiluminescence is denoted by the dashed blue line.

Table 5.1: % Contribution of Heating and Cooling Processes (S_{min}/S_{max})

	Altitude		
	110 km	200 km	300 km
Heating Processes			
EUV absorption	35/30	2/0	0/0
Quenching	56/55	23/23	12/15
Neutral-neutral chemistry	3/8	24/41	0/5
Ion-neutral chemistry	2/3	21/16	11/22
Photoelectron heating	0/1	0/10	9/9
Joule Heating	4/3	14/6	10/12
Election-Ion collisions	0/0	6/4	58/37
Cooling Processes			
CO_2 cooling	52/56	0/0	0/0
NO cooling	0/0	2/14	0/1
NO chemiluminescence	0/0	6/8	0/0
O(^{3}P) cooling	2/2	12/6	19/5
K_T	-21/-24	80/72	81/94
K_E	24/16	0/0	0/0

Table 5.2: Exospheric Temperature Sensitivities

	Solar Min.		**Solar Max.**	
Case	T_{exo} (K)	ΔT_{exo} (%)	T_{exo} (K)	ΔT_{exo} (%)
MSIS	739		1263	
ACE1D (default run)	643		1364	
Doubled NO cooling (thermal)	626	-2.7	1280	-6.2
No Chemiluminescence	665	3.3	1405	3.1
Halved O(^{3}P) cooling	672	4.4	1396	2.3
95 GW Joule Heating	673	4.5	1395	2.3

energy budget calculations results in a 3% increase in modeled exospheric temperatures for both levels of solar activity, which is in line with the results presented in Chapter 2.

The model was also tested by scaling the cooling rate of O(^{3}P) by a factor 2, which was previously done by Roble et al. (1987) in order to account for non-LTE effects. This results in an increase in the exospheric temperature of 4.4% and 2.3% at solar minimum and maximum respectively. As conduction becomes increases in importance in the upper thermosphere as a heat loss mehcnaism with solar activity, it is seen that radiative cooling by O(^{3}P) plays a smaller role.

The model uses a value of 70 GW for the global joule energy input, obtained from Foster et al. (1983). However, a study of long term trends by Knipp et al. (2004) has suggested a mean value of 95 GW for this energy input, a 36% increase from the Foster et al. (1983) value. As the overall contribution of joule input to thermospheric heating decreases with increasing solar activity, using this value results in a 4% increase of the exospheric temperature at solar minimum, and a 2% increase at solar maximum. However, it should be noted that the value presented by Knipp et al. (2004) has a large standard deviation associated with it ($\pm$93 GW), suggesting that the energy input to the model due to this process is better represented as a value that depends on solar activity.

Similar to the tests done in Section 4.6, the contribution of various portions of the solar spectrum to neutral temperatures was also tested in a series of model runs that each omitted one bin of the solar flux specification. Results from these runs are shown in Figure 5.6 along with labels indicating the effect of different portion of the solar spectrum, normalized to the total change in the temperature for all runs. Contrary to the general assumption that the temperature of the thermosphere is largely governed by absorption of solar fluxes at FUV wavelengths, it is seen that fluxes at all wavelengths have a significant effect on the exospheric temperature. In particular, energy deposition at XUV wavelengths contributes indirectly to a number of heating processes and increases in importance at higher levels of solar activity. However, fluxes at these wavelengths have significant variability and large associated uncertainties (Woods et al., 2005; Solomon and Qian, 2005). The model results presented here and in section 4.3 suggest the need for improved measurements of the solar soft x-ray fluxes to better understand its contribution to thermospheric energetics.

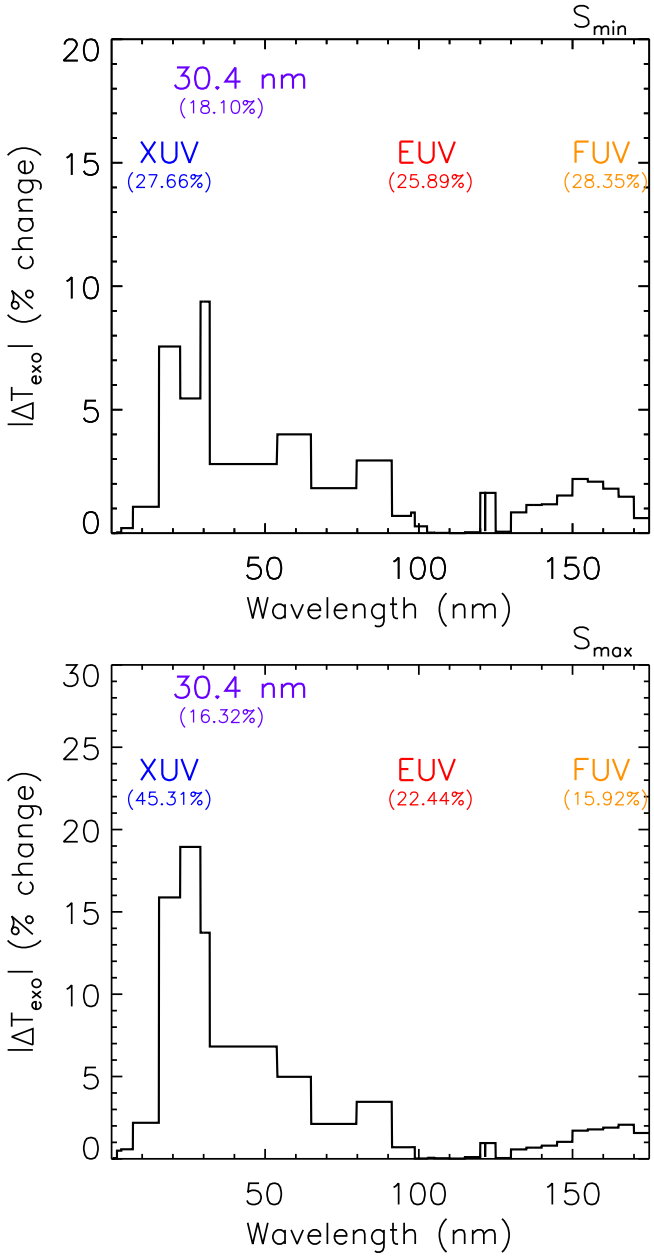

Figure 5.6: Variation in exospheric neutral temperatures as a function of solar irradiance. The labels indicate contributions of different portions of the solar flux specification: soft x-rays (XUV, $0.05 - 29$ nm), the He II line (30.4, $29 - 32$ nm), extreme ultraviolet radiation (EUV, $32 - 105$ nm), and far ultraviolet radiation (FUV, $105 - 175$ nm).

Chapter 6

Conclusions

Chemiluminescence is a secondary source of energy loss from the themosphere, produced as a result of nascent vibrational excitation of nitric oxide in the thermosphere. The present work shows this process to be an important contributor to infrared emissions from the thermosphere, forming 15-40% of the infrared emissions from nitric oxide on the dayside at low to mid latitudes. Using updated results regarding the product channels, vibrational yields and rate coefficients of the reactions involved, we extend the work of Sharma et al. (1998) and Funke and López-Puertas (2000) by including the contribution from the $2 < v \leq 10$ levels. As a mechanism of thermospheric energy loss that is dependent on the production of NO, chemiluminescence is also shown to be a significant source of infrared emissions during periods of increased solar energy deposition.

While the emission serves to reduce the effective heating rate of the N(^{2}D) and N(^{4}S) reactions with O_2, it does not entirely offset the exothermicities of these reactions. The exothermicities of the N(^{2}D) and N(^{4}S) reactions are 3.87 and 1.37 eV respectively, while the average vibrational level excited from the two processes are $v = 6$ and $v = 4$. For the best case scenario when the NO molecule returns to the ground state only by radiative relaxation, chemiluminescence will reduce the heating rate by 35-66%, with the remainder still being converted into thermal energy. This can be seen in Figure 6.1, which plots the efficiency of chemiluminescence (the ratio of the chemiluminescent energy loss rate and the chemical heating rate) as a function of altitude. Below 200 km where the emission is most important, the net efficiency ranges from 20-40% under solar minimum conditions, increasing to 50% for high solar activity due to the increased production of NO from N(^{4}S). As a result, despite it being a significant source of infrared emissions, including chemiluminescence in thermospheric energy budget calculations results in only a 2-3% change in exospheric temperatures.

In order to fully evaluate the importance various processes governing the energetics of the upper atmosphere, a self consistent, one dimensional, thermospheric/ionospheric model that uses updated aeronomic results has also been developed. By accounting for various physical and chemical processes, the Atmospheric Chemistry and Energetics (ACE) 1D model solves

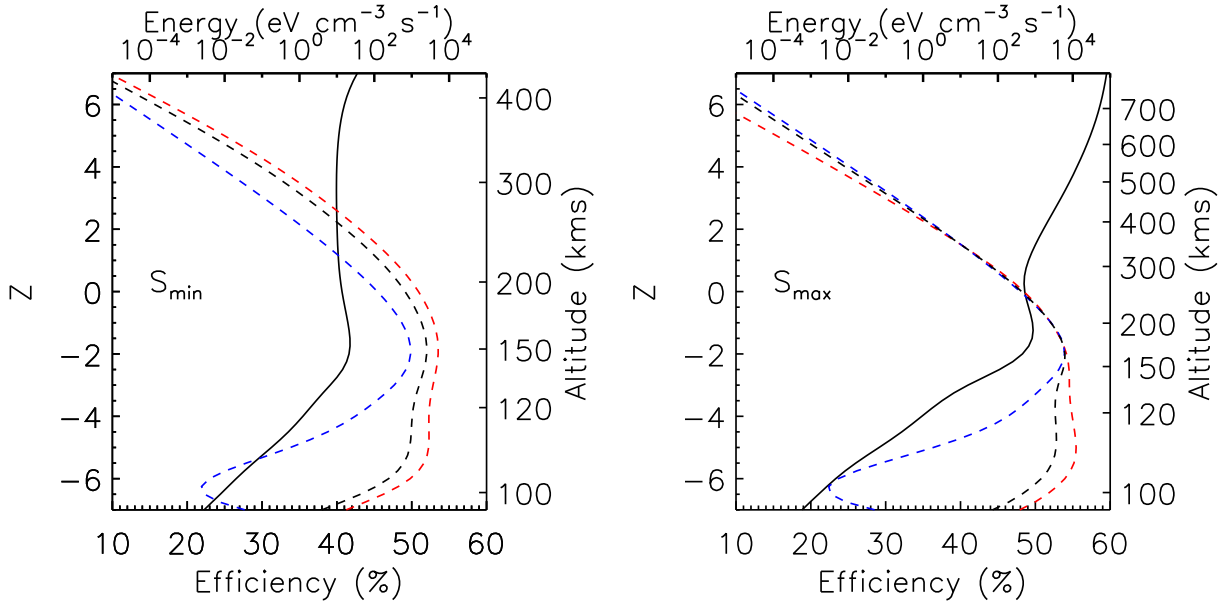

Figure 6.1: The efficiency of chemiluminescence (solid black) in reducing the exothermicity of the N(^{2}D)/N(^{4}S) reactions with O_2, calculated as the ratio of the volume emission rate to the heating rate. Also shown are the heating rates for the N(^{2}D) reaction (red dashed), N(^{4}S) reaction (blue dashed) and the total chemiluminescence (black dashed). The two plots show calculations at solar minimum (left) and solar maximum (right).

a set of continuity and energy equations to produce a global mean representation of the upper atmosphere in terms of the densities and temperatures of various neutral and ion species. The model serves as a useful analytical tool to evaluate the importance of various thermospheric processes and has been used to test the sensitivity of thermospheric quantities to various portions of the solar spectrum.

6.1 Future work

The present work was motivated by the model-data discrepancy regarding the radiative cooling of the thermosphere by nitric oxide. Uncertainties still remain in the cooling rate due to nitric oxide - the most recent experimental result (Hwang et al., 2003) is still a factor of 2 larger than several other theoretical results (Duff and Sharma, 1997; Sharma et al., 1998; Caridade et al., 2008). Current thermospheric models have argued for the larger cooling rate in order to obtain a reasonable thermospheric temperature profile and achieve better agreement with measurements (Lu et al., 2010), or have considered increased cooling from other processes (Sharma and Roble, 2001). While the ACE1D model has shown that a reasonable thermospheric temperature profile can be obtained using the lower bound NO cooling rate and an updated NO chemistry scheme, there is still work to be done in order to improve the agreement with MSIS results. A proposed first step towards this is to drive the model using a solar irradiance model different from the one given in section 3.7, in order to ascertain if the non-linear response of exospheric temperatures seen in MSIS is a shortcoming of the current solar input.

While increased cooling by nitric oxide is known to be the key towards resolving the slow thermospheric recovery of models following geomagnetic storms (Lei et al., 2011; Lu et al., 2014), the chemiluminescent component of the emission has been shown to be incapable of resolving this discrepancy. This suggests that the solution lies in improving the nitric oxide chemistry of thermospheric models.

Appendix A

Model chemistry

Tabulated below are the neutral-neutral and ion-neutral reactions referred to in Figure 3.1, and implemented in the ACE1D model. The tables lists the rate coefficients, relaxation frequencies and exothermicities for each reaction, along with yields for various product channels, and the associated reference from which the values were obtained. T_n, T_i, and T_e refer to the neutral, ion and electron temperatures respectively. The rate coefficients below are in units of $cm^3\ s^{-1}$, except for the three body recombination reactions which are in units of $cm^6\ s^{-1}$, and the photodissociation frequency of NO which has units of s^{-1}. Radiative relaxation frequencies are given in units of s^{-1}, and ionization cross-sections have units of cm^{-2}. β denotes the branching ratio of a given product channel and is dimensionless. Where unavailable, exothermicities have been calculated using the standary enthalpy of formation of the reactants and products.

Table A.1: **Neutral-neutral reactions**

Reaction			Rate coefficient	Notes	Reference
$N(^2P) + O_2$	$\rightarrow$	$NO+O(^3P)$	$3.1\times10^{-12}\ e^{-60/T_n}$		Herron (1999)
$N(^2P) + O(^3P)$	$\rightarrow$	$N(^4S) + O$	2.7×10^{-11}	$\beta = 0.03$	Herron (1999)
	$\rightarrow$	$N(^2D) + O$		$\beta = 0.47$	
	$\rightarrow$	$NO^+ + e$		$\beta = 0.5$	
$N(^2P) + e$	$\rightarrow$	$N(^2D) + e$	9.5×10^{-9} +		Berrington and Burke (1981)
	$\rightarrow$	$N(^4S) + e$	$1.6\times10^{-12}\ T_e^{0.85}$		
$N(^2D) + N_2$	$\rightarrow$	$N(^4S) + N_2$	1.74×10^{-14}		Herron (1999)
$N(^2D) + O_2$	$\rightarrow$	$NO(v) + O(^3P)$	$6.2\times10^{-12}(T_n/300)$		Duff et al. (2003)
$N(^2D) + O$	$\rightarrow$	$N(^4S) + O$	$1.65\times10^{-12}\ e^{-260/T_n}$		Fell et al. (1990)
$N(^2D) + NO$	$\rightarrow$	$N_2 + O(^3P)$	6.7×10^{-11}		Herron (1999)
$N(^2D) + e$	$\rightarrow$	$N(^4S) + e$	$3.86\times10^{-10}\ (T_e/300)^{0.81}$		Berrington and Burke (1981)
$N(^4S) + O_2$	$\rightarrow$	$NO(v) + O(^3P)$	$1.5\times10^{-11}\ e^{-3600/T_n}$		Sander et al. (2006)
$N(^4S) + NO$	$\rightarrow$	$N_2 + O(^3P)$	$2.1\times10^{-11}\ e^{100/T_n}$		Sander et al. (2006)
$O + O + M$	$\rightarrow$	$O_2 + M$	$9.59\times10^{-34}\ e^{480/T_n}$		Logan et al. (1978)
$O + O_2 + M$	$\rightarrow$	$O_3 + M$	$6\times10^{-34}\ (T_n/300)^{-2.4}$		Sander et al. (2006)
$N_2(A) + O$	$\rightarrow$	$NO + N(^2D)$	1×10^{-13}		Dilecce and De Benedictis (1999)
$N(^2P) + N_2$	$\rightarrow$	$N(^4S) + N_2$	5×10^{-17}		Herron (1999)
$N(^2P) + NO$	$\rightarrow$	$N(^4S) + NO$	2.9×10^{-11}		Herron (1999)

A.1 – continued from previous page

Reaction			Rate coefficient	Notes	Reference
$O(^1D) + N_2$	$\rightarrow$	$O(^3P) + N_2$	$2{\times}10^{-11}\ e^{107.8/T_n}$		Fennelly et al. (1994)
$O(^1D) + O_2$	$\rightarrow$	$O(^3P) + O_2$	$2.9{\times}10^{-11}\ e^{67.5/T_n}$		Fennelly et al. (1994)
$O(^1D) + O$	$\rightarrow$	$O(^3P) + O$	$8{\times}10^{-12}$		Fennelly et al. (1994)
$N_2 + h\nu\ /e^*$	$\rightarrow$				
	$\rightarrow$	$2N(^2P, ^2D, ^4S)$			
				$\beta_{N(^2P)} = 0.224$	Yonker (2013)
				$\beta_{N(^2D)} = 0.276$	
				$\beta_{N(^4S)} = 0.5$	
	$\rightarrow$	$N_2^+ + e$			Solomon and Qian (2005)
	$\rightarrow$	$N + N^+ + e$			
$O_2 + h\nu\ /e^*$	$\rightarrow$				
	$\rightarrow$	$O(^1D) + O(^3P)$			Lee et al. (1977),
	$\rightarrow$	$O_2^+ + e$			Solomon and Qian (2005)
	$\rightarrow$	$O + O^+ + e$			
$O + h\nu\ /e^*$	$\rightarrow$	$O^+ + e$			Solomon and Qian (2005)
$N + h\nu\ /e^*$	$\rightarrow$	$N^+ + e$			Solomon and Qian (2005)
$NO + h\nu\ /e^*$	$\rightarrow$	$NO^+ + e$		$\sigma_i = 2.02 \times 10^{-18}$	Watanabe (1958)
	$\rightarrow$	$N(^4S) + O$	$J_{NO} = 4.5 \times 10^{-6}$		Barth (1992)

Table A.2: **Ion-neutral reactions**

Reaction			Rate coefficient	Notes	Reference
$N^+ + NO$	$\rightarrow$	$N(^4S) + NO^+$	$6.5\times10^{-9}(T_i)^{-0.44}$	$\beta = 0.91$	Midey et al. (2004)
		$O + N_2^+$		$\beta = 0.07$	
		$O^+ + N_2$		$\beta = 0.02$	
$N^+ + O(^3P)$	$\rightarrow$	$N(^4S) + O^+$	4.5×10^{-12}		Anicich (2003)
$N^+ + O_2$	$\rightarrow$	$N(^2D) + O_2^+$	5.5×10^{-10}	$\beta = 0.5$	Midey et al. (2006)
	$\rightarrow$	$NO^+ + O$		$\beta = 0.42$	
	$\rightarrow$	$NO + O^+(^4S)$		$\beta = 0.08$	
$N_2^+ + e$	$\rightarrow$	$N(^2D) + N(^2D)$	$2.2\times10^{-7}(300/T_e)^{0.39}$	$\beta = 0.52$	Sheehan and St-Maurice (2004), Peterson et al. (1998)
	$\rightarrow$	$N(^2D) + N(^4S)$		$\beta = 0.37$	
	$\rightarrow$	$N(^2P) + N(^4S)$		$\beta = 0.11$	
$N_2^+ + N(^4S)$	$\rightarrow$	$N^+ + N(^4S)$	1×10^{-11}		Fox and Sung (2001)
$N_2^+ + NO$	$\rightarrow$	$NO^+ + N_2$	$7.5\times10^{-9}(T_i)^{-0.52}$		Midey et al. (2004)
$N_2^+ + O(^3P)$	$\rightarrow$		$1.33\times10^{-10}(300/T_i)^{0.44}$	$T_i \leq 1500$ K	Fox and Sung (2001)
			$6.5\times10^{-11}(T_i/300)^{0.2}$	$T_i > 1500$ K	
	$\rightarrow$	$NO^+ + N(^2D)$		$\beta = 0.9$	
	$\rightarrow$	$NO^+ + N(^4S)$		$\beta = 0.05$	
	$\rightarrow$	$O^+ + N_2$		$\beta = 0.05$	

A.2 – continued from previous page

Reaction			Rate coefficient	Notes	Reference
$N_2^+ + O_2$	$\rightarrow$	$N_2 + O_2^+$	$5.1\times10^{-11}(300/T_i)^{1.16}$	$T_i \leq 1000$ K	Fox and Sung (2001)
			$1.26\times10^{-11}(T_i/1000)^{0.67}$	$T_i > 1000$ K	
$NO^+ + e$	$\rightarrow$	$N(^2D) + O$	$3.5\times10^{-7}(300/T_e)^{0.69}$	$\beta = 0.95$	Sheehan and St-Maurice (2004)
	$\rightarrow$	$N(^4S) + O$		$\beta = 0.05$	Hellberg et al. (2003)
$O^+ + N(^2D)$	$\rightarrow$	$N^+ + O$	1.3×10^{-10}		Richards and Voglozin (2011)
$O^+ + N_2$	$\rightarrow$	$NO^+ + N(^4S)$	$1\times10^{-12}\ (300/T_i)^{0.45}$	$T_i \leq 1000$	Richards and Voglozin (2011)
			$7\times10^{-13}\ (T_i/1000)^{2.12}$	$T_i > 1000$	
$O^+ + NO$	$\rightarrow$	$NO^+ + O$	$5.01\times10^{-13}\ (300/T_i)^{1.68}$		Dotan and Viggiano (1999)
$O^+ + O_2$	$\rightarrow$	$O_2^+ + O$	$1.7\times10^{-11}\ (300/T_i)^{0.77}+$		Hierl et al. (1997)
			$8.54\times10^{-11}\ e^{-3461/T_i}$		
$O^+(^2D) + e$	$\rightarrow$	$O^+(^4S) + e$	$6.03\times10^{-8}(300/T_e)^{0.5}$		Richards and Voglozin (2011)
$O^+(^2D) + N(^4S)$	$\rightarrow$	$N^+ + O$	1.5×10^{-10}		Richards and Voglozin (2011)
$O^+(^2D) + N_2$	$\rightarrow$	$O(^3P) + N_2^+$	$5.7\times10^{-10}\ e^{-400/T_i}$		Fox and Sung (2001)
$O^+(^2D) + NO$	$\rightarrow$	$NO^+ + O$	1.2×10^{-9}		Richards and Voglozin (2011)
$O^+(^2D) + O(^3P)$	$\rightarrow$	$O^+(^4S) + O(^3P)$	1×10^{-11}		Richards and Voglozin (2011)
$O^+(^2D) + O_2$	$\rightarrow$	$O_2^+ + O$	7×10^{-10}		Johnsen and Biondi (1980)
$O^+(^2P) + e$	$\rightarrow$	$O^+(^4S) + e$	$1.84\times10^{-7}(300/T_e)^{0.5}+$		Richards and Voglozin (2011)
	$\rightarrow$	$O^+(^2D) + e$	$3.03\times10^{-8}(300/T_e)^{0.5}$		

A.2 – continued from previous page

Reaction			Rate coefficient	Notes	Reference
$O^+(^2P) + N_2$	$\rightarrow$	$O(^3P) + N_2^+$	$5.7\times10^{-10}\ e^{-400/T_i}$		Fox and Sung (2001)
$O^+(^2P) + O(^3P)$	$\rightarrow$	$O^+(^4S) + O(^3P)$	5×10^{-11}		Stephan et al. (2003)
$O^+(^2P) + O_2$	$\rightarrow$	$O_2^+ + O$	7×10^{-10}		Johnsen and Biondi (1980)
$O_2^+ + e$	$\rightarrow$		$2\times10^{-7}(300/T_e)^{0.7}$	$T_e < 1200$ K	Fennelly et al. (1994)
			$1.6\times10^{-7}(300/T_e)^{0.55}$	$T_e \geq 1200$ K	
	$\rightarrow$	$O(^3P)+O(^3P)$	$\beta = 0.22$		Schunk and Nagy (2009)
	$\rightarrow$	$O(^3P)+O(^1D)$	$\beta = 0.42$		
	$\rightarrow$	$O(^1D)+O(^1D)$	$\beta = 0.36$		
$O_2^+ + N(^2D)$	$\rightarrow$	$NO^+ + O$	1.8×10^{-10}		Richards and Voglozin (2011)
$O_2^+ + N(^2P)$	$\rightarrow$	$O_2^+ + N$	2.2×10^{-11}		Zipf et al. (1980)
$O_2^+ + N(^4S)$	$\rightarrow$	$NO^+ + O$	1.33×10^{-10}		Scott et al. (1998)
$O_2^+ + NO$	$\rightarrow$	$NO^+ + O_2$	4.5×10^{-10}		Midey and Viggiano (1999)

Table A.3: **Loss frequencies and Photon Energies**

Reaction			Loss frequency (s^{-1})	$h\nu$ Energy (eV)	Reference
$N(^2D)$	$\rightarrow$	$N(^4S) + h\nu$	1.279×10^{-5}	2.38	Swaminathan et al. (1998)
$N(^2P)$	$\rightarrow$	$N(^4S) + h\nu$	5.4×10^{-3}	3.57	Swaminathan et al. (1998)

A.3 – continued from previous page

Reaction			Relaxation frequency (s^{-1})	$h\nu$ Energy (eV)	Reference
	$\rightarrow$	$N(^2D) + h\nu$	8.054×10^{-2}	1.19	
$O^+(^2P)$	$\rightarrow$	$O^+(^4S) + h\nu$	0.047	5.02	Roble (1995)
	$\rightarrow$	$O^+(^2D) + h\nu$	0.171	1.69	
$O(^1D)$	$\rightarrow$	$O(^3P) + h\nu$	0.0059	1.97	Fennelly et al. (1994)

Table A.4: **Reaction Exothermicities**

Reaction			Exothermicity (eV)	Reference
$N^+ + NO$	$\rightarrow$	$N(^4S) + NO^+$	5.3	Midey et al. (2004)
		$O + N_2^+$	2.2	
		$O^+ + N_2$	4.2	
$N^+ + O$	$\rightarrow$	$O^+(^4S) + N(^4S)$	0.98	Roble (1995)
$N^+ + O_2$	$\rightarrow$	$N(^2D) + O_2^+$	0.04	Midey et al. (2006)
	$\rightarrow$	$NO^+ + O$	6.7	
	$\rightarrow$	$NO + O^+(^4S)$	2.3	
$N_2^+ + e$	$\rightarrow$	$N(^2D) + N(^2D)$	3.44	Roble (1995)
	$\rightarrow$	$N(^2D) + N(^4S)$	5.82	
	$\rightarrow$	$N(^2P) + N(^4S)$	4.63	

A.4 – continued from previous page

Reaction			Exothermicity (eV)	Reference
$N_2^+ + NO$	$\rightarrow$	$NO^+ + N_2$	6.3	Midey et al. (2004)
$N_2^+ + O$	$\rightarrow$	$NO^+ + N(^2D)$	0.646	Scott et al. (1999)
	$\rightarrow$	$NO^+ + N(^4S)$	3.06	
	$\rightarrow$	$O^+ + N_2$	1.02	
$N_2^+ + O_2$	$\rightarrow$	$O_2^+ + N_2$	3.5	Dotan et al. (1997)
$NO^+ + e$	$\rightarrow$	$N(^2D) + O$	0.38	Roble (1995)
	$\rightarrow$	$N(^4S) + O$	2.75	
$O^+ + N(^2D)$	$\rightarrow$	$N^+ + O$	1.45	Roble (1995)
$O^+ + N_2$	$\rightarrow$	$NO^+ + N(^4S)$	1.09	Roble (1995)
$O^+ + NO$	$\rightarrow$	$NO^+ + O$	4.3	Dotan and Viggiano (1999)
$O^+ + O_2$	$\rightarrow$	$O_2^+ + O$	1.56	Roble (1995)
$O^+(^2D) + e$	$\rightarrow$	$O^+(^4S) + e$	3.31	Roble (1995)
$O^+(^2D) + N_2$	$\rightarrow$	$O(^3P) + N_2^+$	1.35	Roble (1995)
$O^+(^2D) + O(^3P)$	$\rightarrow$	$O^+(^4S) + O(^3P)$	3.31	Stephan et al. (2003)
$O^+(^2D) + O_2$	$\rightarrow$	$O_2^+ + O$	4.865	Roble (1995)
$O^+(^2P) + e$	$\rightarrow$	$O^+(^4S) + e$	5.0	Stephan et al. (2003)
	$\rightarrow$	$O^+(^2D) + e$	1.69	
$O^+(^2P) + O(^3P)$	$\rightarrow$	$O^+(^4S) + O(^3P)$	5.0	Roble (1995)

A.4 – continued from previous page

Reaction			Exothermicity (eV)	Reference
$O^+(^2P) + N_2$	$\rightarrow$	$O(^3P) + N_2^+$	3.05	Li et al. (1997)
$O_2^+ + e$	$\rightarrow$	$O(^3P) + O(^3P)$	6.99	Schunk and Nagy (2009)
	$\rightarrow$	$O(^3P) + O(^1D)$	5.02	
	$\rightarrow$	$O(^1D) + O(^1D)$	3.06	
$O_2^+ + N(^2P)$	$\rightarrow$	$O_2^+ + N$	3.57	Zipf et al. (1980)
$O_2^+ + N(^4S)$	$\rightarrow$	$NO^+ + O$	4.18	Scott et al. (1998)
$O_2^+ + NO$	$\rightarrow$	$NO^+ + O_2$	2.81	Midey and Viggiano (1999)
$N(^4S) + O_2$	$\rightarrow$	$NO(v) + O(^3P)$	1.385	Kennealy et al. (1978)
$N(^4S) + NO$	$\rightarrow$	$N_2 + O(^3P)$	3.25	Baulch et al. (2005)
$N(^2D) + O_2$	$\rightarrow$	$NO(v) + O(^3P)$	3.76	Kennealy et al. (1978)
$N(^2D) + NO$	$\rightarrow$	$N_2 + O(^3P)$	5.63	Roble (1995)
$N(^2P) + O_2$	$\rightarrow$	$NO+O(^3P)$	4.96	Rawlins et al. (1989)
$O + O + M$	$\rightarrow$	$O_2 + M$	5.12	Roble (1995)
$N(^2D) + M$	$\rightarrow$	$N(^4S) + M$	2.38	Roble (1995), Herron (1999)
(M = O, N_2, e)				
$N(^2P) + N_2$	$\rightarrow$	$N(^4S) + N_2$	3.57	Herron (1999), Zipf et al. (1980)
$O(^1D) + M$	$\rightarrow$	$O(^3P) + M$	1.97	Roble (1995)

Appendix B

Ionospheric parameters

The parameters concerning the heating of ionospheric electrons, joule heating of neutral species, heating and cooling terms associated with thermal collisions involving neutrals, electrons and ions, and the diffusion of ions are listed here.

B.1 Photoelectron heating rate of ionospheric electrons

The ACE1D model uses the parameterization provided by Smithtro and Solomon (2008) to obtain the electron heating rate due to energetic photoelectrons, shown in Figure 4.5. In this method, the heating rate is calculated by scaling the photoionization rate due to solar photons between 0-55 and 55-105 nm:

$$Q_{0-55nm} =< \hat{\epsilon} > \sum_i P_i \bar{\epsilon_i} \tag{B.1}$$

$$Q_{55-105nm} =< \hat{\epsilon} > \; P_i \tag{B.2}$$

$$\log_e < \hat{\epsilon} > = \sum_i c_i (\log_e R)^i \tag{B.3}$$

$$R = \frac{n_e}{[N_2] + [O_2] + [O]} \tag{B.4}$$

Where Q denotes the heating rate in units of eV cm^3 s^{-1}, R is the deposition parameter, $< \hat{\epsilon} >$ is the heating efficiency factor and $\bar{\epsilon_i}$ is the photon energy associated with the bin that produces a local photoionization rate of P_i. The summation for $Q_{0-55\text{nm}}$ is over all wavelength bins. The coefficients for the polynomial fit c_i are given in Table B.1.

Table B.1: Fit parameters for photoelectron heating

	0 - 55 nm	55 - 105 nm
c0	1.468	1.020
c1	9.229×10^{-1}	1.540×10^{-2}
c2	4.956×10^{-2}	-6.858×10^{-3}
c3	-1.897×10^{-2}	-8.528×10^{-3}
c4	-3.934×10^{-3}	-2.052×10^{-3}
c5	-2.643×10^{-4}	-1.634×10^{-4}
c6	-5.980×10^{-6}	-4.314×10^{-6}

The total electron volume heating rate is simply the sum of the individual heating rates:

$$Q = Q_{0-55\text{nm}} + Q_{55-105\text{nm}} \tag{B.5}$$

B.2 Electron cooling rates

Elastic and inelastic collisions of electrons with background neutral species is the dominant energy loss mechanism for electrons in the thermosphere, expressions for which are given here in units of eV cm^{-3} s^{-1}. n_e and n(M) in the below expressions refer to the electron density and the density of species M respectively.

B.2.1 N_2 rotation

$$L_e(N_2) = 3.5 \times 10^{-14}\ n_e n(N_2)(T_e - T_n)/T_e^{0.5} \tag{B.6}$$

B.2.2 O_2 rotation

$$L_e(O_2) = 5.2 \times 10^{-15}\ n_e n(O_2)(T_e - T_n)/T_e^{0.5} \tag{B.7}$$

B.2.3 CO_2 rotation

$$L_e(CO_2) = 5.8 \times 10^{-14}\ n_e n(CO_2)(T_e - T_n)/T_e^{0.5} \tag{B.8}$$

B.2.4 N_2 vibration

$$\begin{aligned} L_e(N_2) &= n_e n(N_2)[1-\exp(-E_1/T_{vib})] \times \sum_{v=1}^{10} Q_{0v}[1-\exp[vE_1(T_e^{-1}-T_{vib}^{-1})]] \\ &+ n_e n(N_2)[1-\exp(-E_1/T_{vib})]\exp(-E_1/T_{vib}) \\ &\times \sum_{v=2}^{9} Q_{1v}[1-\exp[(v-1)E_1(T_e^{-1}-T_{vib}^{-1})]] \end{aligned} \tag{B.9}$$

where E_1 = 3353 K (0.2889 eV), $T_{vib} = T_n$, and

$$\begin{aligned} \log Q_{0v} &= A_{0v} + B_{0v}T_e + C_{0v}T_e^2 + D_{0v}T_e^3 + F_{0v}T_e^4 - 16 \\ \log Q_{1v} &= A_{1v} + B_{1v}T_e + C_{1v}T_e^2 + D_{1v}T_e^3 + F_{1v}T_e^4 - 16 \end{aligned} \tag{B.10}$$

The coefficients A-F in the above expressions have been given in Table B.2, B.3 and B.4

Table B.2: Coefficients for calculating Q_{0v} for $1500 \leq T_e \leq 6000$ K

v	A_{0v}	B_{0v} K^{-1}	C_{0v} K^{-2}	D_{0v} K^{-3}	F_{0v} K^{-4}	δ_{0v}
1	2.025	8.782 $\times 10^{-4}$	2.954 $\times 10^{-7}$	-9.562 $\times 10^{-11}$	7.252 $\times 10^{-15}$	0.06
2	-7.066	1.001 $\times 10^{-2}$	-3.066 $\times 10^{-6}$	4.436 $\times 10^{-10}$	-2.449 $\times 10^{-14}$	0.08
3	-8.211	1.092 $\times 10^{-2}$	-3.369 $\times 10^{-6}$	4.891 $\times 10^{-10}$	-2.706 $\times 10^{-14}$	0.10
4	-9.713	1.204 $\times 10^{-2}$	-3.732 $\times 10^{-6}$	5.431 $\times 10^{-10}$	-3.008 $\times 10^{-14}$	0.10
5	-10.353	1.243 $\times 10^{-2}$	-3.850 $\times 10^{-6}$	5.600 $\times 10^{-10}$	-3.100 $\times 10^{-14}$	0.13
6	-10.819	1.244 $\times 10^{-2}$	-3.771 $\times 10^{-6}$	5.385 $\times 10^{-10}$	-2.936 $\times 10^{-14}$	0.15
7	-10.183	1.185 $\times 10^{-2}$	-3.570 $\times 10^{-6}$	5.086 $\times 10^{-10}$	-2.769 $\times 10^{-14}$	0.15
8	-12.698	1.309 $\times 10^{-2}$	-3.952 $\times 10^{-6}$	5.636 $\times 10^{-10}$	-3.071 $\times 10^{-14}$	0.15
9	-14.710	1.409 $\times 10^{-2}$	-4.249 $\times 10^{-6}$	6.058 $\times 10^{-10}$	-3.300 $\times 10^{-14}$	0.15
10	-17.538	1.600 $\times 10^{-2}$	-4.916 $\times 10^{-6}$	7.128 $\times 10^{-10}$	-3.941 $\times 10^{-14}$	0.15

B.2.5 O_2 vibration

$$L_e(O_2) = n_e\ n(N_2)\ Q(T_e)[1-\exp[2239(T_e^{-1}-T_n^{-1})]] \tag{B.11}$$

Table B.3: Coefficients for calculating Q_{0v} for $300 \leq T_e \leq 1500$ K

v	A_{0v}	B_{0v} K^{-1}	C_{0v} K^{-2}	D_{0v} K^{-3}	F_{0v} K^{-4}	δ_{0v}
1	-6.462	3.151 $\times 10^{-2}$	-4.075 $\times 10^{-5}$	2.439 $\times 10^{-8}$	-5.479 $\times 10^{-12}$	0.14

Table B.4: Coefficients for calculating Q_{1v} for $1500 \leq T_e \leq 6000$ K

v	A_{0v}	B_{0v} K^{-1}	C_{0v} K^{-2}	D_{0v} K^{-3}	F_{0v} K^{-4}	δ_{0v}
2	-3.413	7.326 $\times 10^{-3}$	-2.200 $\times 10^{-6}$	3.128 $\times 10^{-10}$	-1.702 $\times 10^{-14}$	0.11
3	-4.160	7.803 $\times 10^{-3}$	-2.352 $\times 10^{-6}$	3.352 $\times 10^{-10}$	-1.828 $\times 10^{-14}$	0.11
4	-5.193	8.360 $\times 10^{-3}$	-2.526 $\times 10^{-6}$	3.606 $\times 10^{-10}$	-1.968 $\times 10^{-14}$	0.12
5	-5.939	8.807 $\times 10^{-3}$	-2.669 $\times 10^{-6}$	3.806 $\times 10^{-10}$	-2.073 $\times 10^{-14}$	0.08
6	-8.261	1.010 $\times 10^{-2}$	-3.039 $\times 10^{-6}$	4.318 $\times 10^{-10}$	-2.347 $\times 10^{-14}$	0.10
7	-8.185	1.010 $\times 10^{-2}$	-3.039 $\times 10^{-6}$	4.318 $\times 10^{-10}$	-2.347 $\times 10^{-14}$	0.12
8	-10.823	1.199 $\times 10^{-2}$	-3.620 $\times 10^{-6}$	5.159 $\times 10^{-10}$	-2.810 $\times 10^{-14}$	0.09
9	-11.273	1.283 $\times 10^{-2}$	-3.879 $\times 10^{-6}$	5.534 $\times 10^{-10}$	-3.016 $\times 10^{-14}$	0.09

with

$$\begin{aligned}\log_{10}[Q(T_e)] = &-19.9171 + 0.0267\ T_e - 3.9960 \times 10^{-5}\ T_e^2 + 3.5187 \times 10^{-8}\ T_e^3 \\ &- 1.9228 \times 10^{-11}\ T_e^4 + 6.6865 \times 10^{-15}\ T_e^5 - 1.4791 \times 10^{-18}\ T_e^6 \\ &+ 2.0127 \times 10^{-22}\ T_e^7 - 1.5346 \times 10^{-26}\ T_e^8 + 5.0148 \times 10^{-31}\ T_e^9\end{aligned} \tag{B.12}$$

B.2.6 O fine structure

$$\begin{aligned}L_e(O) = n_e\ n(O) D^{-1} \Big(&S_{10}[1 - \exp[98.9(T_e^{-1} - T_n^{-1})]] \Big) + \\ &S_{20} \Big(1 - \exp[326.6(T_e^{-1} - T_n^{-1})] \Big) + \\ &S_{22} \Big(1 - \exp[227.7(T_e^{-1} - T_n^{-1})] \Big)\end{aligned} \tag{B.13}$$

with

$$
\begin{aligned}
D &= 5 + \exp(-326.6\ T_n^{-1}) + 3\exp(-227.7\ T_n^{-1}), \\
S_{21} &= 1.863 \times 10^{-11} \\
S_{20} &= 1.191 \times 10^{-11} \\
S_{10} &= 8.249 \times 10^{-16}\ T_e^{0.6} \exp(-227.7\ T_n^{-1})
\end{aligned}
\tag{B.14}
$$

B.2.7 O(^{1}D) excitation)

$$
\begin{aligned}
L_e(O(^1D)) &= 1.57 \times 10^{-12}\, n_e\, n(O) \exp\left(d\frac{T_e - 3000}{3000\, T_e}\right)\left[exp\left(-22713\frac{T_e - T_n}{T_e\, T_n}\right) - 1\right] \\
d &= 2.4 \times 10^4 + 0.3(T_e - 1500) - 1.947 \times 10^{-5}(T_e - 1500)(T_e - 4000)
\end{aligned}
\tag{B.15}
$$

B.3 Ion cooling rates

Ions are cooled primarily by collisional energy exchange with neutral species, the rates for which are given in Table B.5.

Table B.5: Energy loss rates for ions due to collisions with neutrals

Ion Mixture	Energy Loss rate (10^{-14} eV cm^{-3} s^{-1})
O^+-N_2	6.6 n(O^+) n(N_2) (T_i - T_n)
O^+-O_2	5.8 n(O^+) n(O_2) (T_i - T_n)
O^+-O	0.21 n(O^+) n(O) (T_i + T_n)$^{0.5}$ (T_i - T_n)
NO^+-N_2	5.916 n(NO^+) n(N_2) (T_i - T_n)
NO^+-O_2	5.45 n(NO^+) n(O_2) (T_i - T_n)
NO^+-O	4.5n(NO^+) n(O) (T_i - T_n)
O_2^+-N_2	5.807 n(O_2^+) n(N_2) (T_i - T_n)
O_2^+-O_2	0.14 n(O_2^+) n(O_2) (T_i + T_n)$^{0.5}$ (T_i - T_n)
O_2^+-O	4.358 n(O_2^+) n(O) (T_i - T_n)

B.4 Calculating Joule heating energy input

B.4.1 Pedersen Conductivity

The expression for the Pedersen conductivity due to ions and electrons is given as:

$$\sigma_P = \sum_i \sigma_i \frac{\nu_i}{\nu_i^2 + \omega_i^2} + \sigma_e \frac{\nu_e}{\nu_e^2 + \omega_e^2} \tag{B.16}$$

where ν_i, ω_i, ν_e and ω_e are the ion and electron collision and cyclotron frequencies respectively, defined as

$$\nu_i = \sum_n \nu_{in}, \qquad \nu_{in} = C_{in}\ n_n \tag{B.17}$$

$$\nu_e = \sum_n \nu_{en} \tag{B.18}$$

$$\omega_i = \frac{q_i\ B}{m_i}, \qquad \omega_e = \frac{q_e\ B}{m_e} \tag{B.19}$$

C_{in} are numerical coefficients that define non-resonant ion-neutral interactions. These have been given in Table B.6, while the expressions for resonant collision frequencies for ions are given in Table B.7. Table B.8 lists expressions for collision frequencies for electron - neutral interactions. Finally, the electron and ion conductivities are given as:

$$\sigma_e = \frac{n_e\ q_e^2}{m_e\ \nu_e}, \qquad \sigma_i = \frac{n_i\ q_i^2}{m_i\ \nu_i} \tag{B.20}$$

Table B.6: Collision frequencies ($C_{in} \times 10^{10}$) for nonresonant ion-neutral interactions

	N	O	N_2	O_2
N^+	-	4.42	7.47	7.25
O^+	4.62	-	6.82	6.64
N_2^+	2.95	2.58	-	4.49
O_2^+	2.64	2.31	4.13	-

Table B.7: Collision frequencies for resonant ion-neutral interactions. Densities are in cm^{-3}

Species	T_r (K)	ν^{-1} (s^{-1})
N^+, N	> 275	$3.83 \times 10^{-11}\ n(N)\ T_r^{0.5}\ (1 - 0.063 \log_{10} T_r)^2$
O^+, O	> 235	$3.67 \times 10^{-11}\ n(O)\ T_r^{0.5}\ (1 - 0.064 \log_{10} T_r)^2$
N_2^+, N_2	> 170	$5.14 \times 10^{-11}\ n(N_2)\ T_r^{0.5}\ (1 - 0.069 \log_{10} T_r)^2$
O_2^+, O_2	> 800	$2.59 \times 10^{-11}\ n(O_2)\ T_r^{0.5}\ (1 - 0.073 \log_{10} T_r)^2$

Table B.8: Collision frequencies for electron-neutral interactions. Densities are in cm^{-3}

Species	ν^{-1} (s^{-1})
N_2	$2.33 \times 10^{-11}\ n(N_2)\ (1 - 1.21 \times 10^{-4}\ T_e)\ T_e$
O_2	$1.82 \times 10^{-10}\ n(O_2)\ (1 + 3.6 \times 10^{-2}\ T_e^{0.5})\ T_e^{0.5}$
O	$8.9 \times 10^{-11}\ n(O)\ (1 + 5.7 \times 10^{-4} T_e) T_e^{0.5}$

B.5 Momentum transfer cross sections

The velocity averaged momentum cross sections that are used in expression 3.24 to calculate electron thermal conductivity are given in units of cm^{-2} below:

$$\bar{Q_{D,N_2}} = 2.82 \times 10^{-17}\ T_e^{1/2} - 3.41 \times 10^{-21} T_e^{3/2} \tag{B.21}$$

$$\bar{Q_{D,O_2}} = 2.2 \times 10^{-18}\ T_e^{1/2} + 7.92 \times 10^{-18} T_e^{1/2} \tag{B.22}$$

$$\bar{Q_{D,O}} = 3.4 \times 10^{-16} \tag{B.23}$$

B.6 Ambipolar diffusion coefficients

Expressions for the major and minor ion diffusion coefficients have been obtained from Schunk and Nagy (2009). For O^+, the diffusion parameters are given as:

$$D_a = \frac{2\ kT_p}{m_i\ \nu_i} \tag{B.24}$$

where

$$T_p = \frac{T_e + T_i}{2} \tag{B.25}$$

and ν_i is the ion collision frequency (B.4). Similarly, for N^+

$$D_a = \frac{kT_i}{m_i\ \nu_i} \tag{B.26}$$

The plasma scale height used in Eq. 3.15 is defined as

$$H_p = \frac{2\ kT_p}{m_i\ g} \tag{B.27}$$

Appendix C

Model Solar Fluxes

The ACE1D model follows the solar flux specification implemented in the TIE-GCM, after Solomon and Qian (2005). Given below are the wavelength ranges for each bin along with the corresponding values for the reference solar flux and the scaling parameter A. Details regarding the structure of the wavelength bins and calculation of the solar fluxes have been given 3.7.

Table C.1: **Solar Spectrum Parameters**

Bin #	Wavelength Range (Å)	Reference Value (x10^9 ph cm^{-2} s^{-1})	A-factor
1	0.5-4	5.010E-8	6.24E-1
2	4-8	1.000E-5	3.710E-1
3	8-18	2.000E-3	2.000E-1
4	18-32	2.850E-2	6.247E-2
5	32-70	5.326E-1	1.343E-2
6	70-155	1.270E+0	9.182E-3
7	155-224	5.612E+0	1.433E-2
8	224-290	4.342E+0	2.575E-2
9	290-320	8.380E+0	7.059E-3
10	320-540	2.861E+0	1.458E-2

C.1 – continued from previous page

Bin #	Wavelength Range (Å)	Reference Value (x10^9 ph cm^{-2} s^{-1})	A-factor
11	540-650	4.830E+0	5.857E-3
12	650-798	1.459E+0	5.719E-3
13	650-798	1.142E+0	3.680E-3
14	798-913	2.364E+0	5.310E-3
15	798-913	3.655E+0	5.261E-3
16	798-913	8.448E-1	5.437E-3
17	913-975	3.818E-1	4.915E-3
18	913-975	1.028E+0	4.955E-3
19	913-975	7.156E-1	4.422E-3
20	975-987	4.482E+0	3.950E-3
21	987-1027	4.419E+0	5.021E-3
22	1027-1050	4.235E+0	4.825E-3
23	1050-1100	3.298E+0	3.007E-3
24	1100-1150	3.200E+0	2.099E-3
25	1150-1200	8.399E+0	2.541E-3
26	1215.67	3.940E+2	4.230E-3
27	1200-1250	1.509E+1	3.739E-3
28	1250-1300	7.790E+0	2.610E-3
29	1300-1350	2.659E+1	2.877E-3
30	1350-1400	1.387E+1	2.632E-3
31	1400-1450	1.824E+1	1.873E-3
32	1450-1500	2.802E+1	1.202E-3
33	1500-1550	5.080E+1	1.531E-3
34	1550-1600	7.260E+1	1.125E-3

C.1 – continued from previous page

Bin #	Wavelength Range (Å)	Reference Value (x10^9 ph cm^{-2} s^{-1})	A-factor
35	1600-1650	1.055E+2	1.043E-3
36	1650-1700	1.998E+2	6.089E-4
37	1700-1750	3.397E+2	5.937E-4

Appendix D

Numerical methods

The ACE1D model employs centered spatial derivatives and forward time derivatives to discretize and solve the continuity and energy equations discussed in Chapter 3. For the continuity equation, these take the form:

$$\frac{\partial \psi}{\partial Z} = \frac{\psi_{i+1}^{j+1} - \psi_{i-1}^{j+1}}{2\Delta Z} \tag{D.1}$$

$$\frac{\partial^2 \psi}{\partial Z^2} = \frac{\psi_{i+1}^{j+1} - 2\ \psi_{i+1}^{j} + \psi_{i+1}^{j+1}}{\Delta Z^2} \tag{D.2}$$

$$\frac{\partial \psi}{\partial t} = \frac{\psi_{i}^{j+1} - \psi_{i}^{j}}{\Delta t} \tag{D.3}$$

Where the derivatives are evaluated at the grid point i and are used to solve for quantities at the timestep $j+1$. The equation then reduces to an expression in terms of the unknowns ψ_{i-1}^{j+1}, ψ_{i}^{j+1} and ψ_{i+1}^{j+1} with the general form:

$$p_i \psi_{i-1}^{j+1} + q_i \psi_{i}^{j+1} + r_i \psi_{i+1}^{j+1} = l_i \tag{D.4}$$

where p_i, q_i, r_i and l_i are known coefficients. Written for all grid points, this leads to the system of equations

$$\begin{bmatrix} q_1 & r_1 & 0 & 0 & \cdots & 0 \\ p_2 & q_2 & r_2 & 0 & \cdots & 0 \\ 0 & p_3 & q_3 & r_3 & \cdots & 0 \\ \vdots & \vdots & \vdots & \vdots & \vdots & \vdots \\ 0 & \cdots & 0 & 0 & p_n & q_n \end{bmatrix} \times \begin{bmatrix} \psi_1^{j+1} \\ \psi_2^{j+1} \\ \psi_3^{j+1} \\ \vdots \\ \psi_n^{j+1} \end{bmatrix} = \begin{bmatrix} l_1 \\ l_2 \\ l_3 \\ \vdots \\ l_n \end{bmatrix} \tag{D.5}$$

which can then evaluated using tridiagonal matrix algorithms. Using boundary conditions and equations D.1 and D.2, grid points that fall outside of the model boundaries (e.g, $\psi_0^{j+1}, \psi_{n+1}^{j+1}$) are expressed in terms of quantities that are solved for in equation D.4.

D.1 Block Tri-diagonal solver

In solving for the mass mixing ratios of the major species (Eq. 3.3), we solve for the coupled vector $\boldsymbol{\Psi} = [\psi_{O_2}, \psi_O]^T$, in which case the coefficients and variables in D.4 are matrices of dimensions 2×2 and 2×1 respectively. To solve for the vector $\boldsymbol{\Psi}$, we use the block tridiagonal algorithm:

Forward elimination :

$$\begin{aligned} \boldsymbol{H_1} &= \boldsymbol{Q_1^{-1}R_1} \\ \boldsymbol{H_i} &= -\left[\boldsymbol{Q_i} + \boldsymbol{P_iH_{i-1}}\right]^{\boldsymbol{-1}}\boldsymbol{R_i} \qquad (i = 2, 3, ..n) \\ \boldsymbol{g_1} &= \boldsymbol{Q_1^{-1}L_1} \\ \boldsymbol{g_i} &= \left[\boldsymbol{Q_i} + \boldsymbol{P_iH_{i-1}}\right]^{-1}(\boldsymbol{L_i} - \boldsymbol{P_ig_{i-1}}) \qquad (i = 2, 3, ..n) \end{aligned} \tag{D.6}$$

Backward substitution :

$$\begin{aligned} \boldsymbol{\Psi_n} &= \boldsymbol{g_n} \\ \boldsymbol{\Psi_i} &= \boldsymbol{g_i} + \boldsymbol{H_i\Psi_{i+1}} \qquad (i = n-1, ...2, 1) \end{aligned} \tag{D.7}$$

where the unknown variables and the coefficients of D.5 are replaced by vectors and matrices denoted by $\boldsymbol{\Psi_i}$, $\boldsymbol{P_i}$, $\boldsymbol{Q_i}$, $\boldsymbol{R_i}$, and $\boldsymbol{L_i}$.

D.2 Neutral gas cooling rates

The energy loss from the thermosphere due to radiative cooling by NO, CO_2 and O(^{3}P) are temperature dependent, and results in the neutral gas heat equation (Eq. 3.20) being non-linear. Solving this equation thus requires linearization of these terms, which are of the general form:

$$L = a\ e^{-b/T} \tag{D.8}$$

Where T refers to the neutral temperature. Applying a Taylor series expansion to the above expression about the temperature at the current time step and ignoring the second order

and higher terms, we obtain:

$$L = a\ e^{-b/T_n} + a\ e^{-b/T_n}\Big(\frac{-b}{T_n^2}\Big)(T_{n+1} - T_n) \tag{D.9}$$

where T_n and T_{n+1} refer to the neutral temperature at the current and next time step respectively. Grouping terms:

$$\begin{aligned} L &= \Big[a\ e^{-b/T_n}\Big(1 - \frac{b}{T_n}\Big)\Big] + \Big[- \frac{a\ b}{T_n^2} e^{-b/T_n}\ T_{n+1}\Big] \\ &= L_1 + L_2 \end{aligned} \tag{D.10}$$

Here, L_1 comprises of known values, while L_2 is in terms of the unknown quantity T_{n+1} that we wish to solve for. As a result, in the energy equation equivalent of D.4, L_1 is absorbed into the coefficient l_i and can be referred to as the 'explicit' cooling term, while L_2 is a part of the coefficient q_i and is referred to as an 'implicit' cooling term.

Bibliography

Ahmadjian, M., Nadile, R., Wise, J., and Bartschi, B. (1990). Cirris-1a space shuttle experiment. *Journal of Spacecraft and Rockets*, 27(6):669–674.

Anicich, V. G. (2003). An index of the literature for bimolecular gas phase cation-molecule reaction kinetics.

Bailey, S. M., Barth, C. A., and Solomon, S. C. (2002). A model of nitric oxide in the lower thermosphere. *Journal of Geophysical Research: Space Physics*, 107(A8).

Balakrishnan, N., Sergueeva, E., Kharchenko, V., and Dalgarno, A. (2000). Kinetics and thermalization of hot n (4 s) atoms in the upper atmosphere. *Journal of Geophysical Research: Space Physics*, 105(A8):18549–18555.

Ballard, J., Kerridge, B., Morris, P., and Taylor, F. (1993). Observations of v= 1–0 emission from thermospheric nitric oxide by isams. *Geophysical research letters*, 20(12):1311–1314.

Banks, P. and Kockarts, G. (1973). Aeronomy, academic. *New York*.

Barth, C., Lu, G., and Roble, R. (2009). Joule heating and nitric oxide in the thermosphere. *Journal of Geophysical Research: Space Physics*, 114(A5).

Barth, C., Mankoff, K., Bailey, S., and Solomon, S. (2003). Global observations of nitric oxide in the thermosphere. *Journal of Geophysical Research: Space Physics*, 108(A1).

Barth, C. A. (1964). Rocket measurement of the nitric oxide dayglow. *Journal of Geophysical Research*, 69(15):3301–3303.

Barth, C. A. (1966). Rocket measurement of nitric oxide in the upper atmosphere. *Planetary and Space Science*, 14(7):623–630.

Barth, C. A. (1992). Nitric oxide in the lower thermosphere. *Planetary and space science*, 40(2-3):315–336.

Barth, C. A., Rusch, D. W., and Stewart, A. I. (1973). The uv nitric-oxide experiment for atmosphere explorer. *Radio Science*, 8(4):379–385.

Bates, D. (1951). The temperature of the upper atmosphere. *Proceedings of the Physical Society. Section B*, 64(9):805.

Baulch, D., Bowman, C. T., Cobos, C., Cox, R., Just, T., Kerr, J., Pilling, M., Stocker, D., Troe, J., Tsang, W., et al. (2005). Evaluated kinetic data for combustion modeling: supplement ii. *Journal of physical and chemical reference data*, 34(3):757–1397.

Berrington, K. and Burke, P. (1981). Effective collision strengths for forbidden transitions in en and eo scattering. *Planetary and Space Science*, 29(3):377–381.

Billingsley, F. P. (1975). Multiconfiguration self-consistent-field calculation of the dipole moment function and potential curve of no (x 2π). *The Journal of Chemical Physics*, 62(3):864–874.

Braunstein, M. and Duff, J. (2000). Theoretical study of the n (2 d)+ o 2 (x 3 σ g-) o+ no reaction. *The Journal of Chemical Physics*, 113(17):7406–7413.

Caledonia, G., Krech, R., Oakes, D., Lipson, S., and Blumberg, W. (2000). Products of the reaction of 8 km/s n (4s) and o2. *Journal of Geophysical Research: Space Physics*, 105(A6):12833–12837.

Caridade, P., Mota, V., Mohallem, J., and Varandas, A. (2008). A theoretical study of rate coefficients for the o+ no vibrational relaxation. *The Journal of Physical Chemistry A*, 112(5):960–965.

Castle, K. J., Black, L. A., Simione, M. W., and Dodd, J. A. (2012). Vibrational relaxation of co2 (ν2) by o (3p) in the 142–490 k temperature range. *Journal of Geophysical Research: Space Physics*, 117(A4).

Chamberlin, P. C., Woods, T. N., and Eparvier, F. G. (2007). Flare irradiance spectral model (fism): Daily component algorithms and results. *Space Weather*, 5(7).

Chamberlin, P. C., Woods, T. N., and Eparvier, F. G. (2008). Flare irradiance spectral model (fism): Flare component algorithms and results. *Space Weather*, 6(5).

Colegrove, F., Johnson, F., and Hanson, W. (1966). Atmospheric composition in the lower thermosphere. *Journal of Geophysical Research*, 71(9):2227–2236.

DeMajistre, R., Yee, J.-H., and Zhu, X. (2001). Parameterizations of oxygen photolysis and energy deposition rates due to solar energy absorption in the schumann-runge continuum. *Geophysical research letters*, 28(16):3163–3166.

Dickinson, R. E. (1984). Infrared radiative cooling in the mesosphere and lower thermosphere. *Journal of atmospheric and terrestrial physics*, 46(11):995–1008.

Dickinson, R. E., Ridley, E., and Roble, R. (1984). Thermospheric general circulation with coupled dynamics and composition. *Journal of the atmospheric sciences*, 41(2):205–219.

Dilecce, G. and De Benedictis, S. (1999). Experimental studies on elementary kinetics in n2-o2 pulsed discharges. *Plasma Sources Science and Technology*, 8(2):266.

Dodd, J., Singleton, S., Miller, S., Armstrong, P., and Blumberg, W. (1996). Vibrational relaxation of no (ν= 2, 3) by atomic oxygen. *Chemical Physics Letters*, 260(1-2):103–108.

Dodd, J. A., Lockwood, R. B., Hwang, E. S., Miller, S. M., and Lipson, S. J. (1999). Vibrational relaxation of no (υ= 1) by oxygen atoms. *The Journal of chemical physics*, 111(8):3498–3507.

Dotan, I., Hierl, P. M., Morris, R. A., and Viggiano, A. (1997). Rate constants for the reactions of n+ and n2+ with o2 as a function of temperature (300–1800 k). *International journal of mass spectrometry and ion processes*, 167:223–230.

Dotan, I. and Viggiano, A. (1999). Rate constants for the reaction of o+ with no as a function of temperature (300–1400 k). *The Journal of chemical physics*, 110(10):4730–4733.

Duff, J., Dothe, H., and Sharma, R. (2003). On the rate coefficient of the n (2d)+ o2 no+ o reaction in the terrestrial thermosphere. *Geophysical research letters*, 30(5).

Duff, J. W., Bien, F., and Paulsen, D. E. (1994). Classical dynamics of the n (4s)+ o2 (x^3 σg-) no (x^2ii)+ o (^{3}p) reaction. *Geophysical research letters*, 21(18):2043–2046.

Duff, J. W. and Sharma, R. D. (1997). Quasiclassical trajectory study of no vibrational relaxation by collisions with atomic oxygen. *Journal of the Chemical Society, Faraday Transactions*, 93(16):2645–2649.

Dungey, J. W. (1961). Interplanetary magnetic field and the auroral zones. *Physical Review Letters*, 6(2):47.

Fell, C., Steinfeld, J., and Miller, S. (1990). Quenching of n (2 d) by o (3 p). *The Journal of Chemical Physics*, 92(8):4768–4777.

Fennelly, J., Torr, D., Richards, P., and Torr, M. (1994). Simultaneous retrieval of the solar euv flux and neutral thermospheric o, o2, n2, and temperature from twilight airglow. *Journal of Geophysical Research: Space Physics*, 99(A4):6483–6490.

Fischer, H., Birk, M., Blom, C., Carli, B., Carlotti, M., Clarmann, T. v., Delbouille, L., Dudhia, A., Ehhalt, D., Endemann, M., et al. (2008). Mipas: an instrument for atmospheric and climate research. *Atmospheric Chemistry and Physics*, 8(8):2151–2188.

Foster, J. C., St-Maurice, J.-P., and Abreu, V. (1983). Joule heating at high latitudes. *Journal of Geophysical Research: Space Physics*, 88(A6):4885–4897.

Fox, J. L. and Sung, K. (2001). Solar activity variations of the venus thermosphere/ionosphere. *Journal of Geophysical Research: Space Physics*, 106(A10):21305–21335.

Funke, B. and López-Puertas, M. (2000). Nonlocal thermodynamic equilibrium vibrational, rotational, and spin state distribution of no (ν= 0, 1, 2) under quiescent atmospheric conditions. *Journal of Geophysical Research: Atmospheres*, 105(D4):4409–4426.

Gérard, J.-C., Bisikalo, D., Shematovich, V., and Duff, J. (1997). An updated model of the hot nitrogen atom kinetics and thermospheric nitric oxide. *Journal of Geophysical Research: Space Physics*, 102(A1):285–294.

Grossmann, K. and Vollmann, K. (1997). Thermal infrared measurements in the middle and upper atmosphere. *Advances in Space Research*, 19(4):631–638.

Hellberg, F., Rosén, S., Thomas, R., Neau, A., Larsson, M., Petrignani, A., and van der Zande, W. J. (2003). Dissociative recombination of no+: Dynamics of the x 1 σ+ and a 3 σ+ electronic states. *The Journal of chemical physics*, 118(14):6250–6259.

Herron, J. T. (1999). Evaluated chemical kinetics data for reactions of n (2 d), n (2 p), and n 2 (a 3 σ u+) in the gas phase. *Journal of Physical and Chemical Reference Data*, 28(5):1453–1483.

Hierl, P. M., Dotan, I., Seeley, J. V., Van Doren, J. M., Morris, R. A., and Viggiano, A. (1997). Rate constants for the reactions of o+ with n2 and o2 as a function of temperature (300–1800 k). *The Journal of chemical physics*, 106(9):3540–3544.

Hinteregger, H. E., Fukui, K., and Gilson, B. R. (1981). Observational, reference and model data on solar euv, from measurements on ae-e. *Geophysical Research Letters*, 8(11):1147–1150.

Hollas, J. M. (2004). *Modern spectroscopy*. John Wiley & Sons.

Hubert, B., Gérard, J.-C., Shematovich, V. I., and Bisikalo, D. V. (1996). High rotational excitation of no infrared thermospheric airglow: A signature of superthermal nitrogen atoms? *Geophysical research letters*, 23(17):2215–2218.

Hwang, E. S., Castle, K. J., and Dodd, J. A. (2003). Vibrational relaxation of no (v= 1) by oxygen atoms between 295 and 825 k. *Journal of Geophysical Research: Space Physics*, 108(A3).

Jacobson, M. Z. (2005). *Fundamentals of atmospheric modeling*. Cambridge university press.

Johnsen, R. and Biondi, M. A. (1980). Laboratory measurements of the o+ (^{2}d)+ n2 and o+ (^{2}d)+ o2 reaction rate coefficients and their ionospheric implications. *Geophysical Research Letters*, 7(5):401–403.

Kennealy, J., Del Greco, F., Caledonia, G., and Green, B. (1978). Nitric oxide chemiexcitation occurring in the reaction between metastable nitrogen atoms and oxygen molecules. *The Journal of Chemical Physics*, 69(4):1574–1584.

Knipp, D., Tobiska, W. K., and Emery, B. (2004). Direct and indirect thermospheric heating sources for solar cycles 21–23. *Solar Physics*, 224(1-2):495.

Kockarts, G. (1980). Nitric oxide cooling in the terrestrial thermosphere. *Geophysical Research Letters*, 7(2):137–140.

Kockarts, G. and Peetermans, W. (1970). Atomic oxygen infrared emission in the earth's upper atmosphere. *Planetary and Space Science*, 18(2):271–285.

Lee, L. C., Slanger, T., Black, G., and Sharpless, R. (1977). Quantum yields for the production of o (1 d) from photodissociation of o2 at 1160–1770 å. *The Journal of Chemical Physics*, 67(12):5602–5606.

Lei, J., Thayer, J. P., Lu, G., Burns, A. G., Wang, W., Sutton, E. K., and Emery, B. A. (2011). Rapid recovery of thermosphere density during the october 2003 geomagnetic storms. *Journal of Geophysical Research: Space Physics*, 116(A3).

Li, X., Huang, Y.-L., Flesch, G., and Ng, C. (1997). A state-selected study of the ion–molecule reactions o+(4 s, 2 d, 2 p)+ n 2. *The Journal of chemical physics*, 106(4):1373–1381.

Link, R. and Swaminathan, P. (1992). N (2d)+ o2: A source of thermospheric 6300 å emission? *Planetary and space science*, 40(5):699–705.

Logan, J. A., Prather, M., Wofsy, S., and McElroy, M. (1978). Atmospheric chemistry: Response to human influence. *Philosophical Transactions of the Royal Society of London A: Mathematical, Physical and Engineering Sciences*, 290(1367):187–234.

Lu, G., Hagan, M., Häusler, K., Doornbos, E., Bruinsma, S., Anderson, B., and Korth, H. (2014). Global ionospheric and thermospheric response to the 5 april 2010 geomagnetic storm: An integrated data-model investigation. *Journal of Geophysical Research: Space Physics*, 119(12).

Lu, G., Mlynczak, M., Hunt, L., Woods, T., and Roble, R. (2010). On the relationship of joule heating and nitric oxide radiative cooling in the thermosphere. *Journal of Geophysical Research: Space Physics*, 115(A5).

Midey, A. J., Miller, T. M., and Viggiano, A. (2004). Reactions of n+, n 2+, and n 3+ with no from 300 to 1400 k. *The Journal of chemical physics*, 121(14):6822–6829.

Midey, A. J. and Viggiano, A. (1999). Rate constants for the reaction of o 2+ with no from 300 to 1400 k. *The Journal of chemical physics*, 110(22):10746–10748.

Midey, A. J., Viggiano, A., Zhang, P., Irle, S., and Morokuma, K. (2006). A study of the reaction of n+ with o2: Experimental quantification of no+ (a 3+) production (298- 500 k) and computational study of the overall reaction pathways. *The Journal of Physical Chemistry A*, 110(9):3080–3086.

Miller, S. M. and Hunter, M. (2004). O (1d) branching fraction from the reaction n (2d)+ o2 no (2π, v, j)+ o (3p, 1 d). *The Journal of Physical Chemistry A*, 108(26):5588–5599.

Minschwaner, K. and Siskind, D. (1993). A new calculation of nitric oxide photolysis in the stratosphere, mesosphere, and lower thermosphere. *Journal of Geophysical Research: Atmospheres*, 98(D11):20401–20412.

Miquel, I., Hernando, J., Sayós, R., and González, M. (2003). Influence of collision energy on the n (2 d)+ o 2 o (3 p)+ no reaction dynamics: A quasiclassical trajectory study involving four potential energy surfaces. *The Journal of chemical physics*, 119(19):10040–10047.

Mlynczak, M., Martin-Torres, F. J., Russell, J., Beaumont, K., Jacobson, S., Kozyra, J., Lopez-Puertas, M., Funke, B., Mertens, C., Gordley, L., et al. (2003). The natural thermostat of nitric oxide emission at 5.3 μm in the thermosphere observed during the solar storms of april 2002. *Geophysical research letters*, 30(21).

Murphy, R., Lee, E., and Hart, A. (1975). Quenching of vibrationally excited nitric oxide by molecular oxygen and nitrogen. *The Journal of Chemical Physics*, 63(7):2919–2925.

Nicolet, M. (1955). The aeronomic problem of nitrogen oxides. *Journal of Atmospheric and Terrestrial Physics*, 7:152–169.

Nicolet, M. and Aikin, A. (1960). The formation of the d region of the ionosphere. *Journal of Geophysical Research*, 65(5):1469–1483.

Offermann, D. and Grossmann, K. (1978). Spectrometric measurement of atomic oxygen 63μm emission in the thermosphere. *Geophysical Research Letters*, 5(5):387–390.

Peterson, J., Le Padellec, A., Danared, H., Dunn, G., Larsson, M., Larson, A., Peverall, R., Strömholm, C., Rosén, S., Af Ugglas, M., et al. (1998). Dissociative recombination and excitation of n 2+: Cross sections and product branching ratios. *The Journal of chemical physics*, 108(5):1978–1988.

Picone, J., Hedin, A., Drob, D. P., and Aikin, A. (2002). Nrlmsise-00 empirical model of the atmosphere: Statistical comparisons and scientific issues. *Journal of Geophysical Research: Space Physics*, 107(A12).

Qian, L., Burns, A. G., Emery, B. A., Foster, B., Lu, G., Maute, A., Richmond, A. D., Roble, R. G., Solomon, S. C., and Wang, W. (2014). The ncar tie-gcm: A community model of the coupled thermosphere/ionosphere system. *Modeling the Ionosphere-Thermosphere System*, 201:73–83.

Qian, L., Roble, R. G., Solomon, S. C., and Kane, T. J. (2006). Calculated and observed climate change in the thermosphere, and a prediction for solar cycle 24. *Geophysical research letters*, 33(23).

Qian, L., Solomon, S. C., and Kane, T. J. (2009). Seasonal variation of thermospheric density and composition. *Journal of Geophysical Research: Space Physics*, 114(A1).

Rawlins, W., Fraser, M., and Miller, S. (1989). Rovibrational excitation of nitric oxide in the reaction of oxygen with metastable atomic nitrogen. *The Journal of Physical Chemistry*, 93(3):1097–1107.

Rawlins, W., Fraser, M., Miller, S., and Blumberg, W. (1992). Branching ratios for infrared vibrational emission from no (x 2π, v= 2–13). *The Journal of chemical physics*, 96(10):7555–7563.

Rawlins, W., Person, J., Fraser, M., Miller, S., and Blumberg, W. (1998). The dipole moment and infrared transition strengths of nitric oxide. *The Journal of chemical physics*, 109(9):3409–3417.

Rees, M. H. and Roble, R. G. (1975). Observations and theory of the formation of stable auroral red arcs. *Reviews of Geophysics*, 13(1):201–242.

Richards, P. (1986). Thermal electron quenching of n (2d): Consequences for the ionospheric photoelectron flux and the thermal electron temperature. *Planetary and space science*, 34(8):689–694.

Richards, P., Fennelly, J., and Torr, D. (1994). Euvac: A solar euv flux model for aeronomic calculations. *Journal of Geophysical Research: Space Physics*, 99(A5):8981–8992.

Richards, P. and Torr, D. (1983). A simple theoretical model for calculating and parameterizing the ionospheric photoelectron flux. *Journal of Geophysical Research: Space Physics*, 88(A3):2155–2162.

Richards, P. and Voglozin, D. (2011). Reexamination of ionospheric photochemistry. *Journal of Geophysical Research: Space Physics*, 116(A8).

Richmond, A., Ridley, E., and Roble, R. (1992). A thermosphere/ionosphere general circulation model with coupled electrodynamics. *Geophysical Research Letters*, 19(6):601–604.

Ridley, A., Deng, Y., and Toth, G. (2006). The global ionosphere–thermosphere model. *Journal of Atmospheric and Solar-Terrestrial Physics*, 68(8):839–864.

Roble, R., Ridley, E., and Dickinson, R. (1987). On the global mean structure of the thermosphere. *Journal of Geophysical Research: Space Physics*, 92(A8):8745–8758.

Roble, R. G. (1995). Energetics of the mesosphere and thermosphere. *The upper mesosphere and lower thermosphere: a review of experiment and theory*, pages 1–21.

Russell, J. M., Mlynczak, M. G., Gordley, L. L., Tansock, J. J., and Esplin, R. W. (1999). Overview of the saber experiment and preliminary calibration results. In *Optical Spectroscopic Techniques and Instrumentation for Atmospheric and Space Research III*, volume 3756, pages 277–289. International Society for Optics and Photonics.

Sander, S., Golden, D., Kurylo, M., Moortgat, G., Wine, P., Ravishankara, A., Kolb, C., Molina, M., Finlayson-Pitts, B., Huie, R., et al. (2006). Chemical kinetics and photochemical data for use in atmospheric studies evaluation number 15. Technical report, Pasadena, CA: Jet Propulsion Laboratory, National Aeronautics and Space Administration, 2006.

Schunk, R. and Nagy, A. (2009). *Ionospheres: physics, plasma physics, and chemistry*. Cambridge university press.

Scott, G. B., Fairley, D. A., Freeman, C. G., McEwan, M. J., and Anicich, V. G. (1998). Gas-phase reactions of some positive ions with atomic and molecular nitrogen. *The Journal of chemical physics*, 109(20):9010–9014.

Scott, G. B., Fairley, D. A., Milligan, D. B., Freeman, C. G., and McEwan, M. J. (1999). Gas phase reactions of some positive ions with atomic and molecular oxygen and nitric oxide at 300 k. *The Journal of Physical Chemistry A*, 103(37):7470–7473.

Sharma, R., Dothe, H., and Duff, J. (1998). Model of the 5.3 μm radiance from no during the sunlit terrestrial thermosphere. *Journal of Geophysical Research: Space Physics*, 103(A7):14753–14768.

Sharma, R., Wheeler, N., Wise, J., Dothe, H., and Duff, J. (2000). Global variation in the 2.7 μm no overtone limb-emission from the lower thermosphere. *Geophysical research letters*, 27(3):349–352.

Sharma, R., Zygelman, B., Von Esse, F., and Dalgarno, A. (1994). On the relationship between the population of the fine structure levels of the ground electronic state of atomic oxygen and the translational temperature. *Geophysical research letters*, 21(16):1731–1734.

Sharma, R. D. and Roble, R. G. (2001). Impact of the new rate coefficients for the o atom vibrational deactivation and photodissociation of no on the temperature and density structure of the terrestrial atmosphere. *Journal of Geophysical Research: Space Physics*, 106(A10):21343–21350.

Sheehan, C. H. and St-Maurice, J.-P. (2004). Dissociative recombination of n2+, o2+, and no+: Rate coefficients for ground state and vibrationally excited ions. *Journal of Geophysical Research: Space Physics*, 109(A3).

Sheng, C., Lu, G., Solomon, S. C., Wang, W., Doornbos, E., Hunt, L. A., and Mlynczak, M. G. (2017). Thermospheric recovery during the 5 april 2010 geomagnetic storm. *Journal of Geophysical Research: Space Physics*, 122(4):4588–4599.

Shved, G. M., Khvorostovskaya, L. E., Potekhin, I. Y., Ogibalov, V. P., and Uzyukova, T. V. (2003). Measurement of rate constant for quenching co2 (01 0) by atomic oxygen at low temperatures: reassessment of the population of co2 (01 0) and the co2 15-μm emission cooling in the lower thermosphere. In *Proc. of SPIE Vol*, volume 4882, page 107.

Smithtro, C. and Sojka, J. J. (2005). A new global average model of the coupled thermosphere and ionosphere. *Journal of Geophysical Research: Space Physics*, 110(A8).

Smithtro, C. and Solomon, S. (2008). An improved parameterization of thermal electron heating by photoelectrons, with application to an x17 flare. *Journal of Geophysical Research: Space Physics*, 113(A8).

Smithtro, C. G. (2004). Response of the ionosphere and thermosphere to extreme solar conditions. Technical report, UTAH STATE UNIV LOGAN.

Solomon, S. C. and Abreu, V. J. (1989). The 630 nm dayglow. *Journal of Geophysical Research: Space Physics*, 94(A6):6817–6824.

Solomon, S. C., Hays, P. B., and Abreu, V. J. (1988). The auroral 6300 å emission: Observations and modeling. *Journal of Geophysical Research: Space Physics*, 93(A9):9867–9882.

Solomon, S. C. and Qian, L. (2005). Solar extreme-ultraviolet irradiance for general circulation models. *Journal of Geophysical Research: Space Physics*, 110(A10).

Stephan, A., Meier, R., Dymond, K., Budzien, S., and McCoy, R. (2003). Quenching rate coefficients for o+ (2p) derived from middle ultraviolet airglow. *Journal of Geophysical Research: Space Physics*, 108(A1).

Stolarski, R. (1976). Energetics of the midlatitude thermosphere. *Journal of Atmospheric and Terrestrial Physics*, 38(8):863–868.

Strobel, D. F. (1978). Parameterization of the atmospheric heating rate from 15 to 120 km due to o2 and o3 absorption of solar radiation. *Journal of Geophysical Research: Oceans*, 83(C12):6225–6230.

Sultanov, R. A. and Balakrishnan, N. (2006). Quantum mechanical investigations of the n (s 4)+ o 2 (x σ g- 3) no (x π 2)+ o (p 3) reaction. *The Journal of chemical physics*, 124(12):124321.

Swaminathan, P., Strobel, D., Acton, L., and Paxton, L. (2001). Model update for mesospheric/thermospheric nitric oxide. *Physics and Chemistry of the Earth, Part C: Solar, Terrestrial & Planetary Science*, 26(7):533–537.

Swaminathan, P., Strobel, D., Kupperman, D., Kumar, C. K., Acton, L., DeMajistre, R., Yee, J.-H., Paxton, L., Anderson, D., Strickland, D., et al. (1998). Nitric oxide abundance in the mesosphere/lower thermosphere region: Roles of solar soft x rays, suprathermal

n (4 s) atoms, and vertical transport. *Journal of Geophysical Research: Space Physics*, 103(A6):11579–11594.

Swartz, W. E. and Nisbet, J. S. (1972). Revised calculations of f region ambient electron heating by photoelectrons. *Journal of Geophysical Research*, 77(31):6259–6261.

Venkataramani, K., Yonker, J. D., Bailey, S., et al. (2016). Contribution of chemical processes to infrared emissions from nitric oxide in the thermosphere. *Journal of Geophysical Research: Space Physics*, 121(3):2450–2461.

Watanabe, K. (1958). Ultraviolet absorption processes in the upper atmosphere. In *Advances in geophysics*, volume 5, pages 153–221. Elsevier.

Whitson, M., Darnton, L. A., and McNeal, R. J. (1976). Vibrational energy distribution in the no produced by the reaction of n (4s) with o2. *Chemical Physics Letters*, 41(3):552–556.

Winkler, I., Stachnik, R., Steinfeld, J., and Miller, S. (1986). Determination of no (v= 0–7) product distribution from the n (4 s)+ o2 reaction using two-photon ionization. *The Journal of chemical physics*, 85(2):890–899.

Wise, J., Smith, D., Wheeler, N., Ahmadjian, M., Nadile, R., and Sullivan, B. (2001). Overview and summary of results and significant findings from the cirris-1a experiment. *Journal of Spacecraft and Rockets*, 38(3):297–322.

Woods, T. N., Eparvier, F. G., Bailey, S. M., Chamberlin, P. C., Lean, J., Rottman, G. J., Solomon, S. C., Tobiska, W. K., and Woodraska, D. L. (2005). Solar euv experiment (see): Mission overview and first results. *Journal of Geophysical Research: Space Physics*, 110(A1).

Woods, T. N. and Rottman, G. J. (2002). Solar ultraviolet variability over time periods of aeronomic interest. *Atmospheres in the Solar System: Comparative Aeronomy*, pages 221–233.

Yonker, J. D. (2013). *Contribution of the first electronically excited state of molecular nitrogen to thermospheric nitric oxide*. PhD thesis, Virginia Polytechnic Institute and State University.

Zipf, E., Espy, P., and Boyle, C. (1980). The excitation and collisional deactivation of metastable n (^{2}p) atoms in auroras. *Journal of Geophysical Research: Space Physics*, 85(A2):687–694.